

2006

## Electromagnetic characterization of miniature antennas for portable devices

Diana P. Aristizabal  
*University of South Florida*

Follow this and additional works at: <https://digitalcommons.usf.edu/etd>



Part of the [American Studies Commons](#)

---

### Scholar Commons Citation

Aristizabal, Diana P., "Electromagnetic characterization of miniature antennas for portable devices" (2006). *USF Tampa Graduate Theses and Dissertations*.  
<https://digitalcommons.usf.edu/etd/2441>

This Thesis is brought to you for free and open access by the USF Graduate Theses and Dissertations at Digital Commons @ University of South Florida. It has been accepted for inclusion in USF Tampa Graduate Theses and Dissertations by an authorized administrator of Digital Commons @ University of South Florida. For more information, please contact [digitalcommons@usf.edu](mailto:digitalcommons@usf.edu).

Electromagnetic Characterization of Miniature Antennas for Portable Devices

by

Diana P. Aristizabal

A thesis submitted in partial fulfillment  
of the requirements for the degree of  
Master of Science in Electrical Engineering  
Department of Electrical Engineering  
College of Engineering  
University of South Florida

Major Professor: Thomas M. Weller, Ph.D.  
Kenneth A. Buckle, Ph.D.  
Arthur David Snider, Ph.D.

Date of Approval:  
October 30, 2006

Keywords: Self-Complementary, Archimedean, Equiangular, Balun, FSS, Helical

© Copyright 2006, Diana P. Aristizabal

## Dedication

To my beloved husband Fernando Aristizabal, my daughter Sofia Aristizabal, and my parents Alberto Mora Perez and Beatriz Castro de Mora.

## Acknowledgements

I would like to express my gratitude to Dr. Thomas M. Weller for his excellent support, guidance, and for granting me with the opportunity to work in such an interesting project. In addition, I want to recognize Xetron- Northrop Grumman for sponsoring my research.

Next, I want to thank my committee members Dr. Kenneth A. Buckle and Dr. Arthur David Snider for their excellent suggestions to improve my work. Also, I want to recognize Modelithics Inc. for providing me with the necessary parts for some of my measurement characterization projects, as well as for letting me use their facilities to make measurements.

Finally, I want to thank my colleagues in the Antennas and Propagation Lab (412) for their great support and friendship, especially, Bojana Zivanovic, Suzette Presas, Saravana P. Natarajan, Alberto Rodriguez, Sam Baylis, Sergio Melais, and Srinath Balachandran.

## Table of Contents

List of Tables	iii
List of Figures	iv
Abstract	x
Chapter 1 Introduction	1
1.1 Overview	1
1.2 Contributions	3
Chapter 2 Frequency Independent Antennas	4
2.1 Introduction	4
2.2 Equiangular Spiral Antenna	6
2.2.1 Background Theory	7
2.2.2 Design	9
2.3 Archimedean Spiral Antenna	10
2.3.1 Background Theory	11
2.3.2 Design	13
2.4 Electromagnetic Design and Simulations of Equiangular Spiral Antenna	14
2.4.1 S-parameter Simulations	17
2.4.2 Radiation Pattern Simulations	20
2.4.3 Antenna Parameters Simulations	25
2.5 Electromagnetic Design and Simulations of Archimedean Spiral Antenna	28
2.5.1 S-parameter Simulations	29
2.5.2 Radiation Pattern Simulations	32
2.5.3 Antenna Parameters Simulations	34
2.6 Summary and Conclusions	36
Chapter 3 Archimedean Spiral Antenna with a Narrow-Band Feed Network	38
3.1 Introduction	38
3.2 Archimedean Spiral Antenna Design	39
3.2.1 Electromagnetic Simulations of the Spiral Antenna on a Thinner Substrate	40
3.2.1.1 S-parameter Simulations	41
3.2.1.2 Radiation Pattern Simulations	43
3.2.1.3 Antenna Parameter Simulations	44

3.2.2 Electromagnetic Simulations of the Effect of Adding a Narrow-Band Feed Structure to the Spiral Antenna	46
3.2.2.1 S-parameters Simulations	49
3.2.2.2 Radiation Pattern Simulations	51
3.2.2.3 Antenna Parameters Simulations	53
3.2.3 Microwave Simulations of the Effect of Adding a Narrow-Band Feed Structure to the Spiral Antenna	55
3.3 Balun Design	60
3.3.1 Background Theory	61
3.3.2 Microwave Design and Simulations	62
3.3.2.1 Balanced Input to Unbalanced Output Transition Simulations	65
3.3.2.2 Impedance Transformation Simulations	67
3.3.3 Ground Effects Microwave and Electromagnetic Simulations	69
3.4 Fabrication	72
3.5 Measurements	73
3.5.1 S-parameters Measurements	74
3.5.2 Radiation Pattern Measurements	75
3.5.3 Balun Measurements	78
3.6 RF Coaxial Connector Electromagnetic Simulations	79
3.7 Summary and Conclusions	81
 Chapter 4 Frequency Selective Surfaces	 83
4.1 Introduction	83
4.2 Theory of Operation	84
4.3 Summary and Conclusions	88
 Chapter 5 Miniature Coil Antennas	 89
5.1 Introduction	89
5.2 Background Theory	89
5.3 Measurement Characterization	92
5.3.1 S-parameter Measurements	95
5.3.2 Efficiency Measurements	96
5.4 Summary and Conclusions	104
 Chapter 6 Conclusions and Recommendations	 105
6.1 Conclusions	105
6.2 Recommendations for Future Work	107
 References	 109

## List of Tables

Table 2.1	Radius Equations Calculations for the Two-Arm Equiangular Spiral Antenna	10
Table 2.2	Calculated Design Parameters for the Archimedean Spiral Antenna	14
Table 2.3	Radius Equations Calculations for the Two-Arm Archimedean Spiral	14
Table 5.1	Calculation of Inductor Parameters	94
Table 5.2	Calculation of Wire Length for Optimal Radiation Performance	95

## List of Figures

Figure 2.1	Antenna Defined as a Transition Region Between a Wave Guided by a Transmission Line and a Free-Space Wave	5
Figure 2.2	Equiangular Spiral Curve	7
Figure 2.3	Frequency-Independent Planar Self-Complementary Equiangular Spiral Antenna	9
Figure 2.4	Frequency-Independent Planar Self-Complementary Archimedean Spiral Antenna	13
Figure 2.5	Radiation Boundary Assignment for the Equiangular Spiral Antenna	16
Figure 2.6	Lumped Port Assignment for the Equiangular Spiral Antenna	16
Figure 2.7	S-parameter Simulations for the Equiangular Spiral Antenna	18
Figure 2.8	Input Impedance Simulations for the Equiangular Spiral Antenna	19
Figure 2.9	Simulated VSWR for the Equiangular Spiral Antenna	20
Figure 2.10	Coordinate System for Antenna Analysis	21
Figure 2.11	Simulated Radiation Pattern Versus Theta at 2.4GHz for the Equiangular Spiral Antenna	24
Figure 2.12	Side, Front, and Top Views of Simulated Radiation Pattern in 3D at 2.4GHz for the Equiangular Spiral Antenna Backed by a $\lambda/4$ Thick Substrate	25
Figure 2.13	Side, Front, and Top Views of Simulated Radiation Pattern in 3D at 2.4GHz for the Equiangular Spiral Antenna Backed by a $\lambda/4$ Thick Substrate and a Ground Plane	25
Figure 2.14	Simulated Total Gain (dB) Versus Frequency for the Equiangular Spiral Antenna	28

Figure 2.15	Simulated Axial Ratio (dB) Versus Frequency for the Equiangular Spiral Antenna	28
Figure 2.16	Radiation Boundary Assignment for the Archimedean Spiral Antenna	29
Figure 2.17	Lumped Port Assignment for the Archimedean Spiral Antenna	29
Figure 2.18	S-parameter Simulations for the Archimedean Spiral Antenna with and without a Ground Plane	30
Figure 2.19	Input Impedance Simulations for the Archimedean Spiral Antenna with and without a Ground Plane	31
Figure 2.20	Simulated VSWR for the Archimedean Spiral Antenna with and without a Ground Plane	31
Figure 2.21	Simulated Radiation Pattern Versus Theta at 2.4GHz for the Archimedean Spiral Antenna with and without a Ground Plane	33
Figure 2.22	Side, Front, and Top Views of Simulated Radiation Pattern in 3D at 2.4GHz for the Archimedean Spiral Antenna Backed by a $\lambda/4$ Thick Substrate	33
Figure 2.23	Side, Front, and Top Views of Simulated Radiation Pattern in 3D at 2.4GHz for the Archimedean Spiral Antenna Backed by a $\lambda/4$ Thick Substrate and a Ground Plane	34
Figure 2.24	Simulated Total Gain (dB) Versus Frequency for the Archimedean Spiral Antenna with and without a Ground Plane	35
Figure 2.25	Simulated Axial Ratio (dB) Versus Frequency for the Archimedean Spiral Antenna with and without a Ground Plane	36
Figure 3.1	Spiral Antenna Integrated with a Narrow-band Feed Network	39
Figure 3.2	Radiation Boundary Assignment for the Archimedean Spiral Antenna on a 31-mil Thick Substrate	41
Figure 3.3	S-parameter Simulations for the Archimedean Spiral Antenna	42
Figure 3.4	Input Impedance Simulations for the Archimedean Spiral Antenna	42
Figure 3.5	Simulated VSWR for the Archimedean Spiral Antenna	43

Figure 3.6	Simulated Radiation Pattern Versus Theta at 2.4GHz for the Archimedean Spiral Antenna	44
Figure 3.7	Side, Front, and Top Views of Simulated Radiation Pattern in 3D at 2.4GHz for the Archimedean Spiral Antenna Backed by a 31-mil Thick Substrate	44
Figure 3.8	Simulated Total Gain (dB) Versus Frequency for the Archimedean Spiral Antenna	45
Figure 3.9	Simulated Axial Ratio (dB) Versus Frequency for the Archimedean Spiral Antenna	46
Figure 3.10	Wave Port Assignment at the Bottom of the 31-mil Thick Substrate for the Archimedean Spiral Antenna with Feeding Wires	47
Figure 3.11	Wave Port Assignment to One Side of the 31-mil Thick Substrate for the Archimedean Spiral Antenna with Feeding Twin-Strip Lines	47
Figure 3.12	Radiation Boundary Assignment for the Archimedean Spiral Antenna with Feeding Wires and a 31-mil Thick Substrate	49
Figure 3.13	Radiation Boundary Assignment for the Archimedean Spiral Antenna with Feeding Twin-Strip Lines and a 31-mil Thick Substrate	49
Figure 3.14	S-parameter Simulations for the Archimedean Spiral Antenna Backed by a 31-mil Thick Substrate	50
Figure 3.15	Input Impedance Simulations for the Archimedean Spiral Antenna Backed by a 31-mil Thick Substrate	51
Figure 3.16	Simulated Radiation Pattern Versus Theta at 2.4GHz for the Archimedean Spiral Antenna Backed by a 31-mil Thick Substrate	52
Figure 3.17	Side, Front, and Top Views of Simulated Radiation Pattern in 3D at 2.4GHz for the Archimedean Spiral Antenna Backed by a 31-mil Thick Substrate and Simulated with Feeding wires	52
Figure 3.18	Side, Front, and Top Views of Simulated Radiation Pattern in 3D at 2.4GHz for the Archimedean Spiral Antenna Backed by a 31-mil Thick Substrate and Simulated with Feeding Twin-Strip Lines	53

Figure 3.19	Simulated Total Gain (dB) Versus Frequency for the Archimedean Spiral Antenna Backed by a 31-mil Thick Substrate	54
Figure 3.20	Simulated Axial Ratio (dB) Versus Frequency for the Archimedean Spiral Antenna Backed by a 31-mil Thick Substrate	55
Figure 3.21	ADS Approximation of the Spiral Antenna Response when Simulated with Feeding Wires	56
Figure 3.22	S-parameters Simulations of Spiral Antenna Feeding Wires	58
Figure 3.23	ADS Approximation of the Spiral Antenna Response when Simulated with Twin-Strip Lines	59
Figure 3.24	S-parameters Simulations of Spiral Antenna Feeding Twin-Strip Lines	60
Figure 3.25	Integration of Spiral Antenna and Narrow-band Feed Network	60
Figure 3.26	Balanced and Unbalanced Modes on a Three-Wire Transmission Line	62
Figure 3.27	Input Impedance of the Spiral Antenna with Feeding Twin-Strip Lines	63
Figure 3.28	Matching Network Topology Needed to Match the Antenna Input Impedance to 200 Ohms	64
Figure 3.29	Ideal Lumped Element Matching Network Solution	64
Figure 3.30	Ideal Versus Modelithics Johanson Models Matching Network Solution	65
Figure 3.31	Ideal Versus Modelithics Johanson Models Matching Networks	65
Figure 3.32	Balun Design	66
Figure 3.33	Balun Design Optimization in ADS to Connect a Balanced Input to an Unbalanced Output	67
Figure 3.34	S12 (phase) of Balun Design	67
Figure 3.35	Impedance Transformation Design in ADS	68
Figure 3.36	Balun Input Impedance	69

Figure 3.37	Ground Effects Microwave and Electromagnetic Simulations of the Balun Design	70
Figure 3.38	Babinet's Principle Approximation Between the Twin-Strip Line and CPW Structures	71
Figure 3.39	S-parameter Simulations for the Back-to-Back Balun Design	72
Figure 3.40	Fabricated Self-Complementary Archimedean Spiral Antenna with a Narrow-band Feed Network	73
Figure 3.41	Fabricated Back-to-Back Balun Design	73
Figure 3.42	Comparison Between Simulated and Measured S-parameters of Archimedean Spiral Antenna	74
Figure 3.43	E-Plane Radiation Pattern Measurements of Fabricated Spiral Antenna	77
Figure 3.44	H-Plane Radiation Pattern Measurements of Fabricated Spiral Antenna	78
Figure 3.45	Measured S-parameters of Fabricated Back-to-Back Balun Design	79
Figure 3.46	Back-to-Back Connector Design	81
Figure 3.47	S-parameter Simulations of Back-to-Back Connector Design	81
Figure 4.1	Basic Frequency Selective Surfaces	85
Figure 4.2	Cross Section and Top View of a High-Impedance Surface	86
Figure 4.3	Three-Layer High-Impedance Surface	87
Figure 5.1	Typical Geometry for a Helix	90
Figure 5.2	Six 1-Port Bonding Configurations Used to Characterize Surface Mount Chip Inductors as Miniature Antennas	92
Figure 5.3	Surface Mount Chip Inductor	93
Figure 5.4	S-parameters of 270 nH 0603 Coil Inductor Bonded in a 1-Port Configuration Radiating into Free Space	96
Figure 5.5	Efficiency Measurements	98

Figure 5.6	S-parameters of 270 nH 0603 Coil Inductor Bonded in a 1-Port Configuration Radiating Inside the Wheeler Cap	99
Figure 5.7	Radiation Efficiency of 270 nH 0603 Coil Inductor Bonded in a 1-Port Configuration	100
Figure 5.8	Input Impedance of 270 nH 0603 Coil Inductor Bonded in a 1-Port Configuration Radiating in Free Space	103

# Electromagnetic Characterization of Miniature Antennas for Portable Devices

Diana P. Aristizabal

## ABSTRACT

Advances in technology have placed a great emphasis on the design of broadband antennas as well as antenna miniaturization to cope with the demands of making electronic and handheld communication devices smaller and more efficient. In this thesis, the design and fabrication of a frequency independent antenna and a narrow-band planar microstrip Balun are presented. An analysis of frequency selective surfaces is also introduced in order to demonstrate their capability to miniaturize antenna thickness. Lastly, s-parameters measurements and efficiency characterization are performed to determine the radiation properties of surface mount chip inductors in order to determine the feasibility of using them as electrically small antennas.

Two types of frequency independent antennas are considered due to their planar geometries, the Equiangular and Archimedean spiral antennas. Frequency independent antennas are radiating devices that have frequency independent impedance and pattern properties because their shape is specified only in terms of angles.

The Balun is designed to meet the need of a feeding element for the Archimedean spiral antenna. A Balun is a three port device that connects an unbalanced transmission line such as a coaxial line to a balanced feed line such as the one required by two-arm spiral antennas. The Balun discussed in this work is designed to operate at 2.4 GHz with

a 200 MHz bandwidth and to transform the antenna input impedance to a 50-ohm reference impedance. The main characteristics from this device that distinguish it from commercially available structures are its low cost, planarity, and compact footprint. The balancing capability of this Balun is shown by the close agreement between the measured and simulated results.

Antennas can be potentially miniaturized in the z-direction by replacing the PEC ground plane separated from the antenna by a  $\lambda/4$  thick substrate with a frequency selective surface (FSS) structure that allows the ground plane conductor to be in close proximity to the antenna without affecting its radiation performance. The FSS layer operating at 2.4 GHz presented in this thesis is static (not tuned) and thus the overall bandwidth reduces approximately to the bandwidth obtained with the narrow-band Balun.

## Chapter 1

### Introduction

#### 1.1 Overview

Advances in technology have led to the design of antennas capable of transmitting and/or receiving radio frequency signals at a wide frequency band, which would simplify the complexity in a wireless network design by reducing the amount of antennas necessary to cover a wide frequency range of operation. Two types of inherently broadband antennas were considered in this research work due to their planar geometries, the Equiangular and Archimedean spiral antennas. These two types of antennas were designed as two-arm spirals. They were fed using a feed network that connects the antenna balanced input to an unbalanced feed line. Electromagnetic analysis of each of these antennas is presented in chapter 2 in order to establish the best working design at the frequency range of interest from 2 to 6 GHz.

The optimum frequency independent antenna design as far as its fine quality radiation characteristics was constructed and integrated with a narrow-band feed network. Throughout chapter 3, electromagnetic and circuit level simulations were performed to investigate the effect on the antenna radiation performance when decreasing the substrate thickness from  $\lambda/4$  (calculated at 2.4 GHz) to 31 mils. In order to feed the two-arm spiral antenna with a narrow-band feed network, it was necessary to access the antenna feed point with vias that go to the end of the substrate and twin-strip lines to connect the

balanced antenna input to the feed network. With the aim of electromagnetic simulations, the antenna performance was analyzed all the way to the point where it is connected to the balanced feed network.

The designed narrow-band feed network consists of a Balun, which properly connects a balanced transmission line to an unbalanced transmission line. The unbalanced transmission line connects the antenna balanced feed line to an RF coaxial connector. Furthermore, the balun was measured with the antenna at the input of the connector as well as separate from the antenna in a back-to-back configuration. The RF coaxial connector was also simulated in HFSS in a two-port back-to-back configuration so as to investigate the performance of the transition from the unbalanced line to the input of the connector.

In chapter 4, the background theory of operation for frequency selective surfaces is analyzed. A frequency selective surface (FSS) is a metal surface coated with resonant structures that do not support surface waves within a frequency band. They can serve as substrates for antennas allowing them to lie directly adjacent to the ground plane surface without being shorted out. A low-frequency structure operating at 2.4GHz is evaluated that could potentially miniaturize the spiral antenna designed in chapter 2 in the z-direction.

Advances in technology have placed a great emphasis not only on broadband antennas to cover an entire design application range but also on antenna miniaturization to cope with the demands of making electronic devices smaller. In chapter 5, the fundamental limits of electrically small antennas are studied as far as how small an antenna can be at a particular wavelength and still behave as an efficient radiating device.

In addition, research and measurement characterization were oriented to investigate the feasibility of using chip inductors mounted in a 1-port configuration as electrically and physically small helical antennas operating at the frequency range of 1 to 3 GHz. The research focuses on reflection coefficient and radiation efficiency measurements in order to characterize their performance as electrically small antennas.

## 1.2 Contributions

The design of two self-complementary frequency independent spiral antennas and a planar narrow-band Balun has been presented. The electromagnetic simulations and measurement characterization of these antennas and feed network have provided an understanding of their capabilities and limitations. The main contributions from this work are the introduction of inherently broadband antennas achieving optimum operation, the design of a planar narrow-band Balun transformer operating as an efficient antenna feed network, the characterization of coil inductors as practical miniature antennas, and the study of FSS structures as potential ground planes structures allowing antenna miniaturization.

## Chapter 2

### Frequency Independent Antennas

#### 2.1 Introduction

An antenna is the structure associated with the transition region between a guided wave present in a waveguide, microstrip or transmission line and a free-space radiating wave. Thus, an antenna represents an interface where the conversion of electrons on conductors to photons in space takes place. Figure 2.1 illustrates this transition between a guided wave and a free space wave. It is desirable that this transmission of energy occurs with maximum efficiency. Once the transmission line separation approaches a wavelength or more, the guided wave or plane wave traveling along the transmission line in one dimension tends to be radiated so that the opened-out line acts like an antenna, which launches a free space wave or spherically expanding wave as illustrated on figure 2.1. The currents on the transmission line flow out on the transmission line and end there, but the fields associated with them continue [1].

The demands for numerous applications of electromagnetics due to the advances in technology have led to the design of broadband antennas. In 1954, Victor H. Rumsey introduced a class of structures and suggested that their pattern and impedance properties should be independent of frequency [2]. Rumsey's principle states that the impedance and pattern properties of an antenna are frequency independent if the antenna shape is specified only in terms of angles [1]. Therefore, frequency independent antennas

correspond to a type of structures that can be their own continuously scaled models since any characteristic length is replaced by specified angles.

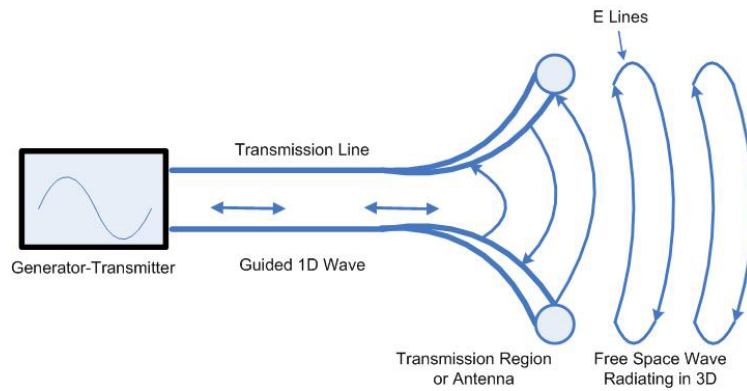


Figure 2.1 Antenna Defined as a Transition Region Between a Wave Guided by a Transmission Line and a Free-Space Wave [1]

A successful frequency independent antenna must radiate most of the power in a finite active region so that it can be truncated with little effects on the pattern. Therefore, the currents must decay after the radiating active region. The finite active region is identified by truncation constants used to size the design. It must also be a transmission-line structure to carry power to the lower frequency end when fed from the high frequency end. Furthermore, a true frequency independent antenna has a constant beam width over the designed frequency band of operation if the active region dimensions scale with wavelength [3].

Two types of frequency independent antennas were considered due to their planar geometries, the self-complementary planar Equiangular and Archimedean spiral antennas. A spiral antenna is a bidirectional radiating device, which consists of a thin metal foil spiral pattern etched on a substrate, usually fed from the center, and located over a backing cavity to either properly reflect or absorb the energy [3]. These two types

of antennas were designed as two-arm spirals since they can be fed using a fairly simple feed network that connects the antenna balanced input to an unbalanced feed line.

Both the Equiangular and Archimedean spiral antennas share a particular feature of frequency independent antennas called the self-complementary structure. The complementary structure of a metal antenna with input impedance  $Z_{\text{metal}}$  is an antenna with input impedance  $Z_{\text{air}}$  that can be formed with air replacing the metal and metal replacing the air of the original metal antenna. Therefore, complementary antennas are similar to a positive and negative in photography. [4]. Then, it can be shown from Babinet's principle that the impedances of complementary antennas are related by equation 2.1, where  $\eta$  is the impedance of free space equal to 377 ohms.

$$Z_{\text{air}} \cdot Z_{\text{metal}} = \frac{\eta^2}{4} \quad (2.1)$$

If an antenna and its complement are actually the same, they are called self-complementary and are defined by equation 2.2 [4].

$$Z_{\text{air}} = Z_{\text{metal}} = \frac{\eta}{2} = 188.5 \text{ohms} \quad (2.2)$$

Throughout this chapter, electromagnetic analysis of each of these antennas is presented in order to establish the best working design at the frequency range of interest. Subsequently, the best antenna design is fabricated and tested with a narrow-band feed network. This procedure is presented in Chapter 3.

## 2.2 Equiangular Spiral Antenna

The self-complementary planar equiangular spiral antenna is considered a frequency independent antenna because it satisfies the requirement that its geometry is entirely defined by angles. Additionally, this type of antenna obeys the truncation

requirement that the currents decay after the radiating active region so that the structure can be stopped without adversely affecting the antenna properties [3].

### 2.2.1 Background Theory

An equiangular spiral antenna can be defined by the spiral curve given by equation 2.3 and also shown in figure 2.2 [1], where  $r$  is the radial distance to a point  $P$  on the spiral,  $\theta$  is the angle sweep with respect to the  $x$  axis, and  $a$  is the spiral constant or flare rate which determines the tightness of the spiral winding [2]. The spiral curve on figure 2.2 is right-handed due to the positive value of the constant  $a$ . Likewise, left-handed spiral curves can be obtained using negative values of  $a$ .

$$r_1 = a^\theta \tag{2.3}$$

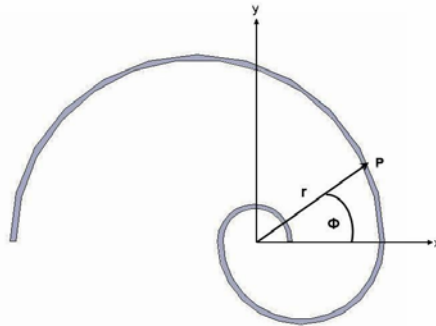


Figure 2.2 Equiangular Spiral Curve

Rotating the spiral curve  $r_1$  (equation 2.3) by a  $\delta$  angle generates the spiral curve  $r_2$  (equation 2.4). Similarly, shifting the angle  $\theta$  of equations 2.3 and 2.4 by 180 degrees ( $\pi$ ) creates the spiral curves  $r_3$  and  $r_4$  (equations 2.5 and 2.6 respectively).

$$r_2 = a^{(\theta-\delta)} \tag{2.4}$$

$$r_3 = a^{(\theta-\pi)} \tag{2.5}$$

$$r_4 = a^{(\theta - \pi - \delta)} \quad (2.6)$$

By metalizing the areas between spiral curves  $r_1$  and  $r_2$  (equations 2.3 and 2.4 respectively) and between spiral curves  $r_3$  and  $r_4$  (equations 2.5 and 2.6 respectively), with the other areas open, a two-arm equiangular spiral antenna is created as shown on figure 2.3. The arrows indicate the direction of the outgoing waves traveling along the conductors resulting in right-circularly polarized (RCP) radiation outward from the page and left-circularly polarized radiation into the page [1].

The  $\delta$  rotation angle can be defined by equation 2.7, where the gap/arm ratio is equal to 1 for a self-complementary structure and  $N$  is the number of spiral turns [3]. Spirals with one half to three turns have been found experimentally to be relatively insensitive to the parameters “a” and  $\delta$  [4]. Another way of describing the spiral curves is through the expansion factor (EF), which is defined by equation 2.8 as the ratio of radius increase in one turn.

$$\delta = \frac{2 \cdot \pi}{N \cdot \left(1 + \frac{\text{gap}}{\text{arm}}\right)} \quad (2.7)$$

$$\text{EF} = a^{2 \cdot \pi} \quad (2.8)$$

The high-frequency limit of operation is determined by the spacing “d” of the input terminal [1]. The upper cutoff is limited to frequencies for which the spacing “d” of the input terminal cease to look like a point [5]. In the same way, the low-frequency limit of operation is determined by the overall diameter “D” [1], which denotes the point of truncation where the total arm length is comparable to the wavelength and where the

current becomes negligible [5]. Thus, for all frequencies above the lowest frequency of operation, the pattern and impedance characteristics are frequency independent [5].

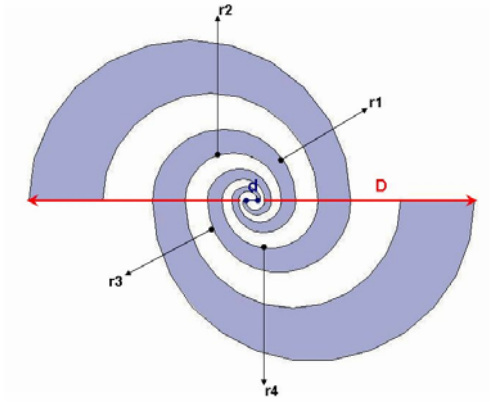


Figure 2.3 Frequency-Independent Planar Self-Complementary Equiangular Spiral Antenna

### 2.2.2 Design

The frequency range of interest is from 2 to 6 GHz. The equiangular spiral was designed as a two-arm spiral with the number of turns  $N$  equal to 2. By setting the maximum radius of the spiral “ $R$ ” equal to  $\lambda_L/4$  (where  $\lambda_L$  is the wavelength at the lower band edge frequency) and the minimum radius of the spiral “ $r$ ” to  $\lambda_U/4$  (where  $\lambda_U$  is the wavelength at the upper frequency band edge), the antenna bandwidth is 3 to 1. This is the bandwidth we are looking for even though this type of antenna could provide much larger bandwidths. The flare rate “ $a$ ” can be found from the maximum radius “ $R$ ” as shown by equation 2.9, where  $4\pi$  is the  $\theta$  angle for two spiral turns, “ $c$ ” equals  $3 \times 10^8$  m/s,  $f_L$  equals 2 GHz, and  $e_{\text{reff}}$  is the effective dielectric constant of the dielectric material backing up the antenna. We chose the Rogers 5880 RT Duroid substrate with  $e_r$  equal to 2.2 for all calculations and simulations. The effective dielectric constant of this Rogers material is approximately equal to 1.6<sup>1</sup>. By solving equation 2.9, we obtain a flare rate

<sup>1</sup> The effective dielectric constant was approximated by the following formula  $e_{\text{reff}} = (e_r + 1)/2$

“a” equal to 1.31. The expansion factor equals to 5.46, and a typical value for the expansion factor is 4. From equation 2.7, we find the  $\delta$  rotation angle to be equal to  $\pi/2$  for a two-turn self-complementary structure consisting of two arms.

$$R = a^{4 \cdot \pi} = \frac{\lambda_L}{4} = \frac{c}{4 \cdot f_L \cdot \sqrt{\epsilon_{\text{reff}}}} \quad (2.9)$$

Table 2.1 shows the calculated radius equations for the two-arm spiral antenna, where r1 through r4 corresponds to equations 2.3 to 2.6 respectively. Units are specified in mm. The physical dimensions of the equiangular spiral antenna are 50.5mm x 33.7mm.

Table 2.1 Radius Equations Calculations for the Two-Arm Equiangular Spiral Antenna

	$\theta$ (radians)	r1 (mm)	r2 (mm)		$\theta$ (radians)	r3 (mm)	r4 (mm)
0	0.00	1.0	0.7	$\pi$	3.14	1.0	0.7
$\pi/2$	1.57	1.5	1.0	$3\pi/2$	4.71	1.5	1.0
$\pi$	3.14	2.2	1.5	$2\pi$	6.28	2.2	1.5
$3\pi/2$	4.71	3.4	2.2	$5\pi/2$	7.85	3.4	2.2
$2\pi$	6.28	5.0	3.4	$3\pi$	9.43	5.0	3.4
$5\pi/2$	7.85	7.5	5.0	$7\pi/2$	11.00	7.5	5.0
$3\pi$	9.43	11.3	7.5	$4\pi$	12.57	11.3	7.5
$7\pi/2$	11.00	16.9	11.3	$9\pi/2$	14.14	16.9	11.3
$4\pi$	12.57	25.3	16.9	$5\pi$	15.71	25.3	16.9

### 2.3 Archimedean Spiral Antenna

Similar to the equiangular spiral antenna, the self-complementary planar Archimedean spiral antenna is also considered a frequency independent antenna because it satisfies both the angle and truncation requirements. The properties of the Archimedean spiral antenna are similar to those of the equiangular planar spiral antenna. Their differences are in the equations defining their arms and the parameters used to achieve a self-complementary structure.

### 2.3.1 Background Theory

An Archimedean spiral antenna can be defined by the spiral radius increasing uniformly with angle given by equation 2.10, where  $r_1$  is the inner radius of the spiral,  $r_0$  is proportionality constant for the growth rate, and  $\phi$  is the angle sweep with respect to the x axis [6].

$$r_a = r_0 \cdot \phi + r_1 \quad (2.10)$$

A rotation of the spiral curve of equation 2.10 generates the other edge of the spiral arm as shown by equation 2.11. Similarly, shifting the angle  $\phi$  of equations 2.10 and 2.11 by 180 degrees ( $\pi$ ) creates the second arm given by equations 2.12 and 2.13.

$$r_b = r_0 \cdot \phi + 2 \cdot r_1 \quad (2.11)$$

$$r_c = r_0 \cdot (\phi - \pi) + r_1 \quad (2.12)$$

$$r_d = r_0 \cdot (\phi - \pi) + 2 \cdot r_1 \quad (2.13)$$

In order to control the frequency of operation, the outer and inner radius  $r_2$  and  $r_1$ , respectively, must be defined. The outer radius  $r_2$  determines the low-frequency of operation, and the inner radius  $r_1$  determines the high frequency limit of operation. Equations 2.14 and 2.15 show the relation between radius and frequency of operation, where  $f_{\text{high}}$  and  $f_{\text{low}}$  are the high and low end frequencies of the operating range, respectively, and “c” is the speed of light equal to  $3 \times 10^8$  m/s. In practice, the low frequency point can be greater than predicted by equation 2.15 due to reflections from the end of the spiral, which could be minimized by using resistive loading at the end of each arm or by adding conductivity loss to some part of the outer turn of each arm [6].

Likewise, the high frequency limit may be less than predicted by equation 2.14 due to feed region effects [6].

$$r_1 = \frac{c}{2\pi \cdot f_{\text{high}}} \quad (2.14)$$

$$r_2 = \frac{c}{2\pi \cdot f_{\text{low}}} \quad (2.15)$$

Moreover, the width of each arm and the spacing between each turn are set equal to obtain a self-complementary structure. The width and space of each arm are defined by equation 2.16. Since frequency independent behavior is best achieved when the inner radius is equal to the strip width or spacing between turns [6],  $r_1$  is established by equation 2.17. The proportionality constant for the growth rate  $r_0$  is given by equation 2.18.

$$W = \frac{r_2 - r_1}{4 \cdot N} \quad (2.16)$$

$$r_1 = \frac{r_2}{4 \cdot N + 1} \quad (2.17)$$

$$r_0 = \frac{2 \cdot W}{\pi} \quad (2.18)$$

By metalizing the areas between spiral curves “a” and “b” (equations 2.10 and 2.11 respectively) and between spiral curves “c” and “d” (equations 2.12 and 2.13 respectively), with the other areas open, we obtain a two-arm Archimedean spiral antenna as shown on figure 2.4.

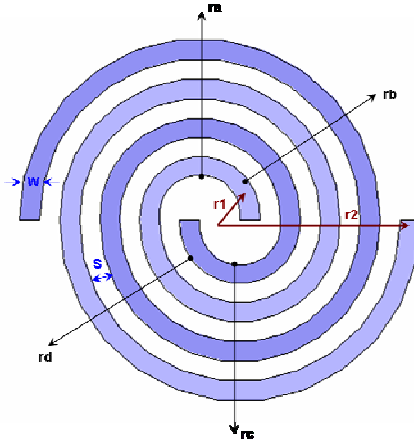


Figure 2.4 Frequency-Independent Planar Self-Complementary Archimedean Spiral Antenna

The radiations from the nearly equal and opposite currents at the feed point separated by the growing spiral arms cancel in the far field. When the perimeter of the turn approaches one wavelength, the out-of-phase currents become in phase so that the currents no longer cancel in the far field. This condition continues for some distance after the  $1\lambda$  perimeter point [3]. The spiral radiates RHC (Right Hand Circular) polarization on one side and LHC (Left Hand Circular) polarization on the other side [3]. One of these polarizations is eliminated when the antenna is mounted over a cavity. In order to determine the sense of the circular polarization, let your fingers roll in the direction of the spiral with the tips toward increasing radius and the thumb points to the pattern maximum [3]. The Archimedean spiral shown on figure 2.4 radiates RHC polarization.

### 2.3.2 Design

The frequency range of interest is from 2 to 6GHz. By plugging these frequencies of interest into equations 2.14 to 2.18, we obtain the parameters necessary to design the antenna. Table 2.2 shows the calculated parameters for the Archimedean spiral antenna. The number of turns “N” was set to two. Table 2.3 shows the calculated radius equations for the two-arm spiral antenna, where ra through rd corresponds to equations 2.10 to 2.13

respectively. Units are specified in mm. The physical dimensions of the equiangular spiral antenna are 53.1mm x 47.7mm.

Table 2.2 Calculated Design Parameters for the Archimedean Spiral Antenna

Parameter	Value (mm)
r1	2.653
r2	23.873
W	2.653
S	2.653
ro	1.689

Table 2.3 Radius Equations Calculations for the Two-Arm Archimedean Spiral

	$\theta$ (radians)	ra (mm)	rb (mm)		$\theta$ (radians)	rc (mm)	rd (mm)
0	0.00	2.7	5.3	$\pi$	3.14	2.7	5.3
$\pi/2$	1.57	5.3	8.0	$3\pi/2$	4.71	5.3	8.0
$\pi$	3.14	8.0	10.6	$2\pi$	6.28	8.0	10.6
$3\pi/2$	4.71	10.6	13.3	$5\pi/2$	7.85	10.6	13.3
$2\pi$	6.28	13.3	15.9	$3\pi$	9.43	13.3	15.9
$5\pi/2$	7.85	15.9	18.6	$7\pi/2$	11.00	15.9	18.6
$3\pi$	9.43	18.6	21.2	$4\pi$	12.57	18.6	21.2
$7\pi/2$	11.00	21.2	23.9	$9\pi/2$	14.14	21.2	23.9
$4\pi$	12.57	23.9	26.5	$5\pi$	15.71	23.9	26.5

#### 2.4 Electromagnetic Design and Simulations of Equiangular Spiral Antenna

In order to perform an electromagnetic simulation of the antenna design, the program Ansoft HFSS (High Frequency Structure Simulator) was used. HFSS employs the Finite Element Method (FEM) for the EM simulations of arbitrary 3D volumetric passive devices [7]. Its basic mesh element is a tetrahedron, which allows solving arbitrary 3D geometries involving complex curves and shapes [7].

The two-arm equiangular spiral antenna was drawn in HFSS using the calculated radius equations presented on table 2.1. The substrate was defined as the Rogers 5880 RT Duroid with  $\epsilon_r$  equal to 2.2. The metal thickness was set to 1.7 mils. Additionally, the preliminary simulations of the spiral antenna utilize the traditional  $\lambda/4$  cavity backed implementation, which introduces a fixed length in terms of  $\lambda$  limiting the frequency

independent characteristics of the antenna [8]. The  $\lambda/4$  substrate thickness was calculated at 2.4 GHz to be equal to 24.7mm.

In addition to generating a precise 3D drawing of the antenna to be characterized, boundary conditions represent a major area of concern with efficiently and correctly modeling an antenna in HFSS. Boundary conditions specify the field behavior on the surfaces of the problem region and object interfaces [7]. The wave equation that is solved by Ansoft HFSS is derived from the differential form of Maxwell's equations [7]. For these expressions to be valid, it is assumed that the field vectors are single-valued, bounded, and have continuous distribution along with their derivatives [7]. Then, boundary conditions define the field behavior across discontinuous boundaries [7].

There are two types of boundaries that need to be considered and defined properly in order to accurately simulate an antenna in HFSS. The first type of boundary is the excitation port that permits energy to flow into and out of a structure [7]. The second type of boundary is the radiation surface or absorbing boundary that enables modeling a surface as electrically open so that waves can radiate out of the structure and toward the radiation boundary [7]. When radiation boundaries are included in a structure simulation, calculated S-parameters include the effects of radiation loss [7]. In addition, the radiation boundary can be assigned to a 3D box enclosing the radiating structure (the spiral antenna in this case) at a radial distance  $\lambda/4$  in every direction as shown by figure 2.5.

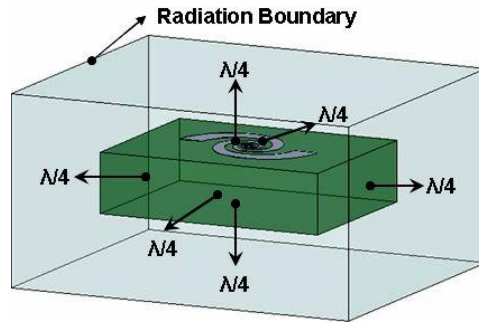


Figure 2.5 Radiation Boundary Assignment for the Equiangular Spiral Antenna

There are two types of excitation boundaries in HFSS: one is external or wave port and the other one is internal or lumped port. Since spiral antennas are conventionally fed in the center of the spiral, an initial simple feeding was created with a lumped port assignment at the center of the spiral represented by a 2D rectangular surface as shown by figure 2.6. A terminal line was defined to create a voltage polarity reference in the port boundary. The arrow head is synonymous with “+” and the arrow base is synonymous with “-”.

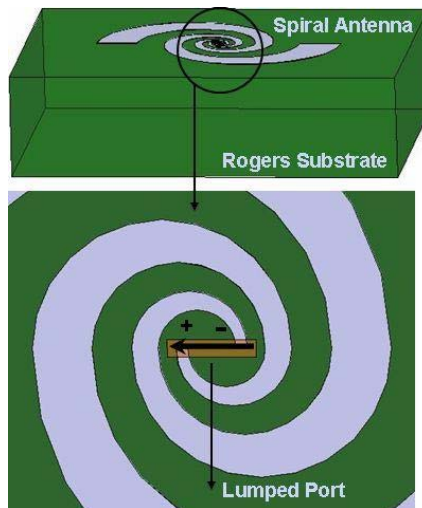


Figure 2.6 Lumped Port Assignment for the Equiangular Spiral Antenna

### 2.4.1 S-parameter Simulations

The scattering matrix is used to provide a complete description of an N-port network as seen at its N ports [9]. Furthermore, the scattering [S] matrix relates the voltage waves incident on the ports to those reflected from the ports as stated by equation 2.19, where  $V_n^-$  and  $V_n^+$  are the amplitudes of the voltage waves reflected and incident on port n respectively [9]. For a 1-port network such as an antenna, the scattering parameter of interest is the reflection coefficient or  $S_{11}$  defined as the amplitude of the reflected voltage wave  $V_1^-$  coming out of port 1 to the incident voltage wave  $V_1^+$  going into port 1 when all other ports are terminated in matched loads as shown by equation 2.20 [9]. The reflection coefficient is also represented as  $\Gamma^{(1)} (V_2^+=0)$  [9].

$$[V_n^-] = [S] [V_n^+] \quad (2.19)$$

$$S_{11} = V_1^- / V_1^+ (V_2^+=0) \quad (2.20)$$

The return loss (RL) in dB defined by equation 2.21 describes the reduction in the amplitude of the reflected energy as compared to the forward energy due to the mismatch between the transmission line characteristic impedance and the load impedance. When  $\Gamma$  is equal to zero the load is matched to the line, so there is no reflected power and the return loss equals  $\infty$  dB. When the magnitude of  $\Gamma$  is equal to 1 all incident power is reflected, so the return loss equals 0 dB [9].

$$RL = -20 \log(|\Gamma|) \cdot \text{dB} \quad (2.21)$$

A flat metal sheet is used in many antennas as a ground plane. Therefore, simulations have been performed with a ground plane located approximately a quarter-wavelength from the antenna, and without a ground plane, in order to compare the different and expected antenna performance. Figure 2.7 shows  $S_{11}$  in dB and phase for the

equiangular spiral antenna having a  $\lambda/4$  thick substrate<sup>2</sup> with and without a ground plane present. The equiangular spiral antenna has a return loss of less than 5dB for a frequency range from 2 to 6 GHz. The effect of backing the antenna with a ground plane is illustrated by the blue trace in both plots shown on figure 2.7. For instance, the highest resonance for the antenna backed by a  $\lambda/4$  thick substrate occurs at 2.2 GHz where  $S_{11}$  equals -18.6dB. Conversely, there are two distinctive resonances for the antenna backed by a  $\lambda/4$  thick substrate and a ground plane occurring at 1.9 and 4.6 GHz where  $S_{11}$  equals -17.61 and -17.73 dB respectively.

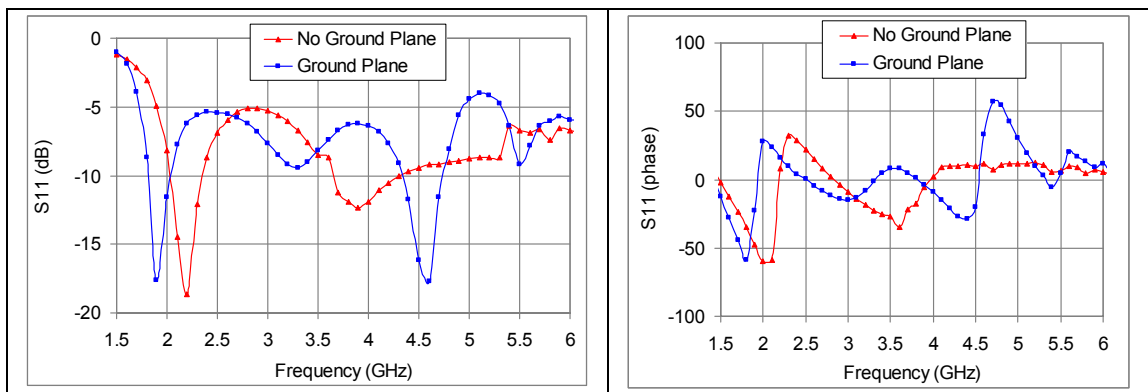


Figure 2.7 S-parameter Simulations for the Equiangular Spiral Antenna. Red Trace- Antenna Backed by a  $\lambda/4$  Thick Substrate. Blue Trace- Antenna Backed by a  $\lambda/4$  Thick Substrate and a Ground Plane. Left Plot- Return Loss (dB). Right Plot- Return Loss (phase)

Input impedance is defined as the impedance presented by an antenna at its terminals or the ratio of the voltage to current at a pair of terminals as demonstrated by equation 2.22, where  $Z_A$  is the antenna impedance,  $R_A$  is the antenna resistance, and  $X_A$  is the antenna reactance at its terminals [5]. The resistive part of the antenna impedance ( $R_A$ ) consists of two components as shown by equation 2.23, where  $R_r$  is the radiation resistance and  $R_L$  is the loss resistance of the antenna [5].

<sup>2</sup> The  $\lambda/4$  thickness was calculated at 2.4 GHz for the Rogers 5880 material (dielectric constant equal to 2.2) to be equal to 24.7 mm.

$$Z_A = R_A + j \cdot X_A \quad (2.22)$$

$$R_A = R_T + R_L \quad (2.23)$$

Figure 2.8 shows the simulated input impedance for the equiangular spiral antenna having a  $\lambda/4$  thick substrate with and without a ground plane present. For a frequency-independent self-complementary spiral, the input impedance should be flat over a wide frequency range. This trend is better represented by the antenna design without the ground plane as shown by the red trace on both plots of figure 2.8, since the impedance follows a more constant flat trace between 3.5 and 6 GHz.

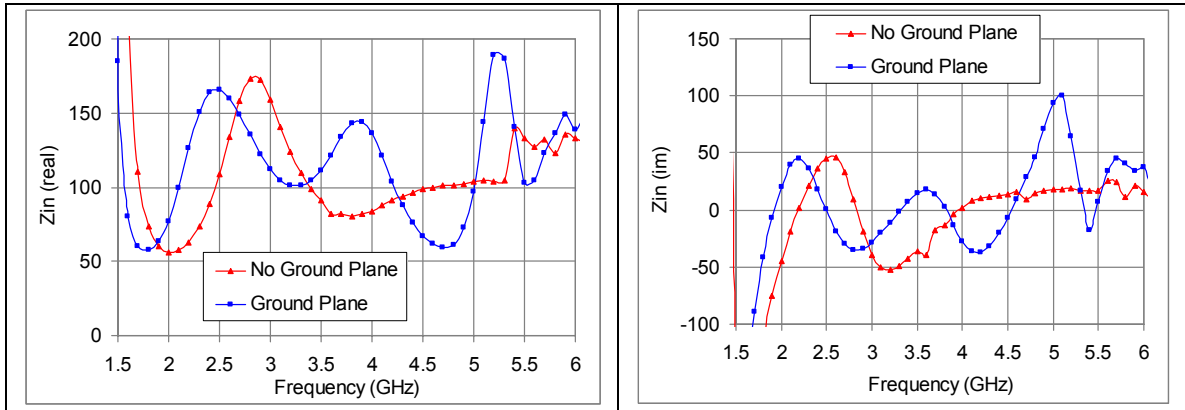


Figure 2.8 Input Impedance Simulations for the Equiangular Spiral Antenna. Red Trace- Antenna Backed by a  $\lambda/4$  Thick Substrate. Blue Trace- Antenna Backed by a  $\lambda/4$  Thick Substrate and a Ground Plane. Left Plot- Input Impedance (real). Right Plot- Input Impedance (imaginary)

The voltage standing wave ratio (VSWR) is a measure of the mismatch of a line and can be defined by equation 2.24 to be a real number such that  $1 \leq \text{VSWR} \leq \infty$  [9]. Matched impedances give ideal power transfer that translates into a value of VSWR equal to 1. On the contrary, mismatched impedances represent reduced power transfer that translates into a high value of VSWR.

$$\text{VSWR} = \frac{1 + |\Gamma|}{1 - |\Gamma|} \quad (2.24)$$

The voltage standing wave ratio is typically used to measure antenna bandwidth [6]. Figure 2.9 shows the simulated VSWR for the equiangular spiral antenna having a  $\lambda/4$  thick substrate with and without a ground plane present. For the antenna without the ground plane present, the VSWR referenced to 50 ohms is less than 3 except for the frequency range between 2.6-3.1 GHz. On the other hand, for the antenna with a ground plane present, the VSWR referenced to 50 ohms is less than 3 except for two frequency ranges between 2.3-2.7 GHz and 4.9-6 GHz.

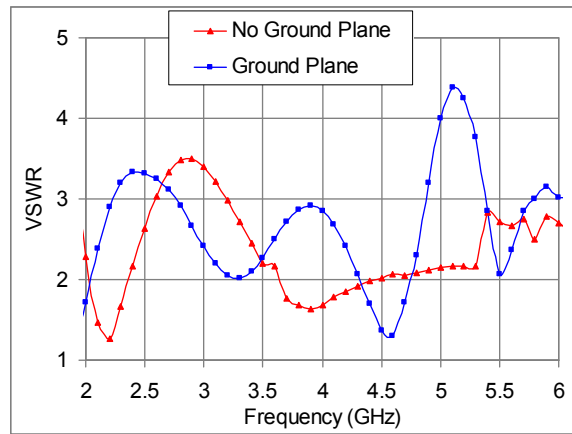


Figure 2.9 Simulated VSWR for the Equiangular Spiral Antenna. Red Trace- Antenna Backed by a  $\lambda/4$  Thick Substrate. Blue Trace- Antenna Backed by a  $\lambda/4$  Thick Substrate and a Ground Plane

#### 2.4.2 Radiation Pattern Simulations

An antenna radiation pattern is a graphical representation of the radiation properties of the antenna, such as radiation intensity and directivity phase or polarization, as a function of space coordinates [5]. An amplitude field pattern is a graph of the spatial variation of the electric or magnetic fields along a constant radius [5]. In most cases, radiation and field patterns are determined in the far-field region, which is the region of the field of the antenna where the angular field distribution is essentially independent of the distance from the antenna [5]. The far-field region is commonly taken to exist at



pattern, which is the spatial distribution of the polarizations of a field vector excited (radiated) by an antenna taken over its radiation sphere [5]. At each point on the radiation sphere the polarization is usually resolved into a pair of orthogonal polarizations, the co-polarization and cross polarization [5].

There are three types of polarization; linear, circular, and elliptical polarizations. A time-harmonic wave is circularly polarized at a given point in space if the electric or magnetic field vector at that point traces a circle as a function of time [5]. The necessary and sufficient conditions to accomplish this type of polarization are that the electric or magnetic field vector must have two orthogonal linear components which must have the same magnitude and a time-phase difference of odd multiples of 90 degrees [5]. Spiral antennas exhibit circular polarization. The sense of the spiral wrap and the direction of current flow determine the circular polarization sense [3].

The mode number of a spiral refers to the number of  $2\pi$  (radians) or  $360^\circ$  (degrees) cycles that occur in the feed phasing when processing through the arms CCW (counterclockwise) [3]. For instance, mode 1 phases in a two-arm spiral are  $0^\circ$  and  $180^\circ$ . Moreover, the phase difference moving CCW between arms is found from the mode number  $m$  and the number of arms  $N$  as shown by equation 2.25 [3]. We determine the mode radiating by the phase slope. RHC polarization produces a negative slope as  $\phi$  increases (CCW rotation) [3]. We use the convention that positive modes radiate RHC and negative modes radiate LHC and place the negative sign in the mode expressions.

$$\text{phase} = -\frac{2 \cdot \pi \cdot m}{N} \tag{2.25}$$

“The number of arms equals the number of independent modes. An axially symmetrical antenna such as a spiral can radiate these modes when we phase the feeding of the ports to match the phase rotation of the mode [3]”. For Instance, a two-arm spiral antenna has modes +1 and -1, which produce the same phasing at the feed points of the spiral:  $0^\circ$  and  $180^\circ$ . The spiral wrap direction determines the polarization radiated [3]. Similarly, all odd-order (... , -3, -1, 1, 3, 5, ...) modes have the same phasing on two feeds, which means that the two-arm spiral will radiate these modes efficiently if current flows on the arms where the spiral circumference is the same integer number of wavelengths [3]. Therefore, whenever the circumference of a two-arm spiral is an odd-integer multiple of a wavelength the currents radiate. The two-arm spiral suppresses the even modes but allows radiation of odd modes [3].

Figure 2.11 shows the simulated total far-field radiation patterns versus Theta at 2.4GHz for the equiangular spiral antenna backed by a  $\lambda/4$  thick substrate with and without a ground plane present. The equiangular spiral antenna backed by a  $\lambda/4$  thick substrate without the ground plane present shows an expected total gain pattern characterized by a major and a minor circular lobe. The maximum total gain at 2.4GHz is 4dB and occurs at a Theta angle equal to  $180^\circ$  for both  $0^\circ$  and  $90^\circ$  Phi angles due to the dielectric backing the antenna. If the dielectric constant of the substrate backing the antenna is increased, then the maximum total gain gets re-directed to a Theta angle of  $0^\circ$  because the thickness of the substrate decreases and less energy tends to be stored in the substrate. On the other hand, the equiangular spiral antenna backed by a  $\lambda/4$  thick substrate and a ground plane shows an expected total gain pattern characterized by a single major circular lobe and an almost non-existent minor lobe due to the presence of

the ground plane. Making the ground plane infinitely long would make the minor lobe disappear. The maximum total gain at 2.4GHz is 7dB and occurs at a Theta angle equal to  $0^\circ$  for both  $0^\circ$  and  $90^\circ$  Phi angles. As it is shown by figure 2.11, the presence of a ground plane redirects one-half of the radiation into the opposite direction, improving the antenna gain by about 3dB [17]. Figures 2.12 and 2.13 show the side, front, and top views of the simulated radiation patterns in 3D at 2.4GHz for the equiangular spiral antenna backed by a  $\lambda/4$  thick substrate without and with a ground plane present respectively.

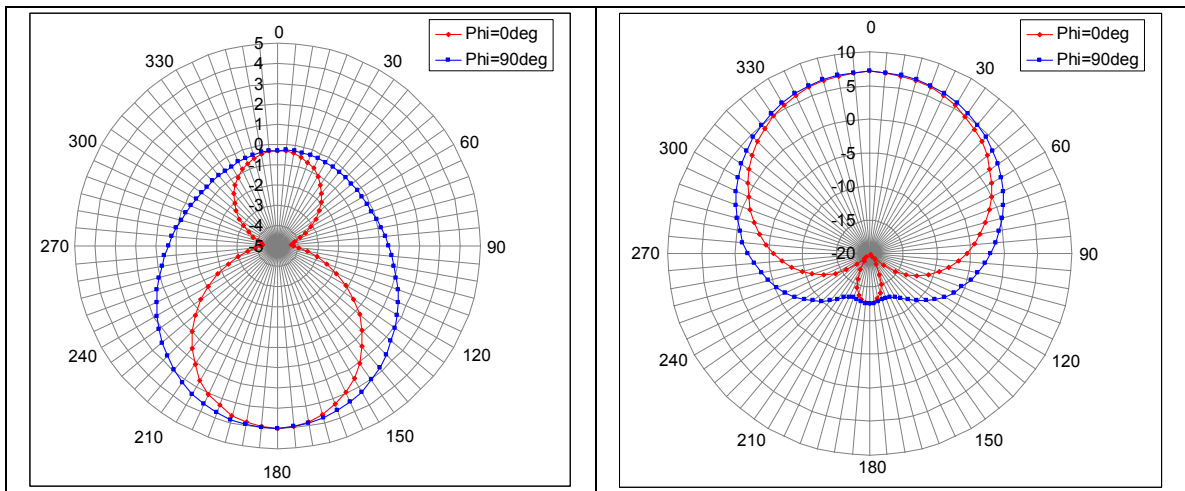


Figure 2.11 Simulated Radiation Pattern Versus Theta at 2.4GHz for the Equiangular Spiral Antenna. Red Trace- Phi = 0deg. Blue Trace- Phi = 90deg. Left Plot- Antenna Backed by a  $\lambda/4$  Thick Substrate. Right Plot- Antenna Backed by a  $\lambda/4$  Thick Substrate and a Ground Plane

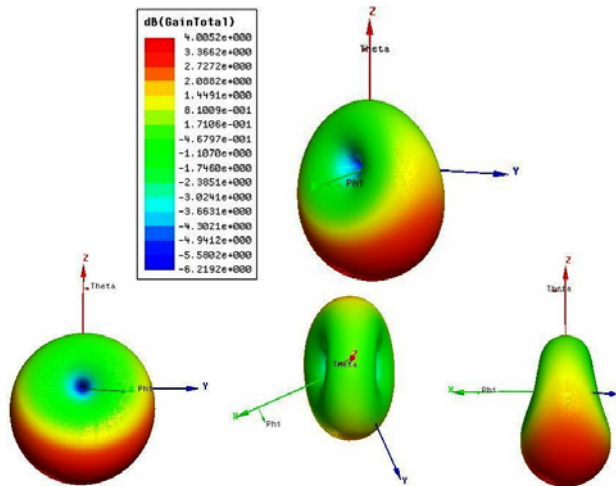


Figure 2.12 Side, Front, and Top Views of Simulated Radiation Pattern in 3D at 2.4GHz for the Equiangular Spiral Antenna Backed by a  $\lambda/4$  Thick Substrate

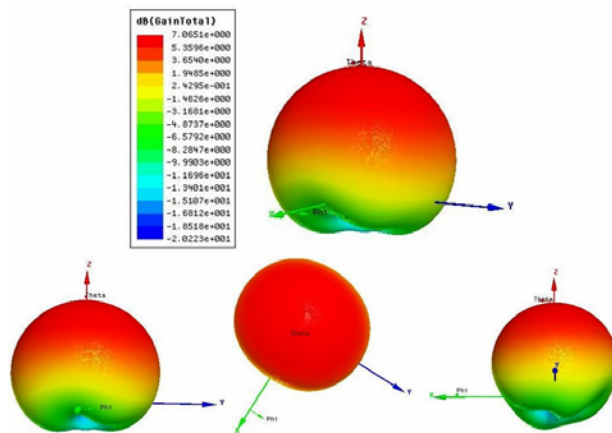


Figure 2.13 Side, Front, and Top Views of Simulated Radiation Pattern in 3D at 2.4GHz for the Equiangular Spiral Antenna Backed by a  $\lambda/4$  Thick Substrate and a Ground Plane

### 2.4.3 Antenna Parameters Simulations

Peak directivity or maximum directivity  $D_0$  is a measure that describes only the directional properties of the antenna, and it is therefore controlled by the pattern [5].  $D_0$  is defined as the ratio of the maximum radiation intensity from the antenna to the radiation intensity averaged over all directions, where the averaged radiation intensity is equal to the total power radiated by the antenna divided by  $4\pi$  [5]. In mathematical form,  $D_0$  can

be expressed as equation 2.26, where  $U_{\max}$  is the maximum radiation intensity (W/unit solid angle) and  $P_{\text{rad}}$  is the total radiated power (W) [5].

$$D_o = \frac{4 \cdot \pi \cdot U_{\max}}{P_{\text{rad}}} \quad (\text{dimensionless}) \quad (2.26)$$

Peak Gain  $G_o$  is a measure of the antenna performance that takes into account the efficiency as well as the directional capabilities of the antenna as shown by equation 2.27, where  $e_{\text{cd}}$  is the antenna radiation efficiency (dimensionless) [5]. The antenna radiation efficiency accounts for the conduction and dielectric efficiency, so gain does not include losses arising from impedance mismatches (reflection losses) and polarization mismatches (losses) [5]. Equation 2.28 converts gain from a dimensionless quantity to decibels.

$$G_o = e_{\text{cd}} \cdot D_o \quad (\text{dimensionless}) \quad (2.27)$$

$$G_o(\text{dB}) = 10 \cdot \log(e_{\text{cd}} \cdot D_o) \quad (2.28)$$

Figure 2.14 shows the simulated total maximum gain (dB) versus frequency for the equiangular spiral antenna. The spiral antenna backed by a  $\lambda/4$  thick substrate and without a ground plane present shows a total maximum gain increasing with frequency as expected. The gain increases from 3 to 12 dB between 2 to 5.4 GHz. Similarly, the spiral antenna backed by a  $\lambda/4$  thick substrate and a ground plane shows the increasing trend of total maximum gain versus frequency except for the frequency range between 4 to 5 GHz. The gain increases from 6.7 to 11.7 dB between 2 to 6GHz. The low gain response between 4 to 5 GHz for the antenna backed by a ground plane shown suggests that at  $\Phi = 0^\circ$  and  $\Theta = 0^\circ$  there is a null in the radiation pattern. This distortion in the radiation pattern could be due to the fact that at this frequency range the substrate backing up the

antenna is  $\lambda/2$  electrically long instead of  $\lambda/4$ , which will put the antenna closer to the ground plane electrically. Therefore, the image currents on the ground plane tend to cancel the currents in the antenna resulting in this low gain.

Axial ratio is a very important parameter for spiral antennas since it indicates the type of polarization the antenna exhibits. Moreover, it is defined as the ratio of the major to the minor axis of the polarization ellipse. The axial ratio value range varies from 1 to infinity, where 1 (0 dB) indicates that the electric field is circularly polarized and a value of infinity indicates that the electric field is linearly polarized. For instance, spiral antennas should have an axial ratio less than 5dB to be considered a circularly polarized antenna with a bidirectional radiation pattern broadside to the plane of the spiral. The designed equiangular spiral antenna radiates RHC polarization based on the spiral wrap direction.

Figure 2.15 shows the simulated axial ratio (dB) versus frequency at the Theta and Phi angle position where total gain is maximum for the equiangular spiral antenna. The spiral antenna backed by a  $\lambda/4$  thick substrate and without a ground plane present has linear polarization from 2 to 3.5 GHz and from 4.5 to 6GHz. However, it has circular polarization from 3.5 to 4.5 GHz. Furthermore, the spiral antenna backed by a  $\lambda/4$  thick substrate and a ground plane has linear polarization from 2 to 2.2 GHz and from 3.1 to 5.3 GHz. It has circular polarization from 2.3 to 3GHz and from 5.4 to 6GHz.

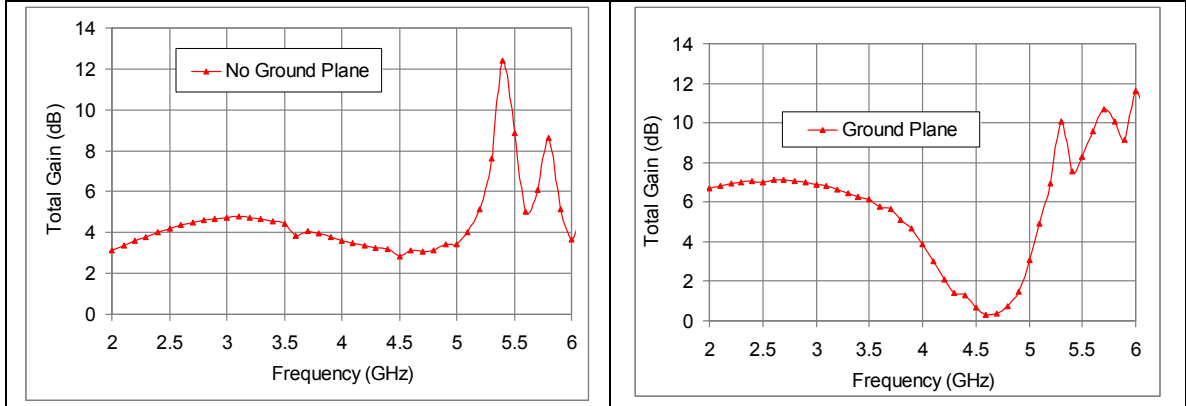


Figure 2.14 Simulated Total Gain (dB) Versus Frequency for the Equiangular Spiral Antenna. Left Plot- Antenna Backed by a  $\lambda/4$  Thick Substrate Simulated at  $\Phi = 0^\circ$  and  $\Theta = 180^\circ$ . Right Plot- Antenna Backed by a  $\lambda/4$  Thick Substrate and a Ground Plane Simulated at  $\Phi = 0^\circ$  and  $\Theta = 0^\circ$

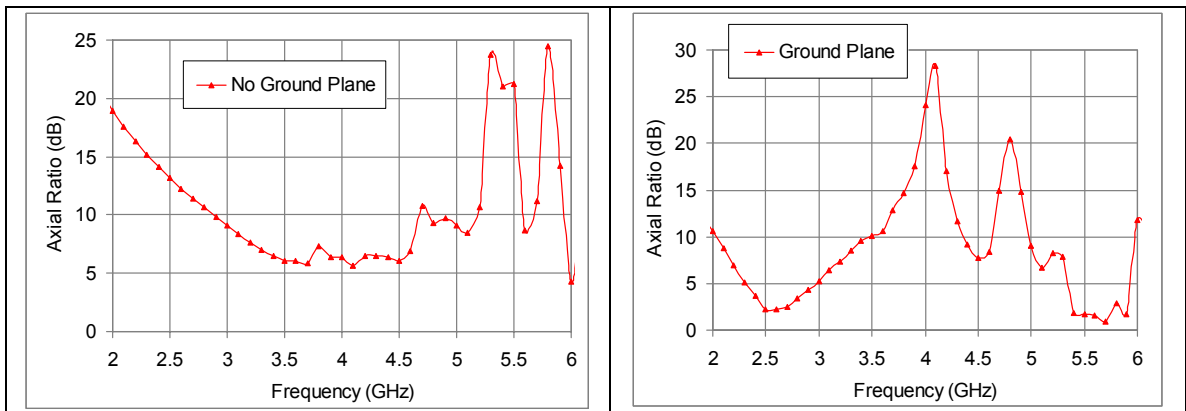


Figure 2.15 Simulated Axial Ratio (dB) Versus Frequency for the Equiangular Spiral Antenna. Left Plot- Antenna Backed by a  $\lambda/4$  Thick Substrate Simulated at  $\Phi = 0^\circ$  and  $\Theta = 180^\circ$ . Right Plot- Antenna Backed by a  $\lambda/4$  Thick Substrate and a Ground Plane Simulated at  $\Phi = 0^\circ$  and  $\Theta = 0^\circ$

## 2.5 Electromagnetic Design and Simulations of Archimedean Spiral Antenna

The two-arm Archimedean spiral antenna was drawn in HFSS using the calculated radius equations presented in table 2.2. The substrate was defined as the Rogers 5880 RT Duroid with  $\epsilon_r$  equal to 2.2. The metal thickness was set to 1.7 mils. Additionally, the preliminary simulations of the spiral antenna utilize the traditional  $\lambda/4$  cavity backed implementation. The  $\lambda/4$  substrate thickness was calculated at 2.4 GHz to be equal to 21.07mm.

The radiation boundary was assigned to a 3D box enclosing the radiating structure (the spiral antenna in this case) at a radial distance  $\lambda/4$  in every direction as shown by figure 2.16. Additionally, an initial simple feeding was created with a lumped port assignment at the center of the spiral represented by a 2D rectangular surface as shown by figure 2.17. A terminal line was defined to create a voltage polarity reference in the port boundary.

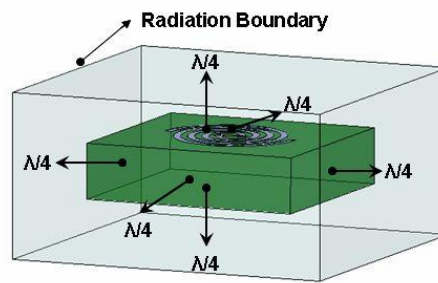


Figure 2.16 Radiation Boundary Assignment for the Archimedean Spiral Antenna

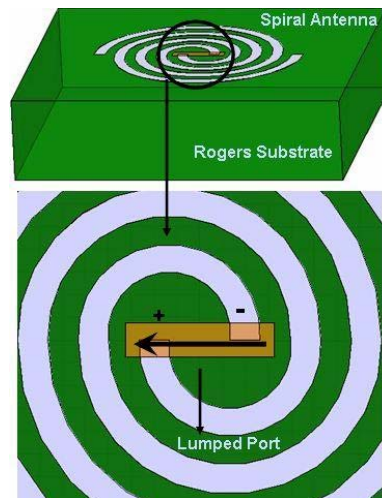


Figure 2.17 Lumped Port Assignment for the Archimedean Spiral Antenna

### 2.5.1 S-parameter Simulations

Figure 2.18 shows the return loss in dB and phase for the Archimedean spiral antenna having a  $\lambda/4$  thick substrate with and without a ground plane present. The

Archimedean spiral antenna has a return loss of less than 5dB for a frequency range from 2 to 6 GHz. The effect of backing the antenna with a ground plane is illustrated by the blue trace in both plots shown on figure 2.18. For instance, the highest resonance for the antenna backed by a  $\lambda/4$  thick substrate occurs at 2.4 GHz where  $S_{11}$  equals -7.9 dB. Conversely, there are two high resonances for the antenna backed by a  $\lambda/4$  thick substrate and a ground plane that occur at 2.25 and 3.05 GHz where  $S_{11}$  equals -12.18 and -16.56 dB respectively.

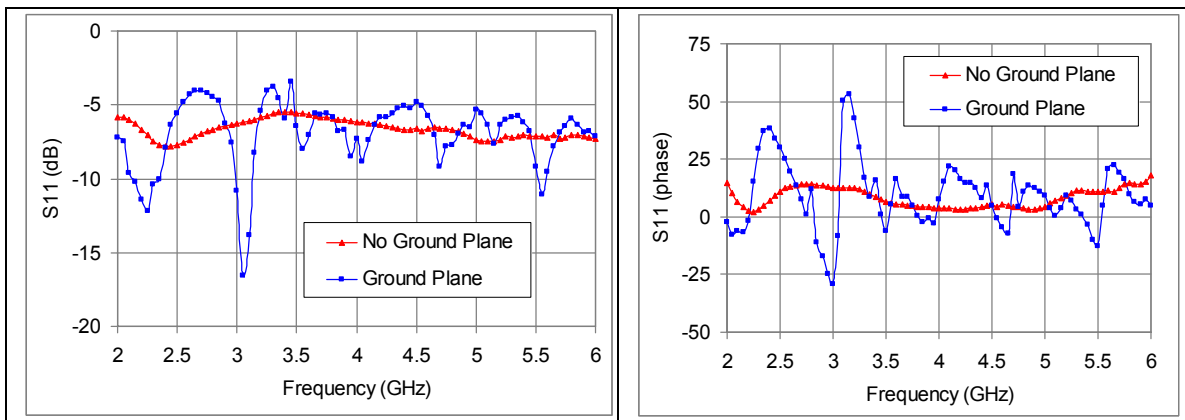


Figure 2.18 S-parameter Simulations for the Archimedean Spiral Antenna with and without a Ground Plane. Red Trace- Antenna Backed by a  $\lambda/4$  Thick Substrate. Blue Trace- Antenna Backed by a  $\lambda/4$  Thick Substrate and a Ground Plane. Left Plot- Return Loss (dB). Right Plot- Return Loss (phase)

Figure 2.19 shows the simulated input impedance for the Archimedean spiral antenna having a  $\lambda/4$  thick substrate with and without a ground plane present. For a frequency-independent self-complementary spiral, the input impedance should be flat over a wide frequency range. This trend is better represented by the antenna design without the ground plane as shown by the red trace on both plots of figure 2.19, since the impedance follows a more constant flat trace from 2 to 6 GHz.

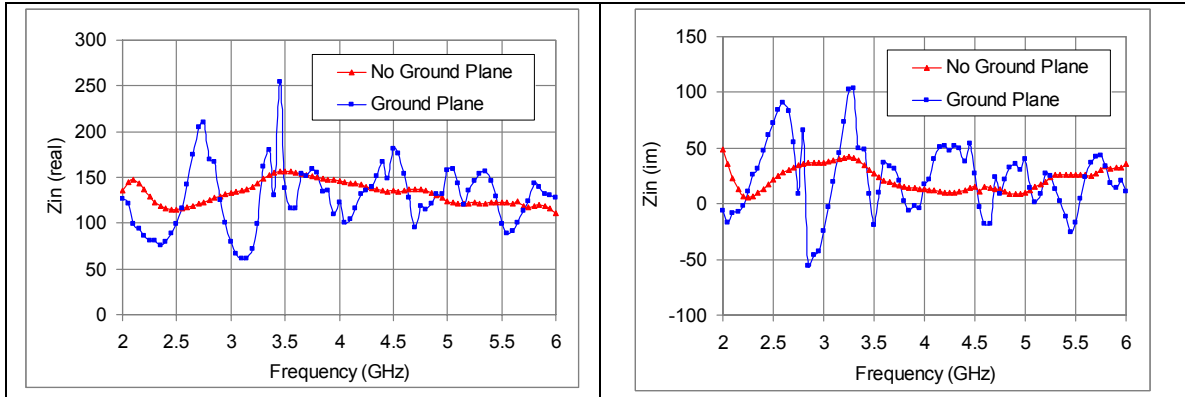


Figure 2.19 Input Impedance Simulations for the Archimedean Spiral Antenna with and without a Ground Plane. Red Trace- Antenna Backed by a  $\lambda/4$  Thick Substrate. Blue Trace- Antenna Backed by a  $\lambda/4$  Thick Substrate and a Ground Plane. Left Plot- Input Impedance (real). Right Plot- Input Impedance (imaginary)

Figure 2.20 shows the simulated VSWR for the Archimedean spiral antenna having a  $\lambda/4$  thick substrate with and without a ground plane present. For the antenna without the ground plane present, the VSWR referenced to 50 ohms is less than 3 except for the frequency range between 3.2 to 3.75GHz. On the other hand, for the antenna with a ground plane present, the VSWR referenced to 50 ohms is less than 5.

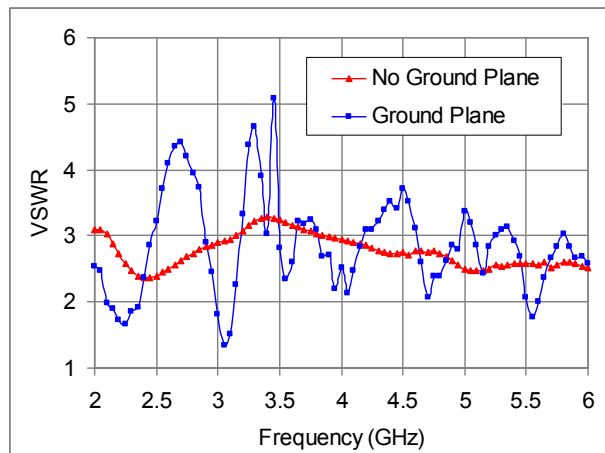


Figure 2.20 Simulated VSWR for the Archimedean Spiral Antenna with and without a Ground Plane. Red Trace- Antenna Backed by a  $\lambda/4$  Thick Substrate. Blue Trace- Antenna Backed by a  $\lambda/4$  Thick Substrate and a Ground Plane

### 2.5.2 Radiation Pattern Simulations

The Archimedean and the equiangular spiral antennas share similar radiation pattern characteristics. For instance, they exhibit maximum gain peaks at a theta angle equal to 180 degrees for the configuration without a ground plane present and at a theta angle equal to 0 degrees for the configuration with a ground plane present, which indicates that the presence of a ground plane redirects the direction of maximum gain by 180 degrees. Also, as it is shown by figures 2.11 and 2.21, the Archimedean spiral antenna has slightly higher gain peaks than the equiangular spiral. In addition, the presence of a ground plane improved the antenna gain of the Archimedean and equiangular spiral antennas by about 3dB at 2.4GHz.

Figure 2.21 shows the simulated total far-field radiation patterns versus Theta at 2.4GHz for the Archimedean spiral antenna backed by a  $\lambda/4$  thick substrate with and without a ground plane present. The Archimedean spiral antenna backed by a  $\lambda/4$  thick substrate without the ground plane present shows an expected total gain pattern characterized by a major and a minor circular lobe. The maximum total gain at 2.4GHz is 4.26dB and occurs at a Theta angle equal to 180° for both 0° and 90° Phi angles. On the other hand, the Archimedean spiral antenna backed by a  $\lambda/4$  thick substrate and a ground plane shows an expected total gain pattern characterized by a single major circular lobe and an almost non-existent minor lobe due to the presence of the ground plane. The maximum total gain at 2.4GHz is 7.11dB and occurs at a Theta angle equal to 0° for both 0° and 90° Phi angles. Figures 2.22 and 2.23 show the side, front, and top views of the simulated radiation patterns in 3D at 2.4GHz for the Archimedean spiral antenna backed by a  $\lambda/4$  thick substrate without and with a ground plane present respectively.

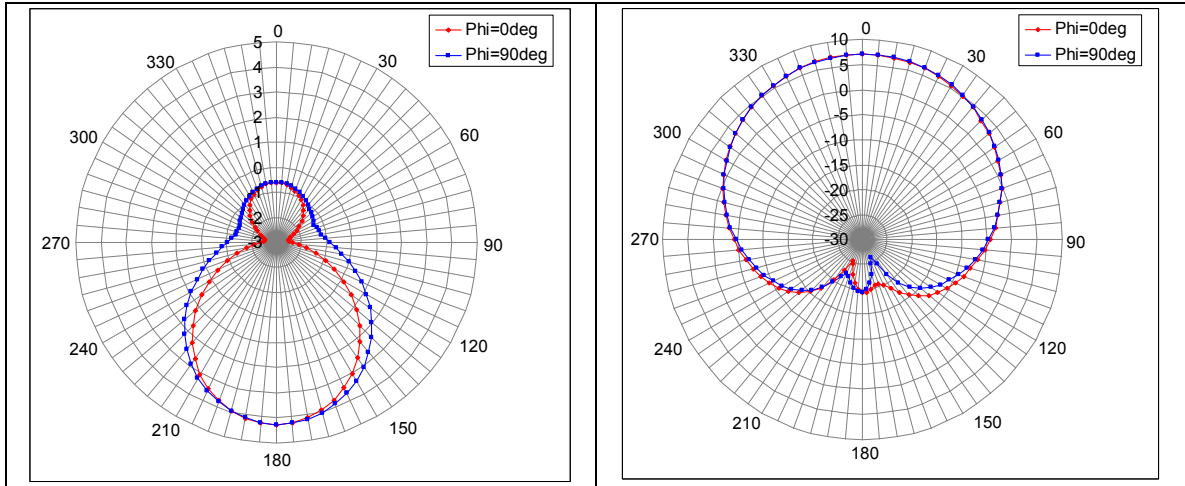


Figure 2.21 Simulated Radiation Pattern Versus Theta at 2.4GHz for the Archimedean Spiral Antenna with and without a Ground Plane. Red Trace- Phi = 0deg. Blue Trace- Phi = 90deg. Left Plot- Antenna Backed by a  $\lambda/4$  Thick Substrate. Right Plot- Antenna Backed by a  $\lambda/4$  Thick Substrate and a Ground Plane

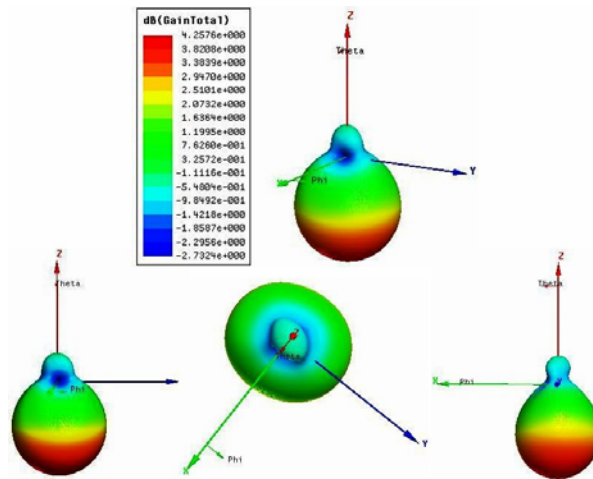


Figure 2.22 Side, Front, and Top Views of Simulated Radiation Pattern in 3D at 2.4GHz for the Archimedean Spiral Antenna Backed by a  $\lambda/4$  Thick Substrate

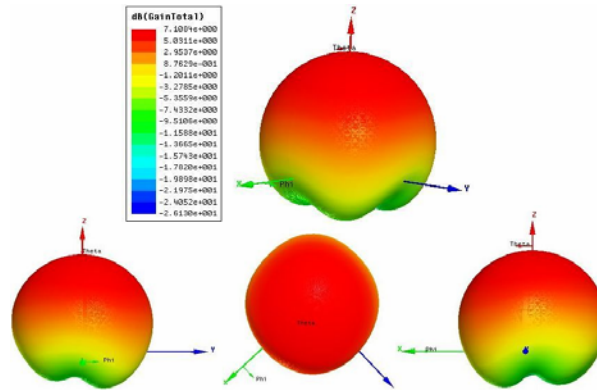


Figure 2.23 Side, Front, and Top Views of Simulated Radiation Pattern in 3D at 2.4GHz for the Archimedean Spiral Antenna Backed by a  $\lambda/4$  Thick Substrate and a Ground Plane

### 2.5.3 Antenna Parameters Simulations

The Archimedean spiral antenna has similar gain versus frequency response to the equiangular spiral antenna. The increasing trend of total maximum gain with frequency is present for the equiangular and Archimedean spiral antennas regardless of the presence of a conductive ground plane. Additionally, the Archimedean spiral antenna holds the same low gain performance as the equiangular spiral antenna at a frequency range where the substrate backing up the antenna is  $\lambda/2$  electrically long instead of  $\lambda/4$ . However, this distortion in the gain is more noticeable for the Archimedean spiral antenna as shown by figure 2.24, which could be due to the Archimedean spiral antenna arms being closer to the edge of the substrate so the image currents on the ground plane could cancel the currents in the antenna to a greater extent.

Figure 2.24 shows the simulated total maximum gain (dB) versus frequency for the Archimedean spiral antenna. The gain increases from 3.66 to 7.75 dB between 2 to 5.85 GHz. Similarly, the spiral antenna backed by a  $\lambda/4$  thick substrate and a ground plane shows the increasing trend of total maximum gain versus frequency except for the frequency range between 3.7 to 4.455 GHz. The gain increases from 7.2 to 11.9 dB

between 2 to 5.7 GHz. The low gain response between 4 to 5 GHz for the antenna backed by a ground plane shown in figure 2.24 implies that at  $\Phi = 0^\circ$  and  $\Theta = 0^\circ$  there is a null in the radiation pattern.

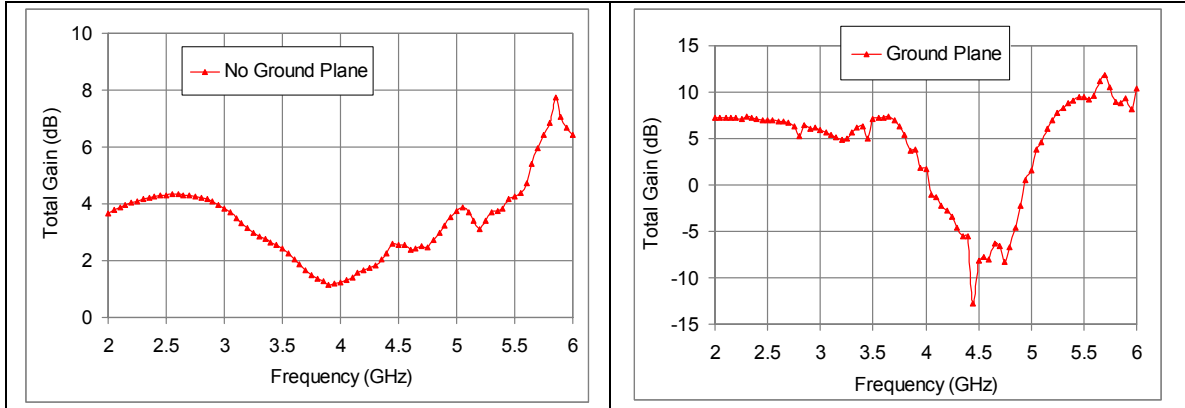


Figure 2.24 Simulated Total Gain (dB) Versus Frequency for the Archimedean Spiral Antenna with and without a Ground Plane. Left Plot- Antenna Backed by a  $\lambda/4$  Thick Substrate Simulated at  $\Phi = 0^\circ$  and  $\Theta = 180^\circ$ . Right Plot- Antenna Backed by a  $\lambda/4$  Thick Substrate and a Ground Plane Simulated at  $\Phi = 0^\circ$  and  $\Theta = 0^\circ$

Figure 2.25 shows the simulated axial ratio (dB) versus frequency at the  $\Theta$  and  $\Phi$  angle positions where total gain is maximum for the Archimedean spiral antenna backed by a  $\lambda/4$  thick substrate. The Archimedean spiral antenna achieves circular polarization through a wider frequency range than the equiangular spiral antenna without a ground plane present. For instance, the Archimedean spiral antenna has circular polarization from 2.4 to 6.0 GHz except for the frequency range between 5.75 to 5.9 GHz where the polarization is more linear. Moreover, it also has linear polarization from 2.0 to 2.39 GHz. On the contrary, the equiangular spiral antenna has circular polarization from 3.5 to 4.5 GHz. Below 3.5 GHz, the polarization is linear. The linear polarization at lower frequencies can be attributed to the reflections from the end of each spiral arm [6]. The reflected waves have opposite sense polarization than the outward traveling waves, which has a significant impact on the axial ratio at the lower cutoff frequencies. The reflections

from the end of each equiangular spiral arm might be greater than from the end of each Archimedean spiral arm since the equiangular spiral arms are wider at the point of truncation resulting in linear polarization through a wider low frequency range.

Furthermore, the Archimedean and equiangular spiral antennas achieve linear polarization through a wider frequency range when backed by a  $\lambda/4$  thick substrate and a ground plane than without a ground plane present. For instance, the Archimedean spiral antenna has mostly linear polarization from 2 to 6.0 GHz except for the frequency ranges from 5.05 to 5.45 GHz, from 5.65 to 5.8 GHz, and at 4.95 GHz where it has circular polarization. In this case, the reflections from the end of each spiral arm plus the interference caused when the surface waves traveling along the ground plane reach the substrate edges are the key factors accountable for the linear polarization through a wider frequency range.

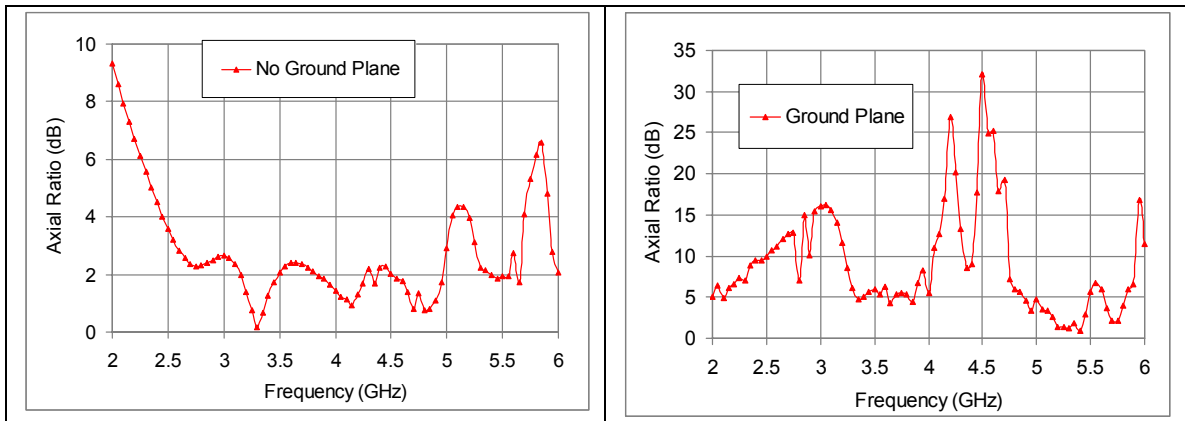


Figure 2.25 Simulated Axial Ratio (dB) Versus Frequency for the Archimedean Spiral Antenna with and without a Ground Plane. Left Plot- Antenna Backed by a  $\lambda/4$  Thick Substrate Simulated at  $\Phi = 0^\circ$  and  $\Theta = 180^\circ$ . Right Plot- Antenna Backed by a  $\lambda/4$  Thick Substrate and a Ground Plane Simulated at  $\Phi = 0^\circ$  and  $\Theta = 0^\circ$

## 2.6 Summary and Conclusions

Two types of frequency independent antennas were designed and simulated as two-arm spirals. Simulations have been performed with a ground plane located

approximately a quarter-wavelength from the antenna, and without a ground plane. The non-ground plane configuration is the reference configuration as it is the goal to obtain similar results to this when we miniaturize the most optimal design using a high impedance frequency selective surface (FSS). The FSS layer will be static (not tuned) and thus the overall bandwidth will reduce relative to the non-ground plane approach.

The simulation results show that even though the Archimedean and the equiangular spiral antennas have different equations defining them, their performance characteristics are similar. For instance, the return loss, VSWR, total gain, and radiation characteristics follow similar and expected trends. Despite the fact that the simulations were performed using a substrate with a fixed electrical length of  $\lambda/4$  at 2.4 GHz, both spirals showed a broadband response at the frequency range of interest. Also, as it was expected, the presence of a ground plane a distance equal to a quarter wavelength away from the antenna resulted in similar radiation responses for both spiral antennas.

To conclude, the Archimedean spiral has a more flat input impedance response, as well as circular polarization over a greater bandwidth than the equiangular spiral. In addition, since the difference in physical size between both spirals is not significant, the Archimedean spiral appears to be the most optimal design to be miniaturized in the z-direction using an FSS. In Chapter 3, the construction and testing of the Archimedean spiral antenna using a narrowband Balun is presented in order to validate the performance of the antenna at a chosen frequency of 2.4GHz.

## Chapter 3

### Archimedean Spiral Antenna with a Narrow-Band Feed Network

#### 3.1 Introduction

In Chapter 2, the Archimedean spiral antenna was found to be the optimum frequency independent design to be constructed and integrated with a narrow-band feed network due to its radiation characteristics. In order to fabricate the spiral antenna, it was necessary to use a thinner substrate than a  $\lambda/4$  thick substrate at a chosen common wireless communication frequency of 2.4 GHz because the physical thickness of about 24.7 mm is not commercially available. Throughout this chapter, electromagnetic and circuit level simulations were performed to investigate the effect on the antenna radiation performance when decreasing the substrate thickness to 31 mils (0.8 mm).

The Archimedean spiral antenna was simulated using a different feed network than the ideal excitation at the antenna feed point used in Chapter 2. In order to feed the two-arm spiral antenna with a narrow-band feed network, it was necessary to access the antenna feed point with vias that go to the end of the substrate and twin-strip lines to connect the balanced antenna input to the feed network as shown in figure 3.1. Simulations of the antenna with feeding wires and twin-strip lines were performed using HFSS.

The narrow-band feed network consists of a Balun, which connects a balanced transmission line to an unbalanced transmission line [3]. The unbalanced transmission

line serves as the interface between the antenna and an RF coaxial connector. The Balun was designed and simulated using the Agilent Advanced Design System (ADS) software. Furthermore, it was measured integrated with the spiral antenna as well as in a back-to-back configuration. Finally, the RF coaxial connector was also simulated in HFSS in a two-port back-to-back configuration so as to investigate the performance of this 50-ohm unbalanced connection.

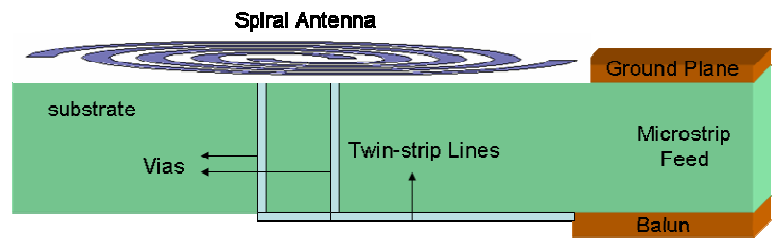


Figure 3.1 Spiral Antenna Integrated with a Narrow-band Feed Network

### 3.2 Archimedean Spiral Antenna Design

The spiral antenna simulated in Chapter 2 used a substrate with a  $\lambda/4$  thickness calculated at 2.4GHz. Nevertheless, this thickness translates into a physical dimension not available for commercial dielectric substrates such as Rogers. Therefore, new simulations were conducted with a 31 mil thick Rogers substrate, so that as to predict the antenna behavior on the substrate used for fabrication.

Similarly, the spiral antenna simulations performed in Chapter 2 used a lumped port excitation at the antenna feed point. However, to maintain the symmetrical properties of the antenna, it is necessary to feed the antenna with an electrically and geometrically balanced line [5]. In addition, this balanced line can be connected to an unbalanced line using a Balun to be able to measure the antenna using a coaxial cable.

The designed transition between the antenna feed point and the Balun consists of two wires that go from the feed point of the spiral antenna down to the bottom of the substrate through via holes and two planar twin-strip lines that go from the feeding wires at the bottom of the substrate to one side of the substrate, as shown in figure 3.1. Microwave simulations in ADS were performed to examine the effect of adding a balanced feed line structure on the antenna performance.

### 3.2.1 Electromagnetic Simulations of the Spiral Antenna on a Thinner Substrate

The new substrate backing the spiral antenna was a 31-mil thick dielectric sheet manufacture by Rogers. This substrate was chosen because of its low dielectric constant and low-loss tangent. The spiral operates as a transmission line between the arms whose length becomes significant for tightly wrapped spirals [3]. This transmission could be analyzed as a coplanar strip transmission line for losses, and the equivalent dielectric constant of the transmission line loads the spirals and reduces the effective loop radiator size [3].

The spiral antenna simulations on a thinner substrate presented in this section use the same lumped port excitation feed structure used in Chapter 2, as well as the same radiation boundary assignment except for shorter dimensions in the z-direction due to the thinner substrate thickness, as shown in figure 3.2. Simulation results will corroborate expected changes in antenna performance as far as the return loss, VSWR, and input impedance. The antenna radiation pattern is expected to still follow the well-known spiral antenna behavior.

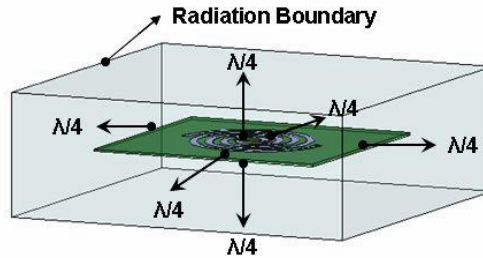


Figure 3.2 Radiation Boundary Assignment for the Archimedean Spiral Antenna on a 31-mil Thick Substrate

### 3.2.1.1 S-parameter Simulations

Figure 3.3 shows  $S_{11}$  in dB and phase for the Archimedean spiral antenna with a  $\lambda/4$  and a 31-mil thick substrate without a ground plane present. The Archimedean spiral antenna has a return loss of less than 5dB for a frequency range from 2 to 6 GHz. The effect of backing the antenna with a thinner substrate is illustrated by the blue trace in both plots shown on figure 3.3. For instance, the highest resonance for the antenna backed by a  $\lambda/4$  thick substrate occurs at 2.4 GHz where  $S_{11}$  equals -7.9 dB. Conversely, the highest resonance for the antenna backed by a 31-mil thick substrate occurs at 2.9 GHz where  $S_{11}$  equals -7.13.

The response of the antenna backed by the 31-mil thick substrate looks like the response of the antenna backed by a  $\lambda/4$  thick substrate shifted by about 500 MHz. This shift in  $S_{11}$  over frequency is due to the fact that the 31-mil thick substrate has a lower effective dielectric constant than the  $\lambda/4$  thick substrate, which in turn increases the resonant frequency. Similarly, this predictable shift is also present in the input impedance and VSWR responses as shown by figure 3.4 and 3.5.

Figures 3.4 and 3.5 show the simulated input impedance and VSWR, respectively, for the Archimedean spiral antenna with a  $\lambda/4$  and a 31-mil thick substrate without a

ground plane present. Both antenna simulations follow a similar trend with a flat impedance response from 2 to 6 GHz and a VSWR referenced to 50 ohms less than 3.5.

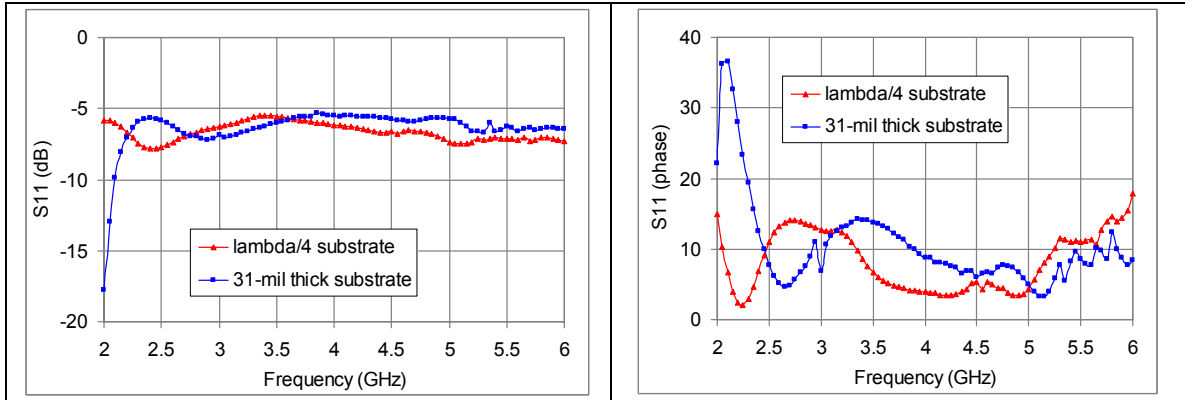


Figure 3.3 S-parameter Simulations for the Archimedean Spiral Antenna. Red Trace- Antenna Backed by a  $\lambda/4$  Thick Substrate. Blue Trace- Antenna Backed by a 31-mil Thick Substrate. Left Plot- Return Loss (dB). Right Plot- Return Loss (phase)

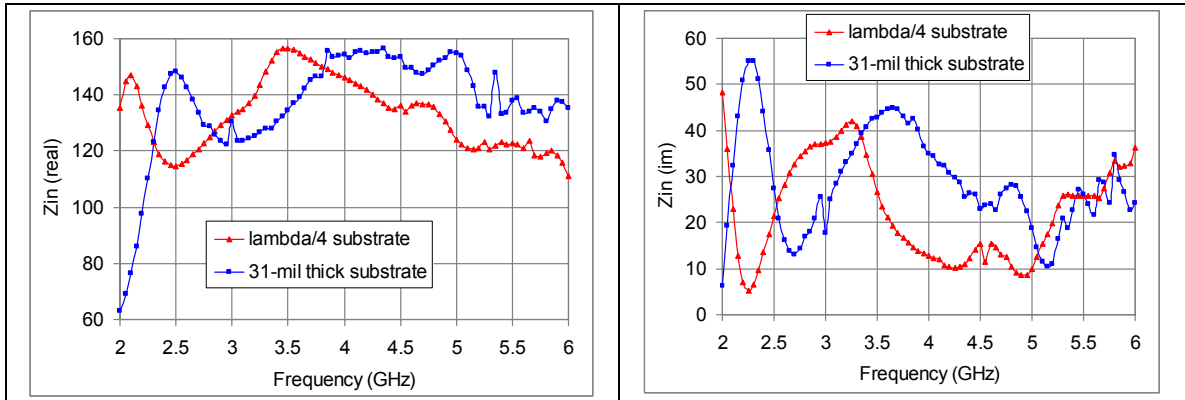


Figure 3.4 Input Impedance Simulations for the Archimedean Spiral Antenna. Red Trace- Antenna Backed by a  $\lambda/4$  Thick Substrate. Blue Trace- Antenna Backed by a 31-mil Thick Substrate. Left Plot- Input Impedance (real). Right Plot- Input Impedance (imaginary)

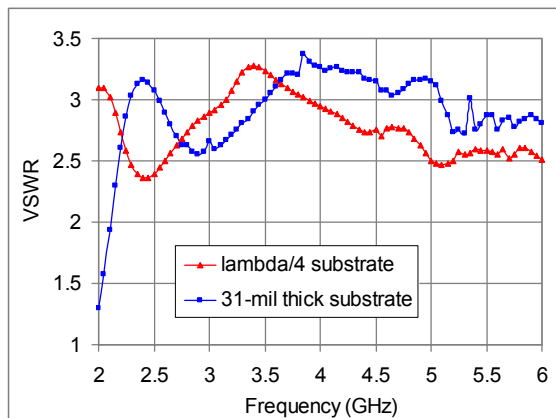


Figure 3.5 Simulated VSWR for the Archimedean Spiral Antenna. Red Trace- Antenna Backed by a  $\lambda/4$  Thick Substrate. Blue Trace- Antenna Backed by a 31-mil Thick Substrate

### 3.2.1.2 Radiation Pattern Simulations

Figure 3.6 shows the simulated far-field radiation patterns versus Theta at 2.4GHz for the Archimedean spiral antenna with a  $\lambda/4$  and a 31-mil thick substrate without a ground plane present. The Archimedean spiral antenna backed by a 31-mil thick substrate shows an expected total gain pattern characterized by two major circular lobes. The maximum total gain at 2.4GHz is 2.98dB and occurs at a Theta angle equal to  $180^\circ$  for  $0^\circ$  and  $90^\circ$  Phi angles. As expected, the maximum gain is lower for the antenna simulated on the thinner substrate, but it still occurs at the same Theta angle as the antenna with a  $\lambda/4$  thick substrate. The thicker substrate suppresses one of the major lobes into minor lobes, which eventually disappear when a ground plane is present as shown by the pattern simulations in Chapter 2. Figure 3.7 shows the side, front, and top views of the simulated radiation patterns in 3D at 2.4GHz for the Archimedean spiral antenna backed by a 31-mil thick substrate without a ground plane present.

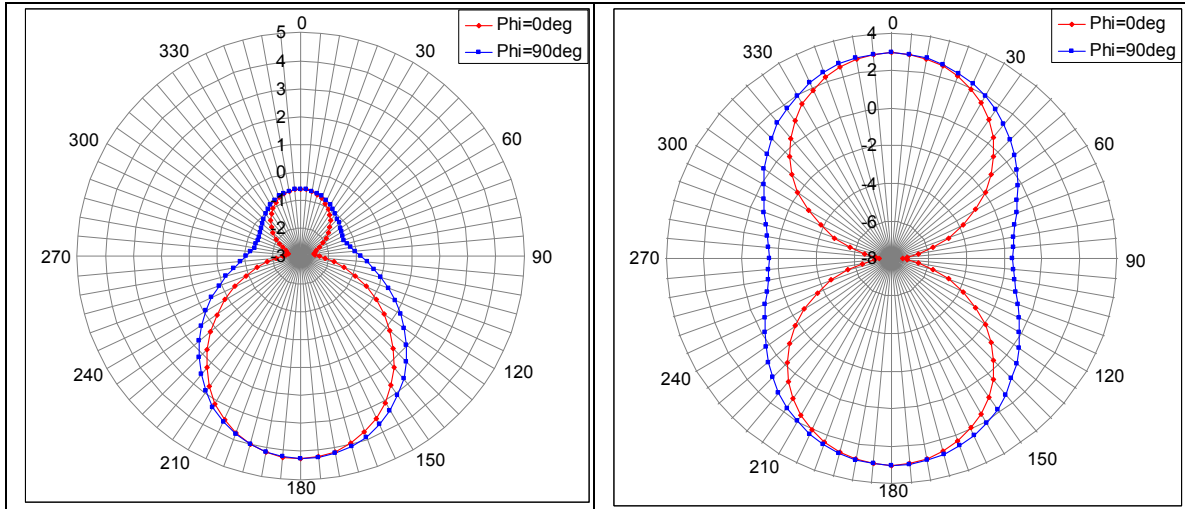


Figure 3.6 Simulated Radiation Pattern Versus Theta at 2.4GHz for the Archimedean Spiral Antenna. Red Trace- Phi = 0deg. Blue Trace- Phi = 90deg. Left Plot- Antenna Backed by a  $\lambda/4$  Thick Substrate. Right Plot- Antenna Backed by a 31-mil Thick Substrate

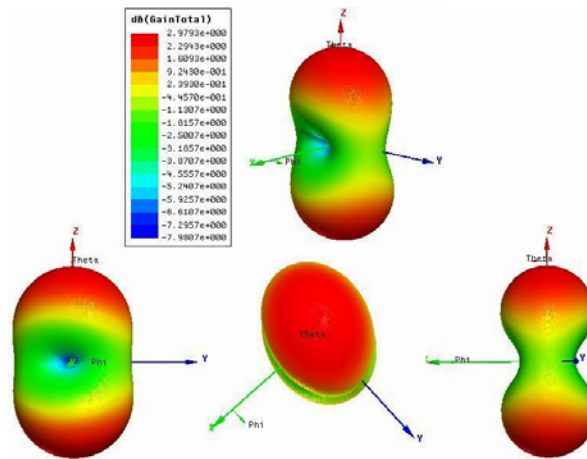


Figure 3.7 Side, Front, and Top Views of Simulated Radiation Pattern in 3D at 2.4GHz for the Archimedean Spiral Antenna Backed by a 31-mil Thick Substrate

### 3.2.1.3 Antenna Parameter Simulations

Figure 3.8 shows the simulated total maximum gain (dB) versus frequency for the Archimedean spiral antenna. The spiral antenna backed by a 31-mil thick substrate and without a ground plane present shows a total maximum gain increasing with frequency as expected. The gain increases from 2 to ~10 dB between 2 to 5.4 GHz. From 2 to 3GHz, the total maximum gain is lower than the gain obtained with the antenna backed by a  $\lambda/4$

thick substrate. However, from 3 to 5.4GHz, the total maximum gain is higher than the gain obtained with the antenna backed by a  $\lambda/4$  thick substrate.

Figure 3.9 shows the simulated axial ratio (dB) versus frequency at the Theta and Phi angle position where total gain is maximum for the Archimedean spiral antenna. The spiral antenna backed by a 31-mil thick substrate and without a ground plane present has circular polarization from 3.15 to 5.9 GHz. On the contrary, from 2 to 3.1 GHz the polarization is more linear. Furthermore, from 2 to 3.5 GHz, the axial ratio is higher than the axial ratio obtained with the antenna backed by a  $\lambda/4$  thick substrate. However, from 3.6 to 6.0 GHz, the axial ratio follows a close trend to the axial ratio obtained with the antenna backed by a  $\lambda/4$  thick substrate.

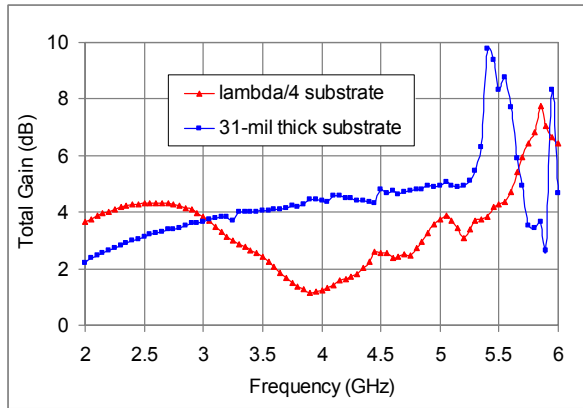


Figure 3.8 Simulated Total Gain (dB) Versus Frequency for the Archimedean Spiral Antenna. Red Trace - Antenna Backed by a  $\lambda/4$  Thick Substrate Simulated at Phi =  $0^\circ$  and Theta =  $180^\circ$ . Blue Trace- Antenna Backed by a 31-mil Thick Substrate Simulated at Phi =  $0^\circ$  and Theta =  $180^\circ$

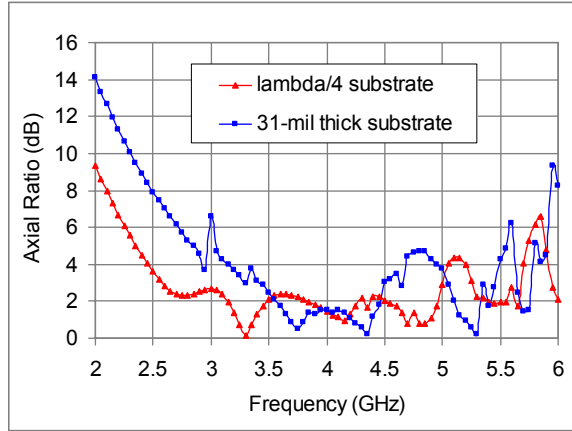


Figure 3.9 Simulated Axial Ratio (dB) Versus Frequency for the Archimedean Spiral Antenna. Red Trace- Antenna Backed by a  $\lambda/4$  Thick Substrate Simulated at  $\Phi = 0^\circ$  and  $\Theta = 180^\circ$ . Blue Trace- Antenna Backed by a 31-mil Thick Substrate Simulated at  $\Phi = 0^\circ$  and  $\Theta = 180^\circ$

### 3.2.2 Electromagnetic Simulations of the Effect of Adding a Narrow-Band Feed Structure to the Spiral Antenna

The effect of adding a narrow-band feed network to the spiral antenna was analyzed in HFSS in two stages. The first stage consists of feeding the antenna using two wires that go from the feed point of the spiral antenna down to the bottom of the substrate (31 mils away from the antenna) through via holes. Figure 3.10 illustrates this first feeding used that it is referred to as “bottom feeding.” The second stage consists of feeding the antenna using two planar twin-strip lines that go from the feeding wires at the bottom of the substrate over to one side of the substrate. Eventually, a Balun will be connected to these lines with the purpose of fabricating and testing the spiral antenna. Figure 3.11 illustrates this second feeding used that it is referred to as “side feeding.”

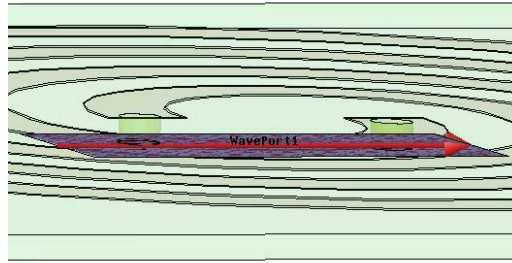


Figure 3.10 Wave Port Assignment at the Bottom of the 31-mil Thick Substrate for the Archimedean Spiral Antenna with Feeding Wires

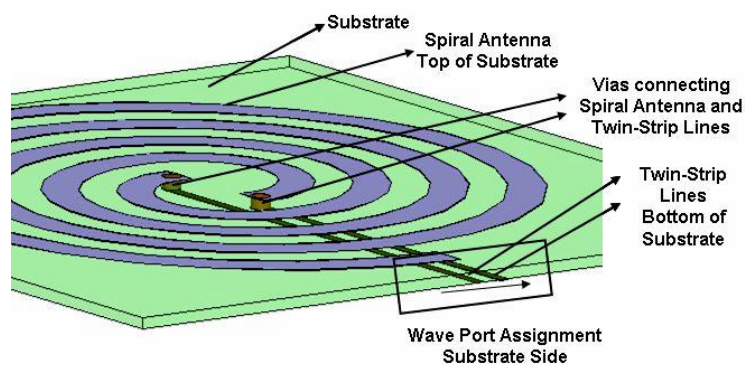


Figure 3.11 Wave Port Assignment to One Side of the 31-mil Thick Substrate for the Archimedean Spiral Antenna with Feeding Twin-Strip Lines

These simulations were performed using a wave port assignment instead of a lumped port because it calculates additional information regarding the port-cross section, such as characteristic impedance and complex propagation constant, that will be later needed for the microwave simulations in ADS. Wave ports are external excitations assumed to be connected to a semi-infinitely long waveguide that has the same cross-section and material properties as the port [7]. The field patterns of the traveling waves entering and exiting the port are computed at every frequency point of interest using Maxwell's equations [7].

The generalized s-parameters calculated by HFSS must be renormalized to a constant characteristic impedance such as 50 ohms in order to match the results obtained in laboratory measurements and circuit simulators, which use a constant reference impedance so the ports are not perfectly matched at every frequency.

The wave ports must be calibrated in order to determine direction and polarity of fields, to make voltage calculations, and to be able to duplicate the results of laboratory measurements in which the setup is calibrated by removing the structure and connecting two ports together [7]. They are calibrated using integration lines, which serve as the path over which HFSS integrates the E-field to obtain the voltage at a wave port [7]. In [7], the procedure used by HFSS to calibrate the ports is explained in more detail.

The simulations used the same radiation boundary assignment used in previous simulations, except for shorter dimensions in the z and x directions for the bottom and side feeding respectively, since the wave port can not be inside the radiation boundary but on the interface instead. Figures 3.12 and 3.13 show the radiation boundary assignment for the spiral antenna with a bottom and a side feeding configuration respectively.

The radius of the wires feeding the antenna was defined as one quarter the desired strip width, since it represents an appropriate transformation from strip width to wire diameter [6]. The strip width of the Archimedean spiral antenna is equal to 2.653 mm, so the wire radius is equal to 0.663 mm. The twin strip lines feeding the antenna had a characteristic impedance of 215.96 ohms and were 33.979 and 26.021 mm long, 0.663 mm wide, and with a gap width equal to 1.326 mm.

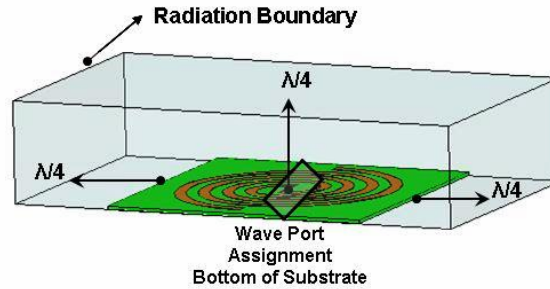


Figure 3.12 Radiation Boundary Assignment for the Archimedean Spiral Antenna with Feeding Wires and a 31-mil Thick Substrate

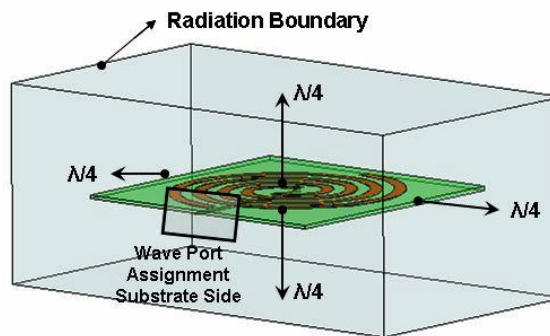


Figure 3.13 Radiation Boundary Assignment for the Archimedean Spiral Antenna with Feeding Twin-Strip Lines and a 31-mil Thick Substrate

### 3.2.2.1 S-parameter Simulations

Figure 3.14 compares the return loss in dB and phase of the Archimedean spiral antenna backed by a 31-mil thick substrate with three different types of feeding configurations. The effect of feeding the antenna with wires is illustrated by the blue trace in both plots shown on figure 3.14. For instance, from 2 to 5 GHz, the return loss of the antenna is less than 5 dB with feeding wires. On the other hand, the return loss of the antenna with feeding twin-strip lines is greater than 5 dB from 2.2 to 3.1GHz and from 5 to 6GHz as shown by the magenta trace in both plots of figure 3.14. The differences between the three simulations are expected as a result of adding transmission line with a characteristic impedance that is not matched to the load impedance. At the frequency

ranges where  $S_{11}$  is low for the antenna simulated with feeding wires and with twin-strip lines, the real part of the input impedance, shown in figure 3.15, is much greater than the respective characteristic impedance of the feeding wires (247.2 ohms) and twin-strip lines (215.96 ohms) resulting in a greater mismatch.

Figure 3.15 compares the simulated input impedance for the Archimedean spiral antenna backed by a 31-mil thick substrate with three different types of feeding configurations. The antenna with feeding wires has a peak on the impedance from 2 to 4GHz, and then it has a flat trace characterized by a lower impedance as compared to the antenna simulated directly at the spiral feed point. Similarly, the antenna with feeding twin-strip lines has a peak on the input impedance from 3.6 to 4.2 GHz, and then it has a flat trace characterized by a higher impedance as compared to the antenna simulated directly at the spiral feed point. Changes in input impedance were expected after adding feeding wires and twin-strip lines to the antenna, since we are adding extra transmission lines.

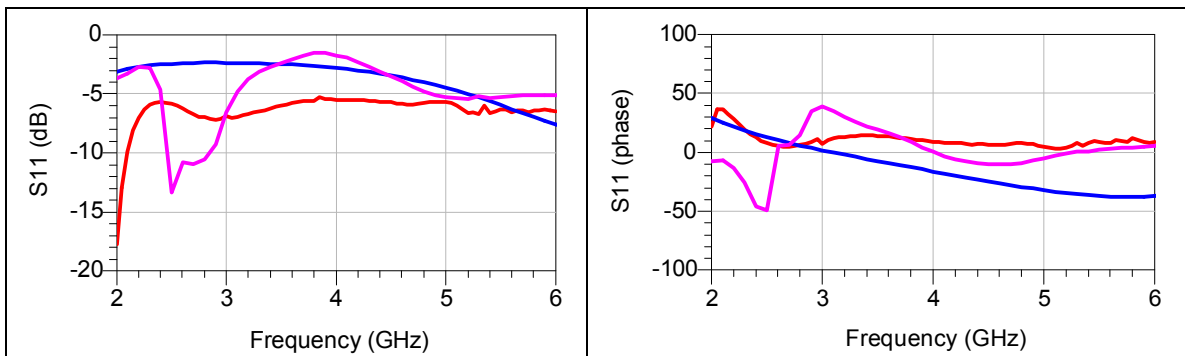


Figure 3.14 S-parameter Simulations for the Archimedean Spiral Antenna Backed by a 31-mil Thick Substrate. Red Trace- Antenna Simulated at the Antenna Feed Point. Blue Trace- Antenna Simulated with Feeding Wires. Magenta Trace – Antenna Simulated with Feeding Twin-Strip Lines Left Plot- Return Loss (dB). Right Plot- Return Loss (phase)

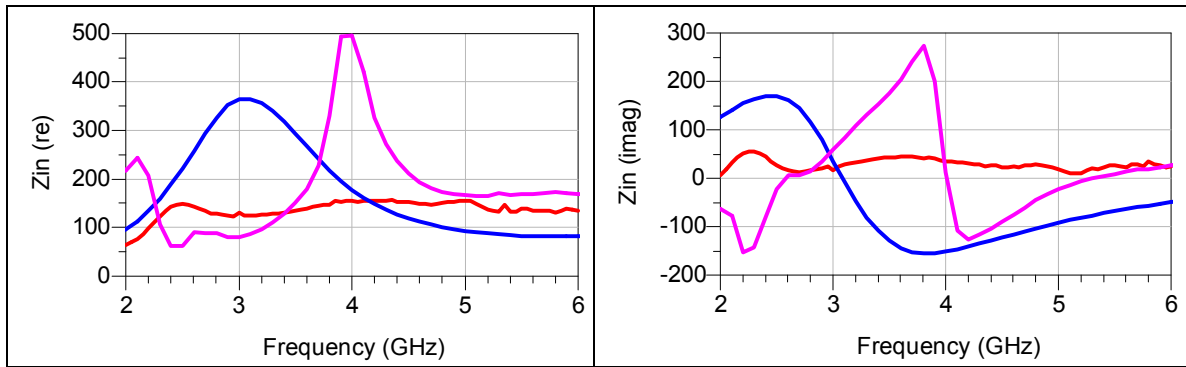


Figure 3.15 Input Impedance Simulations for the Archimedean Spiral Antenna Backed by a 31-mil Thick Substrate. Red Trace- Antenna Simulated at the Antenna Feed Point. Blue Trace- Antenna Simulated with Feeding Wires. Magenta Trace – Antenna Simulated with Feeding Twin-Strip Lines. Left Plot- Input Impedance (real). Right Plot- Input Impedance (imaginary)

### 3.2.2.2 Radiation Pattern Simulations

Figure 3.16 shows the simulated total far-field radiation patterns versus Theta at 2.4GHz for the Archimedean spiral antenna backed by a 31-mil thick substrate with two different types of feeding configurations. Both antenna feeding configurations (wires and twin-strip lines) show the expected total gain pattern characterized by two major circular lobes. However, the antenna with feeding wires shows a much lower gain versus Theta at both  $0^\circ$  and  $90^\circ$  Phi angles as compared to the antenna with feeding twin-strip lines. For instance, the maximum total gain at 2.4GHz for the antenna simulated with feeding wires is -5.09 dB and occurs at a Theta angle equal to  $0^\circ$  for both  $0^\circ$  and  $90^\circ$  Phi angles. The maximum total gain at 2.4GHz for the antenna simulated with feeding twin-strip lines is 2.6 dB and occurs at a Theta angle equal to  $30^\circ$  and at a Phi angle equal to  $0^\circ$ . Figures 3.17 and 3.18 show the side, front, and top views of the simulated radiation patterns in 3D at 2.4GHz for the Archimedean spiral antenna backed by a 31-mil thick substrate with feeding wires and twin-strip lines respectively.

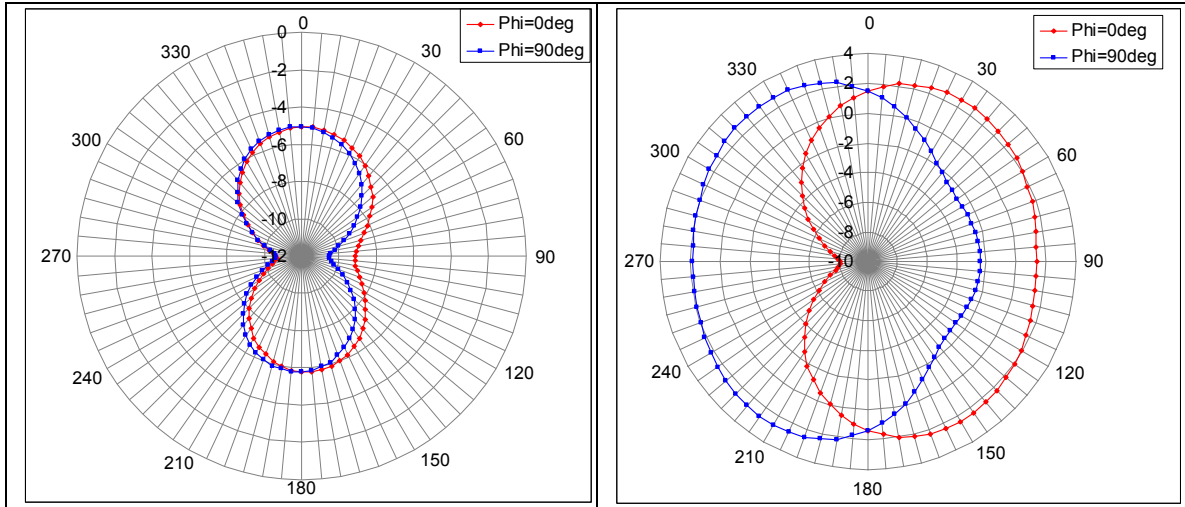


Figure 3.16 Simulated Radiation Pattern Versus Theta at 2.4GHz for the Archimedean Spiral Antenna Backed by a 31-mil Thick Substrate. Red Trace- Phi = 0deg. Blue Trace- Phi = 90deg. Left Plot- Antenna Simulated with Feeding Wires. Right Plot – Antenna Simulated with Feeding Twin-Strip Lines

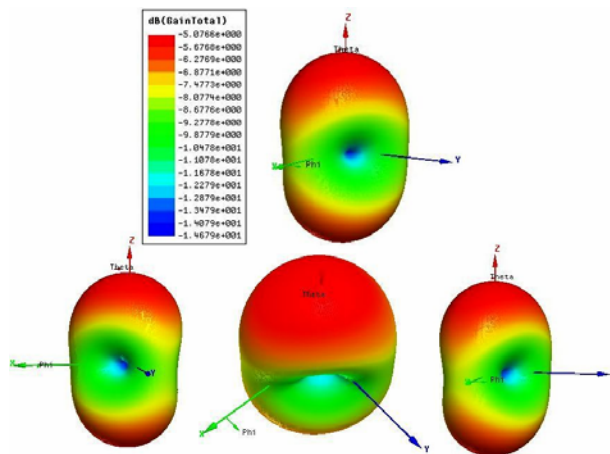


Figure 3.17 Side, Front, and Top Views of Simulated Radiation Pattern in 3D at 2.4GHz for the Archimedean Spiral Antenna Backed by a 31-mil Thick Substrate and Simulated with Feeding Wires

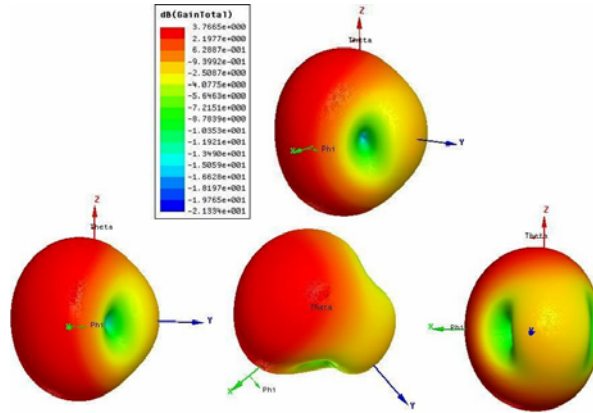


Figure 3.18 Side, Front, and Top Views of Simulated Radiation Pattern in 3D at 2.4GHz for the Archimedean Spiral Antenna Backed by a 31-mil Thick Substrate and Simulated with Feeding Twin-Strip Lines

### 3.2.2.3 Antenna Parameter Simulations

Figure 3.19 shows the simulated total maximum gain (dB) versus frequency for the Archimedean spiral antenna backed by a 31-mil thick substrate with two different types of feeding configurations. Both antenna feeding configurations (wires and twin-strip lines) show a total maximum gain increasing with frequency as expected. However, the antenna with feeding wires (blue trace on figure 3.19) has considerably lower gain than the antenna simulated directly at the spiral feed point (red trace on figure 3.19). On the contrary, the gain of the antenna with feeding twin-strip lines (green trace on figure 3.19) follows a closer trend to the gain of the antenna simulated directly at the spiral feed point except for the frequency range from 2.45 to 3GHz. The peak gain variation at lower frequencies can be attributed to the reflections from the end of each spiral arm.

Based on return loss and maximum gain results, it is better to feed the antenna with wires and twin-strip lines than just with wires in order to obtain an  $S_{11}$  greater than 5 dB and a gain response closer to the one achieved by the antenna fed directly at the spiral feed point.

Figure 3.20 shows the simulated axial ratio (dB) versus frequency for the Archimedean spiral antenna backed by a 31-mil thick substrate with two different types of feeding configurations. The spiral antenna with feeding wires has circular polarization from 2 to 4.5 GHz. On the contrary, the antenna with feeding twin-strip lines has linear polarization for almost the entire frequency range except for some narrow frequency ranges.

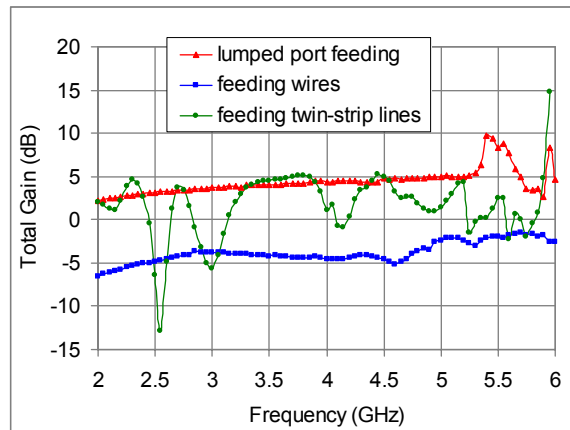


Figure 3.19 Simulated Total Gain (dB) Versus Frequency for the Archimedean Spiral Antenna Backed by a 31-mil Thick Substrate. Red Trace - Antenna Simulated at the Antenna Feed Point at  $\Phi = 0^\circ$  and  $\Theta = 180^\circ$ . Blue Trace- Antenna Simulated with Feeding Wires at  $\Phi = 0^\circ$  and  $\Theta = 0^\circ$ . Green Trace – Antenna Simulated with Feeding Twin-Strip Lines at  $\Phi = 0^\circ$  and  $\Theta = 30^\circ$

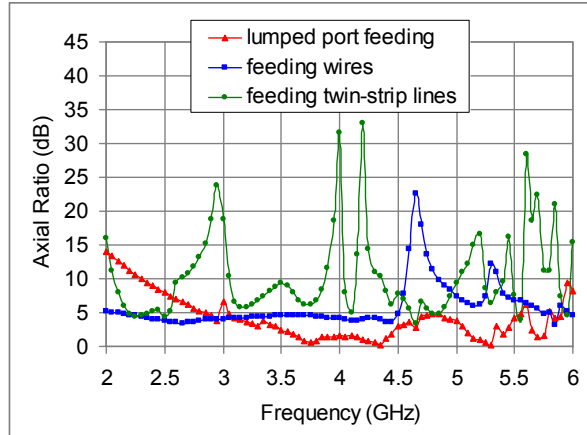


Figure 3.20 Simulated Axial Ratio (dB) Versus Frequency for the Archimedean Spiral Antenna Backed by a 31-mil Thick Substrate. Red Trace - Antenna Simulated at the Antenna Feed Point at  $\Phi = 0^\circ$  and  $\Theta = 180^\circ$ . Blue Trace- Antenna Simulated with Feeding Wires at  $\Phi = 0^\circ$  and  $\Theta = 0^\circ$ . Green Trace – Antenna Simulated with Feeding Twin-Strip Lines at  $\Phi = 0^\circ$  and  $\Theta = 30^\circ$

### 3.2.3 Microwave Simulations of the Effect of Adding a Narrow-Band Feed Structure to the Spiral Antenna

The spiral antenna response obtained with the HFSS simulations was analyzed and approximated using ADS in order to corroborate that adding feeding wires and twin-strip lines to the antenna feed point does not influence the performance by the existence of coupling effects between the spiral arms and the feeding structure. The expected results will support the presumption that the narrow-band balanced feed line structure will have an effect on the antenna operation only because of the fact that further transmission line is present.

The first step was to approximate with circuit-level simulations the response of the antenna when feeding wires are added to the spiral antenna feed point. In order to approximate the antenna's return loss response in ADS, the physical transmission line parameters of the feeding wires were introduced into an ideal transmission line model, and the s-parameter response of the spiral antenna simulated at the feed point with a

lumped port assignment was added to this transmission line model. The schematic representation of this procedure is shown on figure 3.21.

In HFSS simulations, each port is assumed to be connected to a transmission line structure that has the same cross-section as the port [7]. Then, the complex propagation constant “ $\gamma$ ” and the characteristic impedance of this transmission line “ $Z_{pi}$ ” are computed by HFSS. The additional physical transmission line parameters of the feeding wires needed for the model in ADS are physical length “ $L$ ” equal to 0.8738 mm, effective dielectric constant “ $k$ ”, attenuation constant, dielectric loss tangent “ $TanD$ ” equal to 0.0009 for the Rogers material used in the simulations, and relative permeability “ $\mu$ ” equal to 1 for the Rogers material used in the simulations.

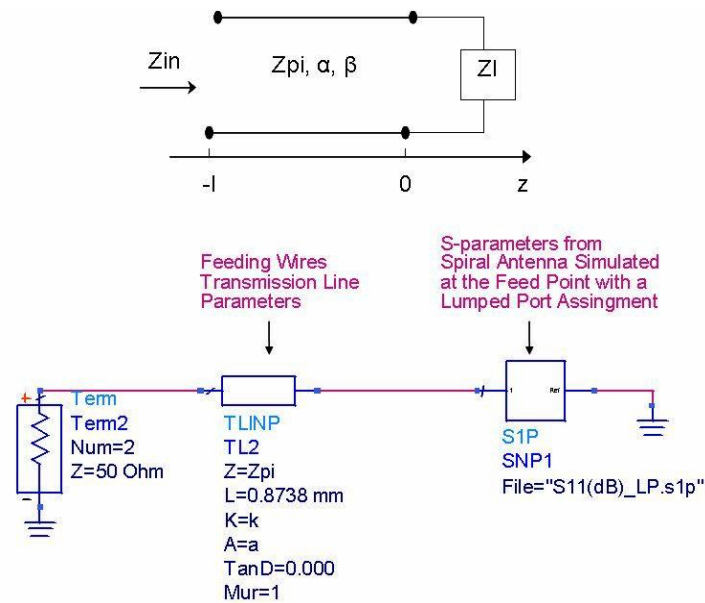


Figure 3.21 ADS Approximation of the Spiral Antenna Response when Simulated with Feeding Wires

The complex propagation constant “ $\gamma$ ” is given by equation 3.1, where  $\alpha$  (nepers/meter) is the attenuation constant of a signal in the transmission structure and  $\beta$  (radians/meter) is the phase constant associated with the wave [7]. Equation 3.2 converts the attenuation constant from nepers per meter to dB per meter.

$$\gamma = \alpha + j\beta \quad (3.1)$$

$$\alpha \left( \frac{\text{dB}}{\text{meter}} \right) = 20 \cdot \log(e^\alpha) \quad (3.2)$$

The effective dielectric constant “k” is given by equation 3.3, where  $k_0$  is the free space wave number, and  $\beta$  is the imaginary component of the complex propagation constant [9].

$$k = \left( \frac{\beta}{k_0} \right)^2 \quad (3.3)$$

$$k_0 = \frac{2 \cdot \pi \cdot f}{c} \quad (3.4)$$

Figure 3.22 shows the comparison between the spiral antenna simulated with feeding wires and the approximation to this response using transmission line simulations in ADS. The differences among the simulations in HFSS and the approximation in ADS can be explained by the fact that the simulations were obtained using two different types of excitations (wave and lumped port).

The second step was to approximate with circuit-level simulations the response of the spiral antenna when twin-strip lines are added from the feeding wires at the bottom of the substrate all the way to one side of the substrate. In order to approximate the antenna’s return loss response in ADS, the physical transmission line parameters of the twin-strip lines were introduced into an ideal transmission line model, and the s-parameter response of the spiral antenna simulated with two feeding wires was added to

this transmission line model. The schematic representation of this procedure is shown on figure 3.23.

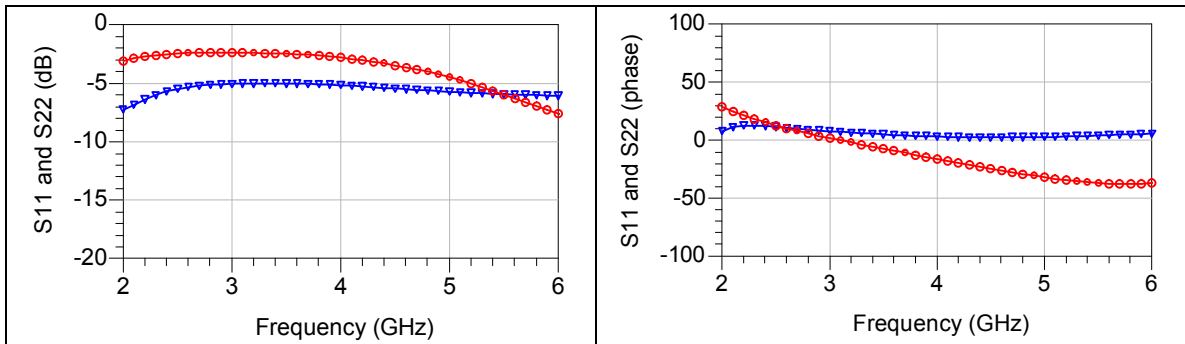


Figure 3.22 S-parameters Simulations of Spiral Antenna Feeding Wires. Red Trace-Spiral Antenna Simulated in HFSS with Two Feeding Wires. Blue Trace- Approximation Simulations in ADS of this Response. Left Plot- Return Loss (dB). Right Plot- Return Loss (phase)

Besides the complex propagation constant “ $\gamma$ ” and the characteristic impedance “ $Z_{pi}$ ” of the twin-strip transmission lines computed by HFSS, the additional physical transmission line parameters of the feeding twin-strip lines needed for the model in ADS are physical length “ $L$ ” equal to 33.979 mm, effective dielectric constant “ $k$ ” calculated using equation 3.3, attenuation constant calculated in dB per meter by equation 3.2, dielectric loss tangent “ $TanD$ ” equal to 0.0009 for the Rogers material used in the simulations, and relative permeability “ $Mu$ ” equal to 1 for the Rogers material used in the simulations.

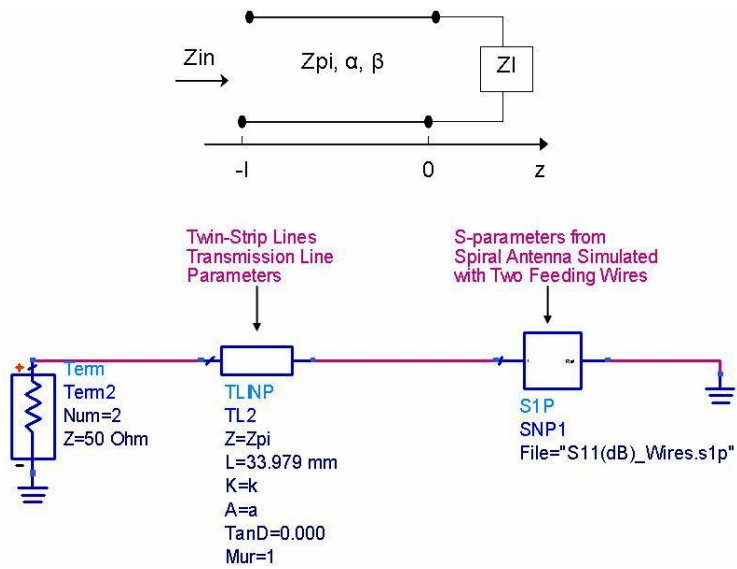


Figure 3.23 ADS Approximation of the Spiral Antenna Response when Simulated with Twin-Strip Lines

Figure 3.24 shows the comparison between the spiral antenna simulated with feeding twin-strip lines and the approximation to this response using transmission line simulations in ADS. The approximation follows the same trend as the HFSS simulation, and at 2.4, 3.5, and 4.8 GHz they are an exact match. These results confirm that adding feeding wires and twin-strip lines to the antenna feed point does not influence the performance by the existence of coupling effects between the spiral arms and the feeding structure. The microwave simulations in ADS support the presumption that the narrow-band balanced feed line structure has an effect on the antenna operation only because further transmission line is present.

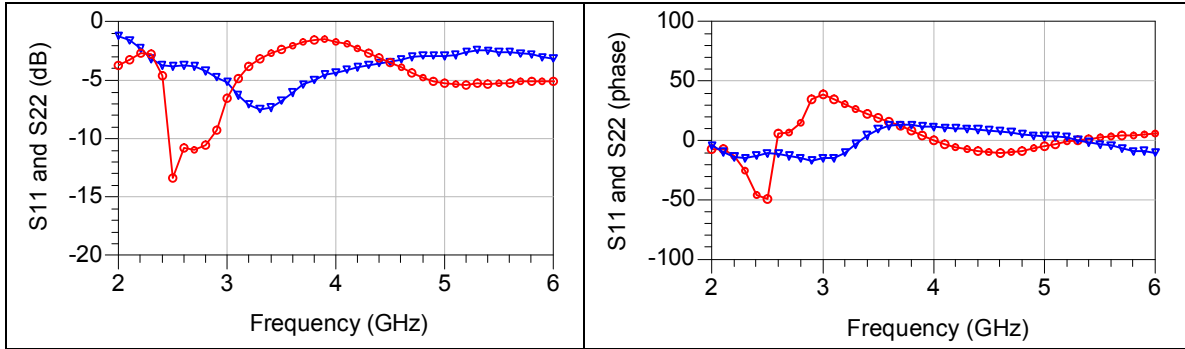


Figure 3.24 S-parameters Simulations of Spiral Antenna Feeding Twin-Strip Lines. Red Trace-Spiral Antenna Simulated in HFSS with Feeding Twin-Strip Lines. Blue Trace- Approximation Simulations in ADS of this Response. Left Plot- Return Loss (dB). Right Plot- Return Loss (phase)

### 3.3 Balun Design

In order to fabricate the antenna to corroborate the HFSS simulations at a frequency of 2.4 GHz, we designed a microstrip feed that consist of a matching network and a Balun. The purpose of the Balun is to provide a balanced feed to the antenna necessary for optimum performance as well as a transition to an unbalanced feed characteristic of a microstrip design. Prior to the microstrip feed design, antenna simulations using feeding wires and twin-strip lines were performed in HFSS to establish a suitable feeding configuration to connect the spiral antenna to the microstrip design.

In addition, the antenna simulations served to determine the input impedance looking into the antenna, which will be transformed to a purely real impedance using a matching network. Then, the impedance looking into the matching network will be transformed to 50 ohms by the Balun. This procedure is illustrated in figure 3.25.

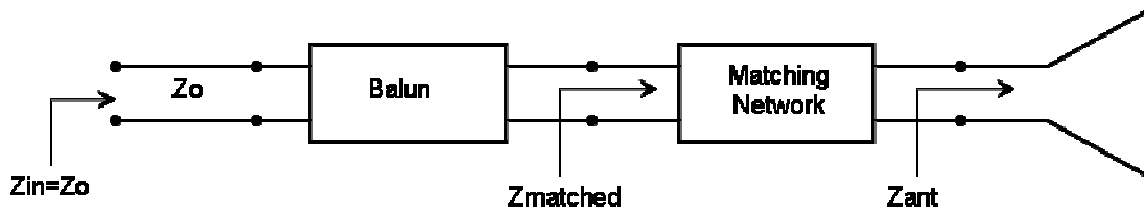


Figure 3.25 Integration of Spiral Antenna and Narrow-band Feed Network

The Balun was designed in two phases. The first phase was to design the Balun to appropriately connect the balanced antenna input to an unbalanced output. The second phase was to design the Balun as an impedance transformer to convert  $Z_{\text{matched}}$  to  $Z_o$  (50 ohms) as shown on figure 3.25. Moreover, a back-to-back configuration of the Balun was simulated in ADS and HFSS in order to investigate possible effects from stopping the ground plane of the microstrip narrow-band feed network at the input of the antenna.

### 3.3.1 Background Theory

The term Balun is a combination of the words balance and unbalanced. It is a device that connects a balanced two-conductor line to an unbalanced coaxial line [1]. A twin-lead transmission line (two parallel-conductor line) is a symmetrical line whereas a coaxial cable is inherently unbalanced [5]. A device such as a Balun can be used to balance inherently unbalanced systems by canceling or choking the net current flow to ground on the outside part of the outer conductor of the coax line [5].

The Balun operation can be explained by the balanced and unbalanced modes of the three-wire transmission lines. A balanced three-wire transmission-line mode carries equal and opposite currents in the feeder lines, where the capacitances per unit length of the two lines to ground are the same [3]. Coax is an example of an unbalanced line structure, where the inner conductor has no direct capacitance to ground [3].

Figure 3.26 shows circuit representations of the fundamental modes of a three-wire transmission line without showing the ground conductor. Equal loads terminate ports 3 and 4. The unbalanced mode (equal current directions) is associated with the even mode, which applies equal voltages on ports 1 and 2 and forms a magnetic wall between the conductors becoming a virtual open circuit [3]. On the contrary, the balanced mode

(equal and opposite currents) is associated with the odd mode, which applies equal and opposite voltages on port 1 and 2 and set up an electric wall between the conductors becoming a virtual short circuit [3].

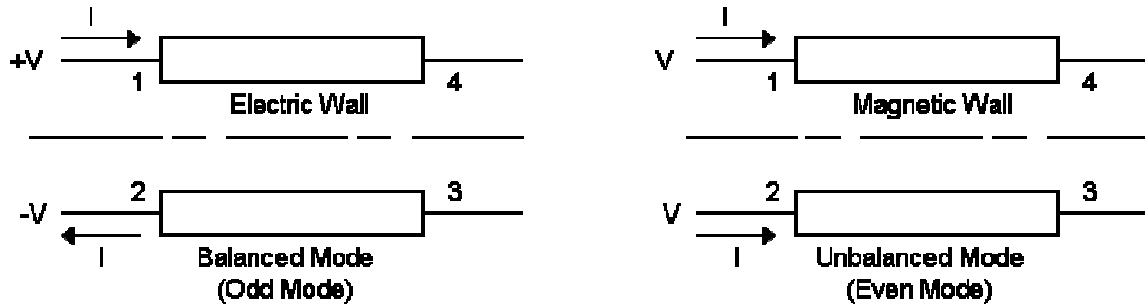


Figure 3.26 Balanced and Unbalanced Modes on a Three-Wire Transmission Line [3]

A balun also blocks the un-wanted far-field radiation components produced by the feeder line, whose polarizations redirect the beam peak of the antenna [3]. Only closely spaced equal and opposite currents, the balanced mode, cancel the far-field radiation from the currents on the feed lines [3].

### 3.3.2 Microwave Design and Simulations

It was desired to match the input impedance of the spiral antenna to a real value that would make the Balun easier to design. A matching network was used to eliminate the capacitive imaginary part of the input impedance looking into the antenna at 2.4 GHz. Figure 3.27 shows this input impedance.

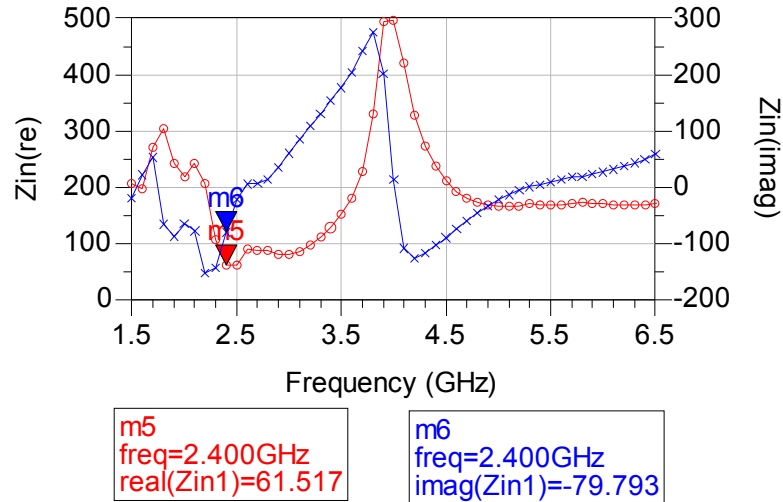


Figure 3.27 Input Impedance of the Spiral Antenna with Feeding Twin-Strip Lines. Red Trace- Zin (real). Blue Trace- Zin (imaginary)

A lumped-element matching network was chosen for its simplicity and ease to manufacture in order to match  $Z_{ant}$  equal to  $61.5-j79.8$  to  $Z_{matched}$  equal to 200 ohms. Figure 3.28 shows the network topology necessary to match this type of load since the normalized load impedance lies outside the  $1+jx$  circle on the smith chart. Equations 3.5 and 3.6 were used to calculate the series reactance  $X$  and shunt susceptance  $B$  for the marching network [9], where  $R_L$  is equal to 61.5 ohms,  $X_L$  is equal to  $-79.8$ , and  $Z_O$  is equal to 200 ohms. One of the possible solution networks was found based on these equations consisting of a 5.3pF series capacitor and an 8.8nH shunt inductor. The matching network was first simulated in ADS using ideal components as shown by figure 3.29.

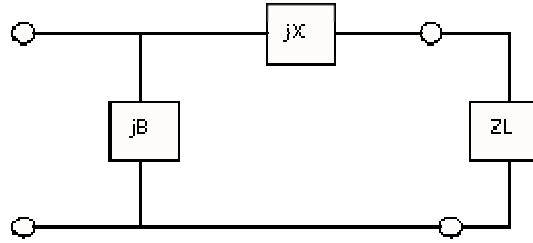


Figure 3.28 Matching Network Topology Needed to Match the Antenna Input Impedance to 200 Ohms

$$X = \sqrt{R_L \cdot (Z_0 - R_L)} - X_L \quad (3.5)$$

$$B = \frac{\sqrt{\frac{(Z_0 - R_L)}{R_L}}}{Z_0} \quad (3.6)$$

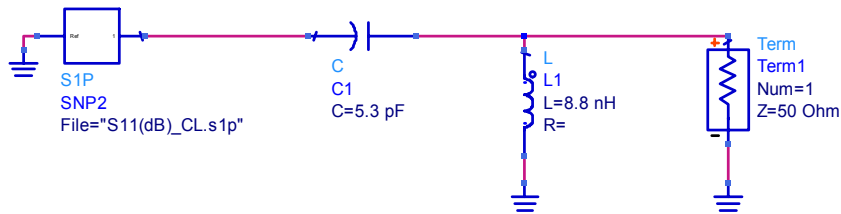


Figure 3.29 Ideal Lumped Element Matching Network Solution

The Johanson 0201 surface mount chip inductors and capacitors were chosen to fabricate the matching network. Therefore, the matching network was also analyzed by replacing the ideal lumped element components by the Modelithics ADS models of the Johanson 0201 surface mount chip inductors and capacitors in the ADS simulations. The lumped component values in the Johanson models were tuned to match the response of the matching network using ideal components as shown by figure 3.30. The final inductor and capacitor values were 2.6pF and 6.9nH respectively. Because of samples availability, the actual components used in the fabricated matching network were a 2.7pF capacitor and a 6.8nH inductor. Figure 3.31 compares the response of the matching networks using ideal components and Modelithics models.

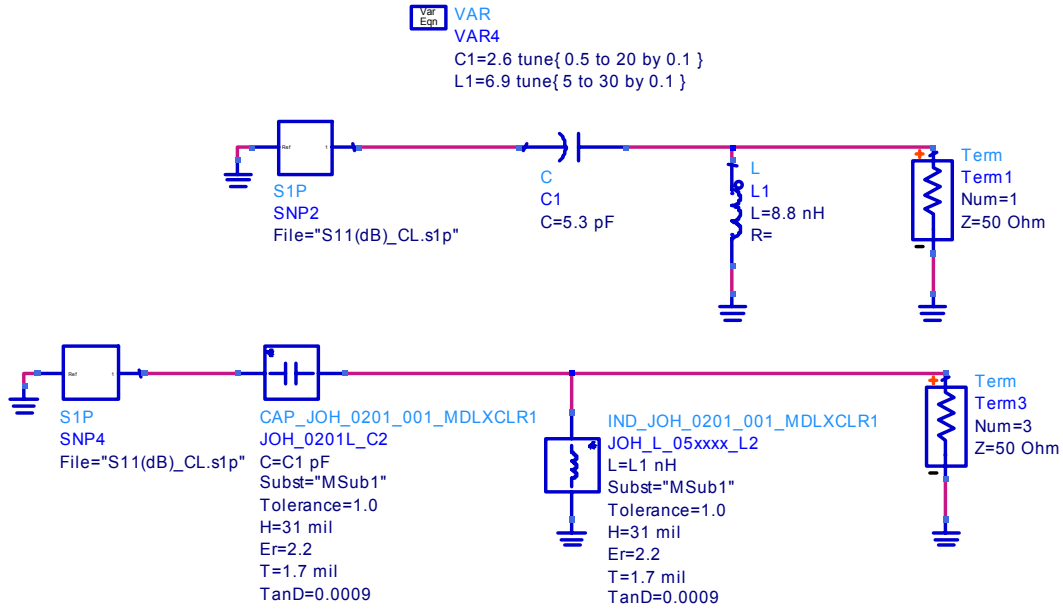


Figure 3.30 Ideal Versus Modelithics Johanson Models Matching Network Solution

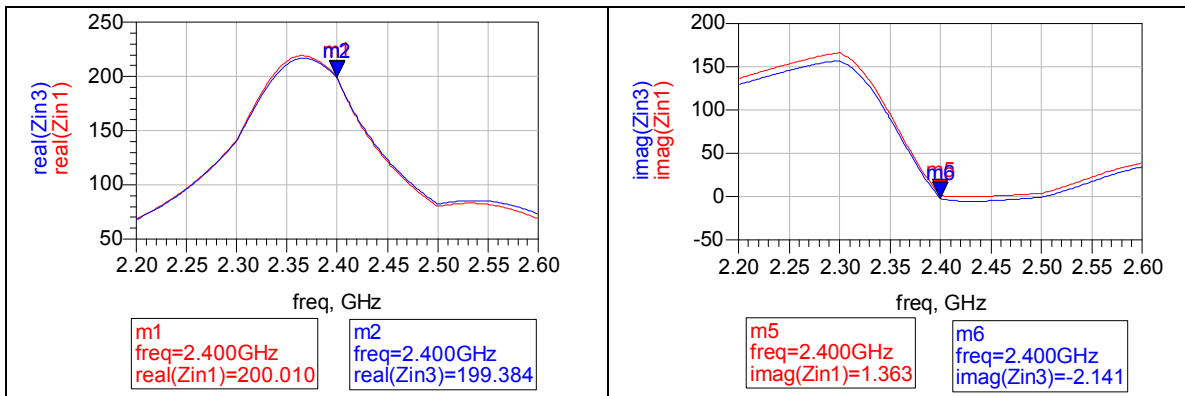


Figure 3.31 Ideal Versus Modelithics Johanson Models Matching Networks. Red Trace- Matching Network Using Ideal Components. Blue Trace- Matching Network Using Modelithics Models. Right Plot- Zin (real). Left Plot- Zin (imaginary)

### 3.3.2.1 Balanced Input to Unbalanced Output Transition Simulations

Figure 3.32 shows the Balun design that will connect the spiral antenna to a coaxial 50-ohm RF connector as shown by figure 3.40. This type of Balun was chosen among many available designs due to its planar geometry and impedance transformation capabilities that will provide a balanced to unbalanced feed reference to 50 ohms without

excessively increasing the design size in the Z-direction. In order to connect the balanced spiral antenna arms to an unbalanced line, the Balun balanced lines need to be a distance  $\lambda/4$  apart from each other.

Figure 3.33 shows the ADS simulation schematic used to optimize the lengths (L1 and L2) of the Balun, so that the phase difference between S12 and S13 is 180 degrees required for a balanced feed. The lengths L1 and L2 that provided a 180 degree phase difference between S12 and S13 were 22.5 and 23 mm respectively. Figure 3.34 shows the insertion loss (phase) after the optimization. The exact phase difference between S12 and S13 is 180.83 degrees at 2.4 GHz.

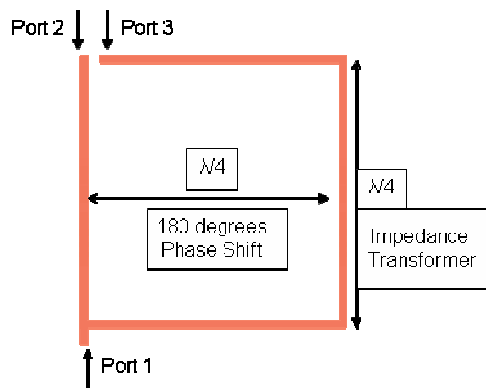


Figure 3.32 Balun Design

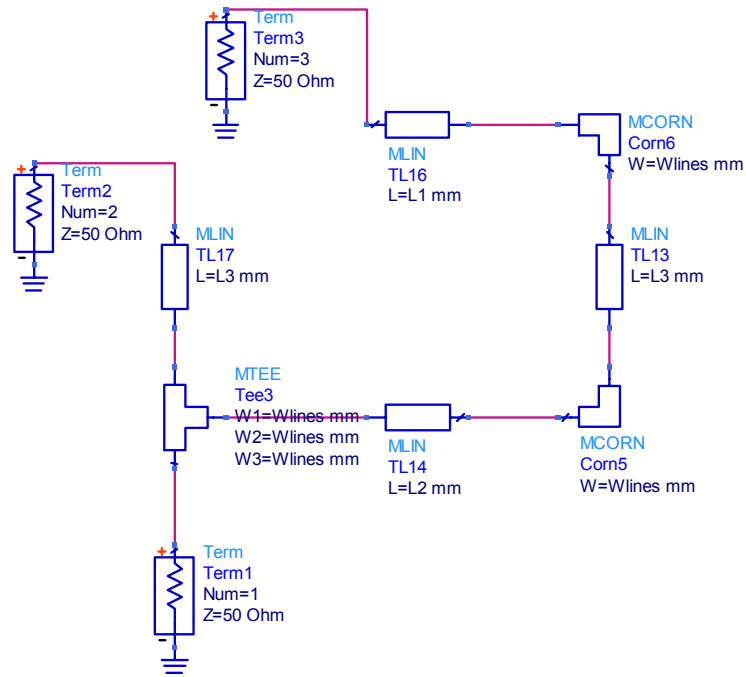


Figure 3.33 Balun Design Optimization in ADS to Connect a Balanced Input to an Unbalanced Output

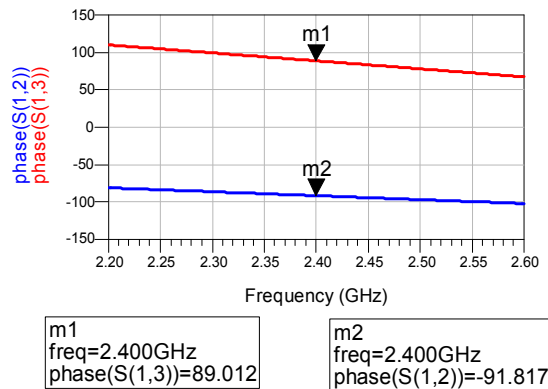


Figure 3.34 S12 (phase) of Balun Design. Red Trace- S13 (phase). Blue Trace- S12 (phase)

### 3.3.2.2 Impedance Transformation Simulations

In addition to providing a balanced feed to the self-complementary spiral antenna, the Balun design also includes a step change in impedance from 200 ohms (impedance looking into the matching network) to a 50-ohm transmission line. A 100 ohm resistor

was placed between ports 2 and 3 of the Balun on the ADS simulation to emulate the 200-ohm impedance seen looking into the matching network. In order to perform the impedance transformation, the transmission line length  $L3$  needs to be  $\lambda/4$ . Figure 3.35 shows the ADS simulation schematic used to optimize the length  $L3$  in order to transform the impedance from 200 to 50 ohms. Figure 3.36 shows the real and imaginary input impedance looking into the Balun after the length optimization. The final length  $L3$  that provided the impedance transformation was 23 mm. The width of the Balun transmission lines was optimized to 0.66 mm. The final input impedance looking into the narrow-band feed network and the spiral antenna is  $51.428 + j1.34$ .

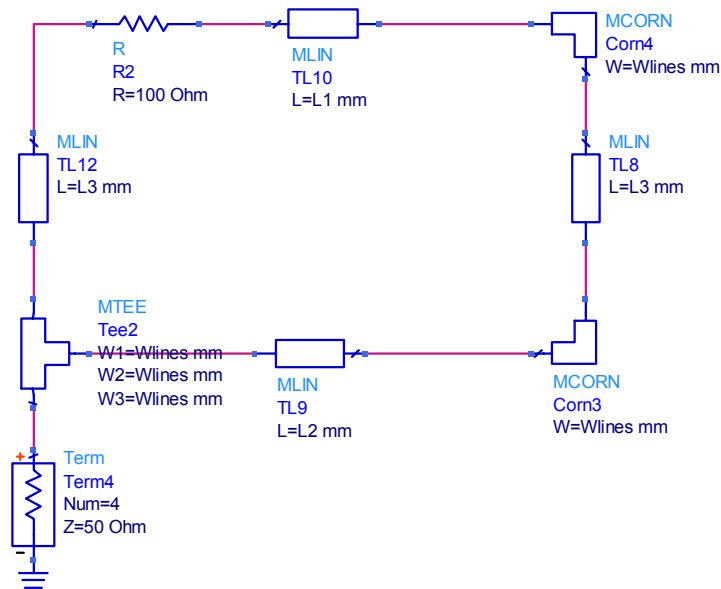


Figure 3.35 Impedance Transformation Design in ADS

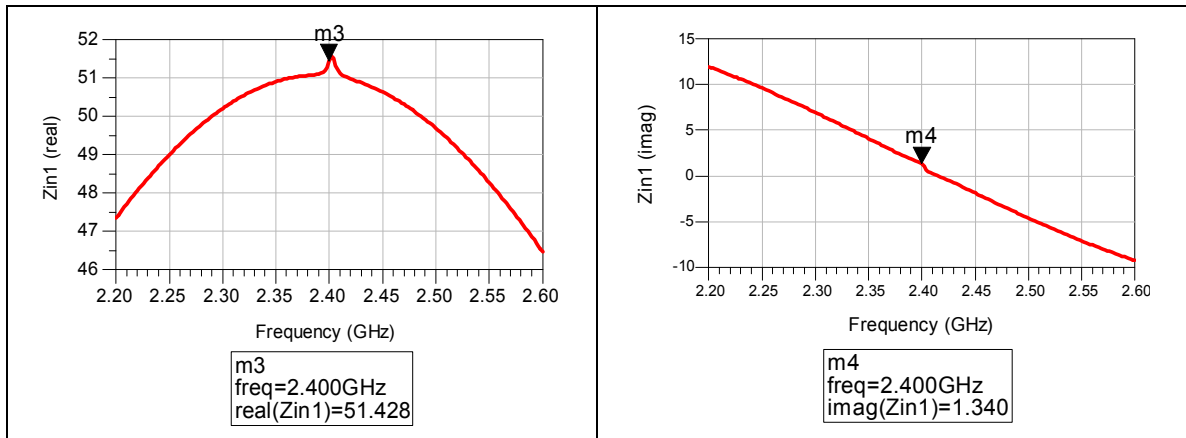


Figure 3.36 Balun Input Impedance. Left Plot- Zin (real). Right Plot- Zin (imaginary)

### 3.3.3 Ground Effects Microwave and Electromagnetic Simulations

Additional simulations were performed in order to investigate the effect of stopping the ground plane conductor at the balanced input of the Balun just where the balanced twin-strip lines connect. A back to back design was simulated in ADS and HFSS as shown by figure 3.37. This design consists of a Balun and its mirror image connected to each other through a twin-strip line. A short piece of twin-strip lines was used instead of the real twin-strip line connecting the antenna to the Balun so that the design would not become extremely long since we just wanted to check the ground effects. The design in HFSS was simulated using wave ports at both ports.

The short piece of twin-strip line was designed with a characteristic impedance of 200 ohms and to be approximately 20 degrees long at 2.4GHz. In order to calculate the physical length and width of the twin-strip line for the HFSS simulation, a coplanar waveguide structure was used to approximate a twin-strip line structure as shown by figure 3.38. Then, Babinet's principle was used to approximate the characteristic impedance of the coplanar waveguide structure, and the ADS LineCalc tool was used to calculate its physical parameters. Equation 3.7 shows Babinet's principle formula, where

$\eta_0$  is the characteristic impedance of free space equal to 377 ohms,  $\epsilon_{\text{reff}}$  is the effective dielectric constant,  $Z_{\text{cpw}}$  corresponds to the strip conductor impedance of the CPW structure, and  $Z_{\text{slot}}$  corresponds to the slot impedance of the twin-strip line structure equal to 200 ohms. The effective dielectric constant was approximated by equation 3.8 to be equal to 1.6, where  $\epsilon_r$  is the dielectric constant of the RT/Duroid 5880 substrate equal to 2.2. Therefore, the approximated strip conductor impedance of the CPW structure was calculated to be equal to 111.04 ohms. The calculated physical parameters of the twin-strip line structure were as follows: slot width was equal to 1.01 mm, strip conductor width was equal to 1.33 mm, and the length of the twin-strip line was equal to 5.9 mm.

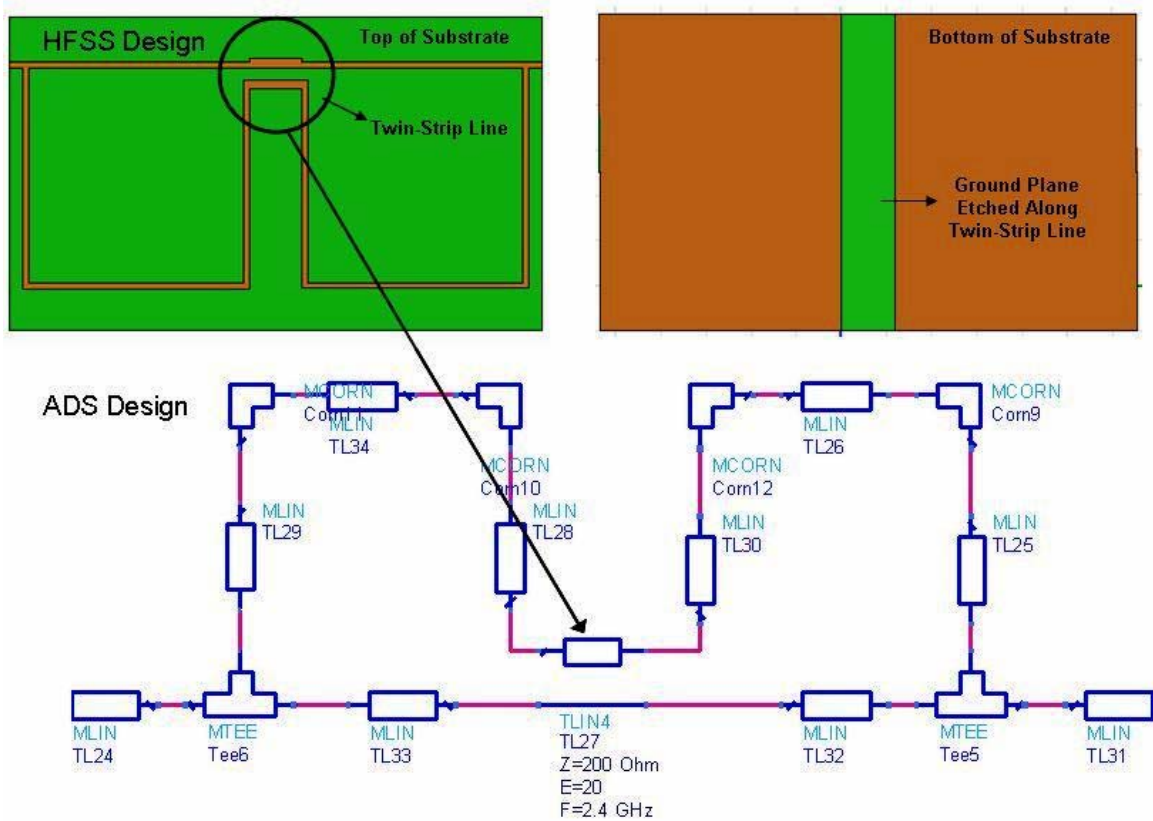


Figure 3.37 Ground Effects Microwave and Electromagnetic Simulations of the Balun Design

$$Z_{\text{slot}} \cdot Z_{\text{cpw}} = \frac{\eta^2}{4 \cdot \epsilon_{\text{reff}}} \quad (3.7)$$

$$\epsilon_{\text{reff}} = \frac{\epsilon_r + 1}{2} \quad (3.8)$$

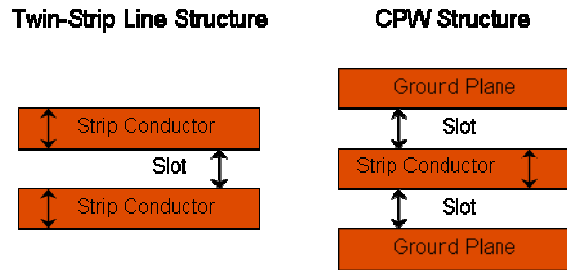


Figure 3.38 Babinet's Principle Approximation Between the Twin-Strip Line and CPW Structures

The ADS simulation represents an ideal transmission line model of the back-to-back Balun design as opposed to the HFSS simulation that represents the actual design. Figure 3.39 shows the comparison between the ADS and HFSS Balun design simulations. The differences among the two design simulations at other frequencies other than 2.4 GHz could be caused by the accuracy of the calculations used to determine the width and length of the twin-strip line for the HFSS simulation.

These results give us confidence that stopping the ground plane at the twin-strip line will not affect the performance of the microstrip narrow-band feed network at the design frequency of 2.4GHz. This design was fabricated and tested to confirm the simulation results.

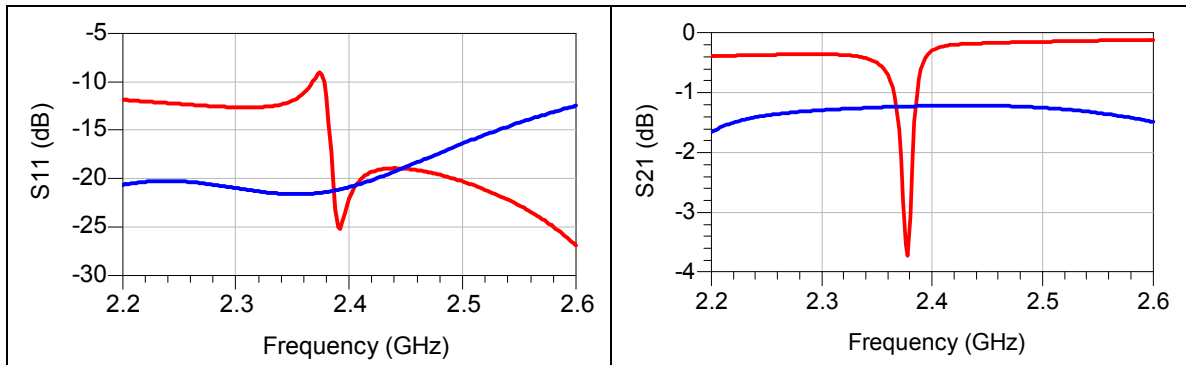


Figure 3.39 S-parameter Simulations for the Back-to-Back Balun Design. Red Trace- ADS Simulation. Blue Trace- HFSS Simulation. Left Plot- S11 (dB). Right Plot S21 (dB)

### 3.4 Fabrication

The self-complementary Archimedean spiral antenna design was etched on a 31-mil thick Rogers RT/Duroid 5880 substrate ( $\epsilon_r=2.2$ ). Figure 3.40 shows the fabricated design implemented with the narrow-band feed network. The antenna feed point was connected to the twin-strip lines at the bottom of the substrate through via holes filled with conductive silver epoxy. The Johanson surface mount components for the matching network (series capacitor-shunt inductor) were bonded between the twin-strip lines and the balanced output of the Balun using a re-flow process with solder paste. Finally, an RF connector was soldered to the unbalanced input of the Balun.

The back-to-back Balun design shown on figure 3.37 was milled on a 31-mil thick Rogers RT/Duroid 5880 substrate ( $\epsilon_r=2.2$ ). The ground plane under the twin-strip line that connects the two Baluns was also milled. Figure 3.41 shows the fabricated design. Two RF connectors were soldered to the unbalanced inputs of each Balun.

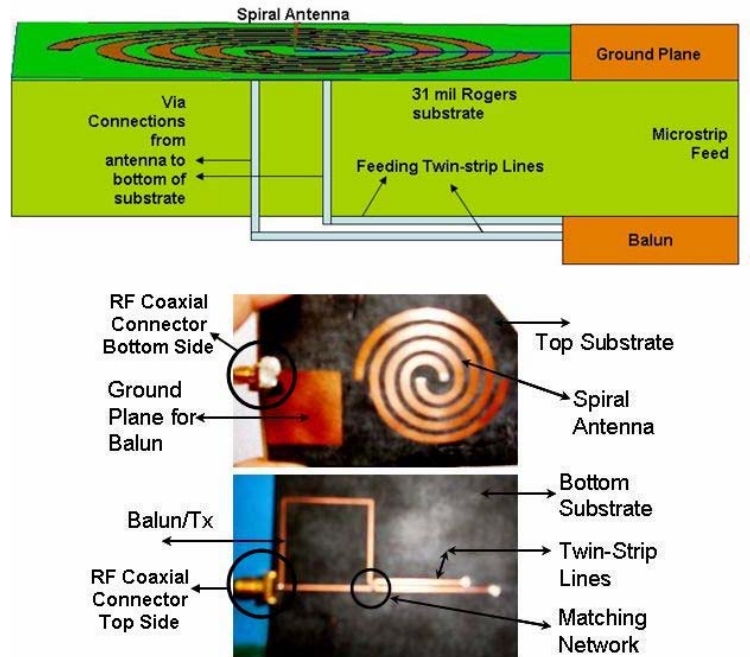


Figure 3.40 Fabricated Self-Complementary Archimedean Spiral Antenna with a Narrow-band Feed Network

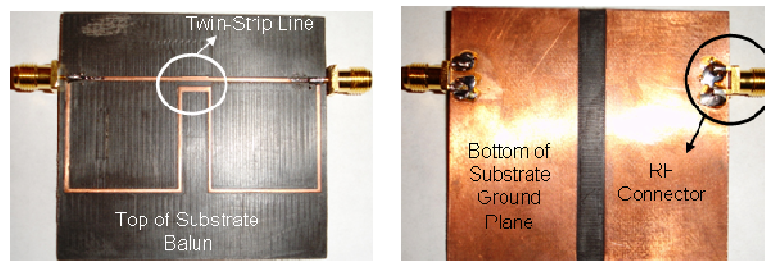


Figure 3.41 Fabricated Back-to-Back Balun Design

### 3.5 Measurements

In Chapter 2 and previous sections of Chapter 3, analytical methods were implemented to analyze and numerically compute the radiation characteristics of the Archimedean spiral antenna. S-parameters and radiation pattern measurements were performed in order to corroborate the results obtained in the simulations. Moreover, s-parameter measurements of the back-to-back Balun design were also performed to support the ground effects simulation results.

### 3.5.1 S-parameters Measurements

A vector network analyzer (VNA) was used to measure the s-parameters of the spiral antenna. A 1-port calibration was performed at the end of a coaxial RF cable connected to port 1 of the network analyzer. The 1-port SOL (Short-Open-Load) calibration consists of connecting a short, an open, and a load calibration standards to the end of the coaxial cable. Then VNA computed the calibration coefficients to account and correct for the loss of the path. Once the measurement setup was calibrated, the device under test (spiral antenna) was connected to the coaxial cable through the RF connector at the unbalanced input of the Balun, and the s-parameters of the antenna were recorded on the network analyzer. Figure 3.42 shows the comparison between simulated and measured  $S_{11}$  (dB) of the fabricated spiral antenna. At the designed frequency of 2.4 GHz, there is a 19dB of return loss with a 200 MHz 10-dB return loss bandwidth. The differences between the simulation and measurement could be explained by the fact that the simulated spiral antenna is not matched to the feed line, but the measured spiral antenna is matched to a 50-ohm feed line. The spiral antenna simulations do not include the lumped-element matching network, the Balun, and the coaxial RF connector.

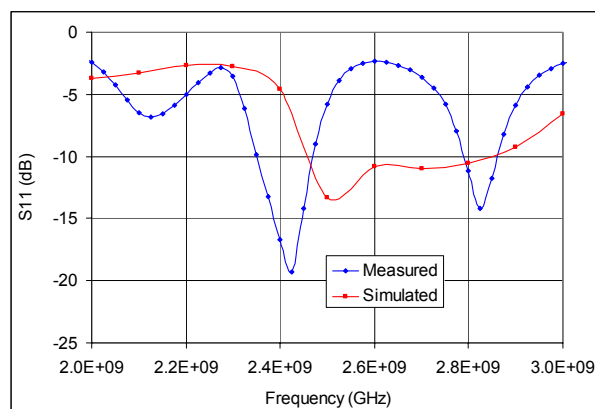


Figure 3.42 Comparison Between Simulated and Measured S-parameters of Archimedean Spiral Antenna. Red Trace- Simulated. Blue Trace- Measured

### 3.5.2 Radiation Pattern Measurements

Far-field radiation characteristics are measured by illuminating the test antenna by plane waves, that is waves with uniform amplitude and phase [5]. In order to approximate this ideal condition, the test antenna is separated from the source antenna or illumination source by a distance equal to the inner boundary of the antenna's far-field region [5]. This inner boundary is equal to  $2D^2/\lambda$ , where  $D$  is the antenna overall maximum dimension and  $\lambda$  is the antenna operating wavelength [5].

Radiation patterns are measured on the surface of a constant radius sphere [5]. The standard spherical coordinate system ( $r, \theta, \phi$ ) is used to identify any particular position on the sphere. However, only the two angular coordinates are needed for positional identification since the radial distance is maintained fixed. For the reason that it is impractical to measure a three-dimensional pattern, the minimum number of two-dimensional patterns needed to accurately represent the antenna radiation pattern is two [5]. A two-dimensional pattern is obtained by fixing one of the angles ( $\theta$  or  $\phi$ ) while varying the other [5]. For instance, elevation or E-plane patterns are obtained by fixing  $\phi$  ( $0 \leq \phi \leq 2\pi$ ) and varying  $\theta$  ( $0 \leq \theta \leq \pi$ ), and azimuthal or H-plane patterns are obtained by fixing  $\theta$  ( $0 \leq \theta \leq \pi$ ) while  $\phi$  is varied ( $0 \leq \phi \leq 2\pi$ ) [5].

The Archimedean spiral antenna was tested in an indoor free-space antenna range or anechoic chamber. The anechoic chamber has walls covered with RF absorbers to suppress electromagnetic interference and is protected from environmental conditions [5]. The source antenna was chosen to be a Yagi antenna operating at 2.4 GHz. The Yagi antenna is connected to a signal source, such as a vector network analyzer. The spiral antenna was mounted to a rotational pedestal using a short semi-rigid RF coaxial cable.

The rotational pedestal has the capability of rotating in various planes. The recording system is connected to the rotational mount, so that position references can be recorded simultaneously with measurements for angular positional identification [5].

Figures 3.43 and 3.44 show the radiation pattern measurements for the fabricated antenna characterized by two major circular lobes. The differences between the simulation and measurement could be explained by the fact that the spiral antenna simulations do not include the lumped-element matching network, the Balun, and the coaxial RF connector. The Balun ground plane could have caused interference in the pattern measurement. Also, there could be sources of error in the pattern measurement caused by the accuracy of directing the source antenna beam directly to the spiral antenna under test.

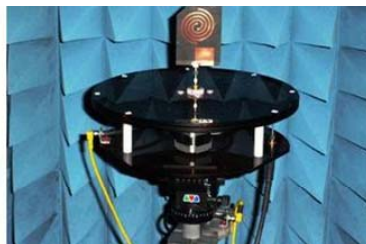
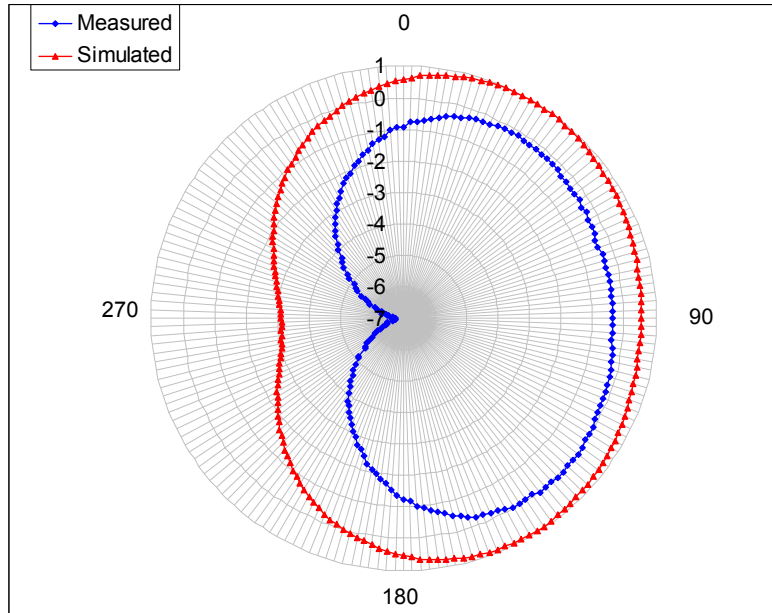


Figure 3.43 E-Plane Radiation Pattern Simulation and Measurement of Fabricated Spiral Antenna. Top- E Plane Pattern. Bottom- Antenna E-Plane Orientation. Red Trace- Simulation. Blue Trace- Measurement

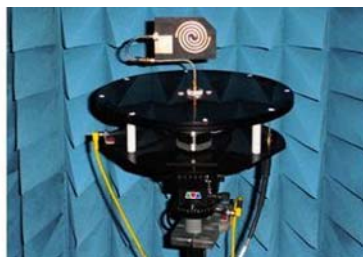
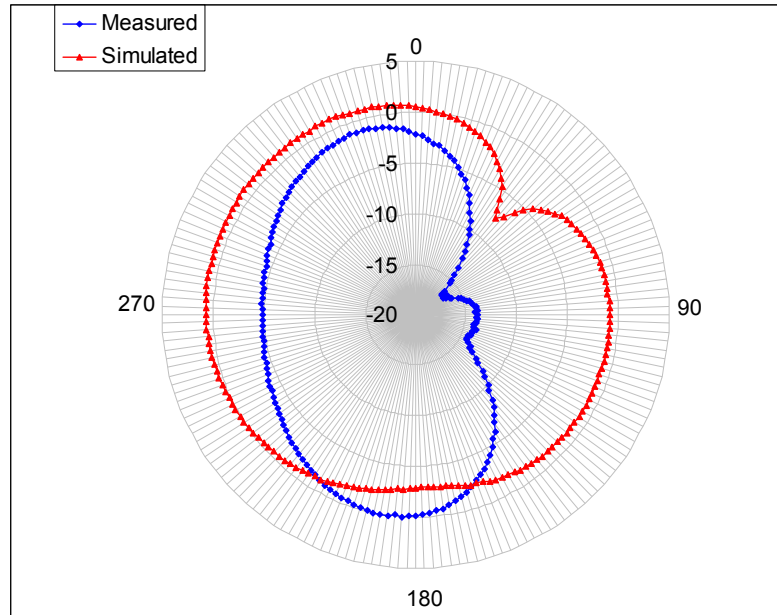


Figure 3.44 H-Plane Radiation Pattern Simulation and Measurement of Fabricated Spiral Antenna. Top- H Plane Pattern. Bottom- Antenna H-Plane Orientation. Red Trace- Simulation. Blue Trace- Measurement

### 3.5.3 Balun Measurements

A vector network analyzer (VNA) was used to measure the s-parameters of the back-to-back Balun design. A 2-port SOLT (Short-Open-Load-Thru) calibration was performed at the end of two coaxial RF cables connected to port 1 and port 2 of the network analyzer by connecting a short, an open, and a load calibration standards to the end of each coaxial cable. Next, a thru connection was made between ports 1 and 2 through the coaxial cables. Then VNA computed the calibration coefficients to account and correct for the loss of the paths. Once our measurement setup was calibrated, the device under test (back-to-back Balun design) was connected through the RF connectors

at the unbalanced input of each Balun in between ports 1 and 2 of the VNA at the end of the coaxial cables. Then, the S-parameters were recorded on the VNA.

Figure 3.45 shows the measured s-parameters of the back-to-back Balun design compared to the simulation results obtained with ADS. At 2.4 GHz, The S11 and S21 in dB from both simulation and measurements are close. For instance, S11 (dB) at 2.4GHz for the ADS design is -22.08 dB and for the measured design is -21.11 dB. S21 (dB) at 2.4 GHz for the ADS design is -0.3 dB and for the measured design is -0.7 dB. However, there is a shift in the response between measured data and simulations of about 50 MHz approximately. This frequency response shift between the simulation and the measured data could be explained by the inductance added by the RF coaxial connectors.

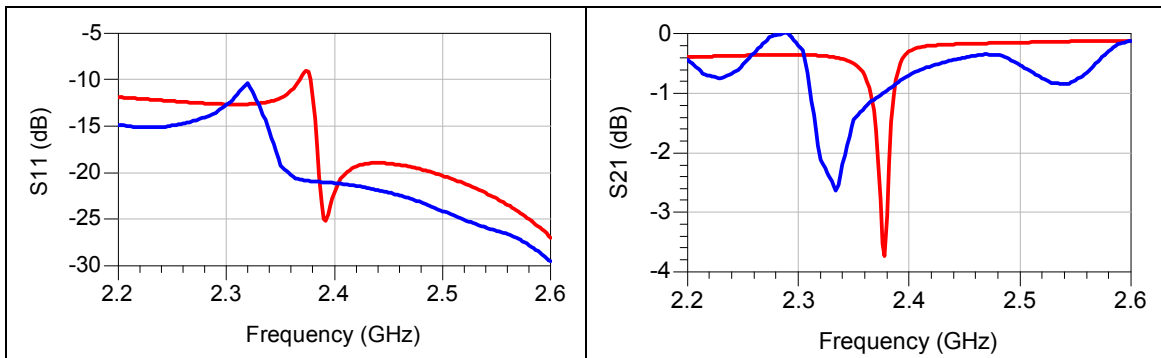


Figure 3.45 Measured S-parameters of Fabricated Back-to-Back Balun Design. Red Trace- ADS Simulation. Blue Trace- Measured Data. Left Plot- S11 (dB). Right Plot S21 (dB)

### 3.6 RF Coaxial Connector Electromagnetic Simulations

The purpose of this section was to investigate how RF coaxial connectors, such as the ones used for our fabricated designs, perform at the frequency range of interest. Therefore, the PSF-S01 end launch connector was chosen to be studied by means of electromagnetic simulations.

The connector was drawn in HFSS using available dimensions from vendor's datasheet. Dimensions that were not available in the vendor's datasheet, such as the

diameter of the dielectric present between the inner and outer conductors and the diameter of the inner conductor, were measured using a micrometer. The dielectric present between the inner and outer conductors was assumed to be a dielectric core material with a dielectric constant equal to 3.255.

The connector was simulated in a back-to-back configuration using a microstrip transmission line. The width of the microstrip line was designed to be 50 ohms at 2.4 GHz, and the length was designed to be 64 degrees at 2.4 GHz. The calculated width and length were equal to 18.3 and 540 mils respectively. The substrate used for the simulations was an 8-mil thick RO4003 Rogers material with a dielectric constant equal to 3.38. Wave port assignments were used as the excitations at the input of each connector as shown by figure 3.46.

We expect for a good RF connector to have a return loss of 20dB or better and an insertion loss of 0.2 dB or better at the designed frequency range of operation. Figure 3.47 shows the simulation results of the back-to-back connector design. The connector shows acceptable return and insertion loss performance to 3GHz based on the expected standards of operation for RF coaxial connectors. At our frequency of interest of 2.4 GHz, the return and insertion loss are equal to 23.4 and 0.08 dB respectively.

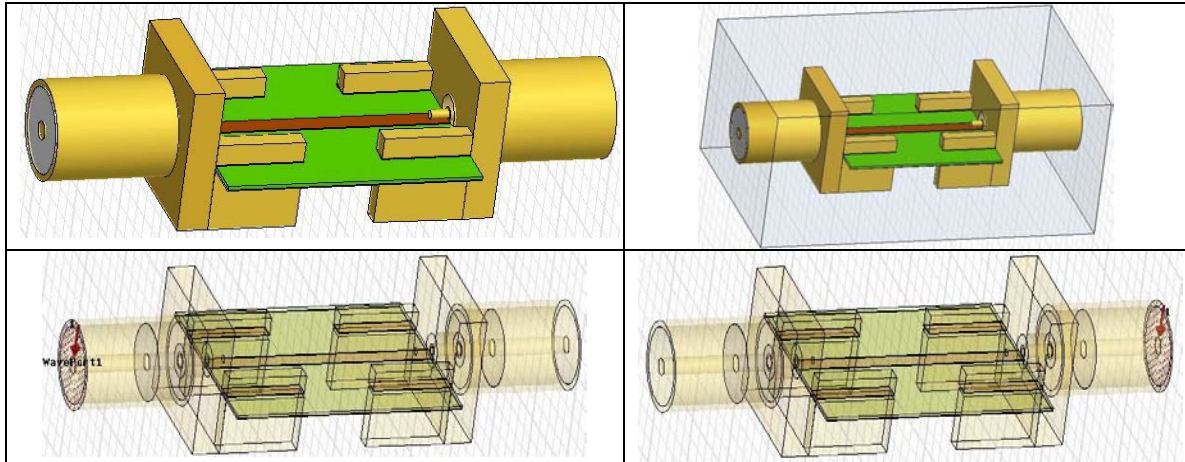


Figure 3.46 Back-to-Back Connector Design. Top Left- Connector Design in HFSS. Top Right- Air Boundary Assignment. Bottom Left- Wave Port 1 Reference Plane. Bottom Right- Wave Port 2 Reference Plane

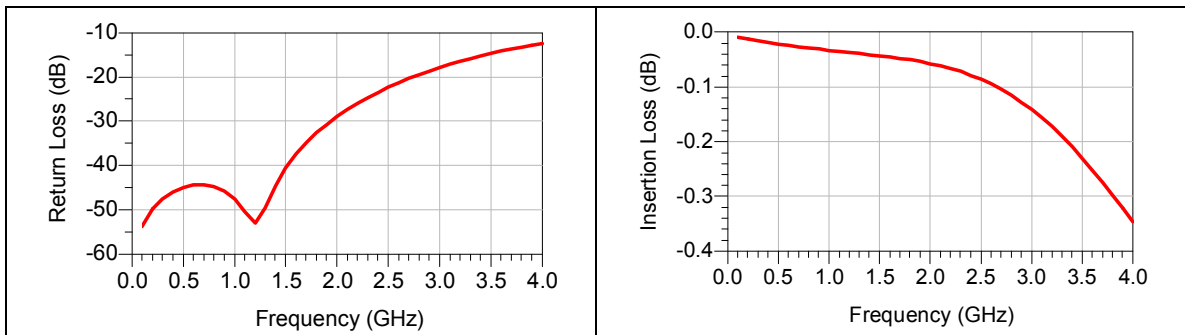


Figure 3.47 S-parameter Simulations of Back-to-Back Connector Design. Left Plot- Return Loss (dB). Right Plot- Insertion Loss (dB)

### 3.7 Summary and Conclusions

With the aim of electromagnetic and circuit-level simulations, the Archimedean spiral antenna performance was successfully analyzed to the point where it is connected to the balanced feed network. It was shown that the twin-strip line feeding configuration does not affect the radiation characteristics of the antenna. It was also demonstrated that there is a trade-off in the antenna performance when the substrate backing up the antenna is reduced in thickness from an ideal  $\lambda/4$  thickness.

A narrow-band feed network involving a planar Balun was designed and simulated using the Agilent Advanced Design System (ADS) software in order to connect the antenna balanced input to an unbalanced line for fabrication and measurement purposes. Furthermore, the Balun was measured with the antenna as well as separate from the antenna in a back-to-back configuration. Both the Archimedean spiral antenna and Balun measurements agreed with the simulations.

The RF coaxial connector was also simulated in HFSS in a two-port back-to-back configuration so as to investigate its performance at the frequency range of interest of 2.4 GHz. Based on the expected standards of operation for RF coaxial connectors, the connector showed acceptable return and insertion loss performance to 3GHz.

## Chapter 4

### Frequency Selective Surfaces

#### 4.1 Introduction

As it was shown on chapters 2 and 3, the radiation properties of an antenna are affected by the presence of a perfect electric conducting (PEC) ground plane. Moreover, if the antenna is placed too close to this conducting surface, the image currents cancel the currents in the antenna resulting in poor radiation efficiency [17]. In order to prevent poor radiation efficiency due to the close proximity of a ground plane to the antenna, a quarter-wavelength space can be included between the radiating element and the ground plane. However, this design approach brings a fixed thickness of  $\lambda/4$  into the backing configuration that not only increases the overall physical dimensions of the antenna but also limits the performance of inherently broad-band antennas such as the spiral antennas discussed in chapter 2 and 3.

Metals support electromagnetic surface waves that bond to the interface between metal and free space and do not couple to external plane waves if the surface is smooth and flat [17]. By incorporating a special texture on a conducting surface, it is possible to alter its radio-frequency electromagnetic properties as well as its surface impedance [17]. This type of metal surfaces coated with resonant structures is known as frequency selective surfaces (FSS) and can serve as a substrate for antennas allowing them to lie directly adjacent to the ground plane surface without being shorted out [18].

In this chapter, the background theory of operation for frequency selective surfaces is analyzed, and a low-frequency structure operating at 2.4GHz is evaluated that could potentially be used to miniaturize an antenna in the z-direction.

#### 4.2 Theory of Operation

A frequency-selective surface is a surface which exhibits different reflection and/or transmission properties as a function of frequency [1]. Two basic types of FSS are an array of dipoles and an array of slots both followed by a dielectric slab. An array of resonant dipoles acts as a band-stop filter by passing waves above and below the dipole resonant frequency but not at the resonant frequency. On the other hand, the complementary array of slots acts as a band-pass filter by passing waves at the resonant frequency of the slots but rejecting them at higher and lower frequencies. As shown by figure 4.1, the action of the dipoles is equivalent to that of a series-tuned circuit on a transmission line and that of the slots is analogous to a parallel tuned circuit. Therefore, the inductor and capacitor resonate at the pass or stop frequencies.

Surface waves travel on a flat metal conductor until they reach an edge where they can radiate into free space translating into a multi-path interference that can be seen as ripples in the radiation pattern [17]. On the contrary, surface waves will radiate vertically if scattered by a surface texture. Smooth conducting sheets have low surface impedance, but a textured surface or FSS can have high surface impedance (greater than 377 ohms).

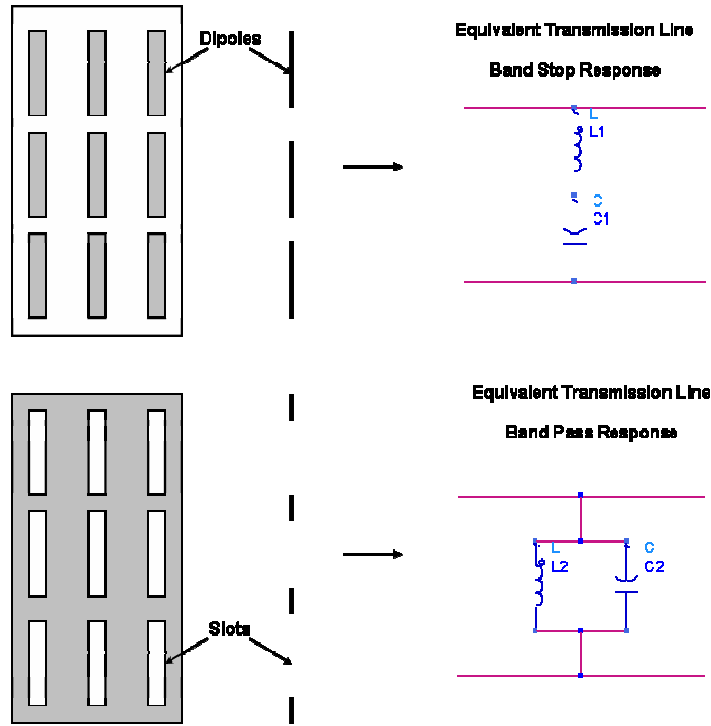


Figure 4.1 Basic Frequency Selective Surfaces [1]

The type of FSS described in this chapter consists of a lattice of small mushroom-shaped protrusions made of metal plates, connected to a common ground plane by vertical metal pins as shown by figure 4.2 [18]. The surface impedance of this structure is characterized by an equivalent parallel resonant LC circuit and is given by equation 4.1. At low frequencies it is inductive and supports transverse magnetic (TM) waves. At high frequencies it is capacitive and supports transverse electric (TE) waves. Near the LC resonance frequency (equation 4.2), the surface impedance is very high and electromagnetic waves are reflected with zero phase shift. In this region, waves are not bound to the surface but radiate readily into the surrounding space. The fractional bandwidth of the gap between the TM and TE bands is given by equation 4.3 where  $t$  is the thickness of the surface and  $\lambda_0$  is the wavelength at resonance.

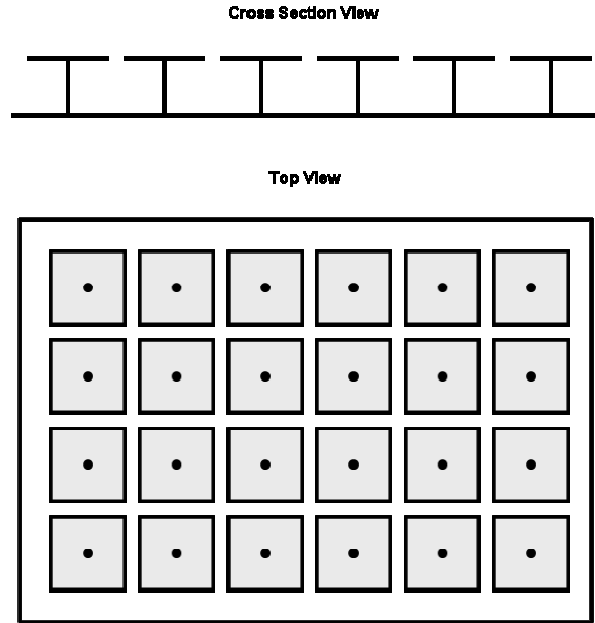


Figure 4.2 Cross Section and Top View of a High-Impedance Surface [17]

$$Z_s = \frac{j \cdot \omega \cdot L}{1 - \omega^2 \cdot L \cdot C} \quad (4.1)$$

$$\omega_0 = \frac{1}{\sqrt{L \cdot C}} \quad (4.2)$$

$$B = t \cdot \frac{2 \cdot \pi}{\lambda_0} \quad (4.3)$$

As the structure shown on figure 4.2 interacts with electromagnetic waves, currents are induced in the top metal plates [17]. A capacitance is built up on the ends of the plates as a voltage is applied to the top surface. An inductance is formed by the magnetic field associated with the currents that flow around a path through the vias and bottom plate. Therefore, in a two-layer design such as the one shown on figure 4.2, the capacitors are formed by the fringing electric fields between adjacent metal patches, and the inductance is fixed by the thickness of the structure.

The three-layer design structure shown on figure 4.3 achieves a lower resonance frequency for a given thickness by using capacitive loading that consists of parallel-plate capacitors formed by the top two overlapping layers [17]. This low-frequency structure would work perfectly for the spiral antennas described on chapter 2 operating at 2.4 GHz. This design can maintain a thickness of a few millimeters with a corresponding inductance of a few nanohenrys and a capacitance of several picofarads. However, by forcing a thin structure to have a low resonance frequency, the bandwidth is also reduced. Operating bandwidths of 6 GHz are common for two-layer FSS structures at a design frequency of 14 GHz. Moreover, operating bandwidths of 400 MHz are common for three-layer FSS structures at a design frequency of 2.4 GHz. The overall thickness of a low-frequency FSS structure operating at 2.4 GHz can be about 4 mm, which is considered a miniature backing design for an antenna compared to the  $\lambda/4$  thick substrate approach with a thickness of about 21 mm at 2.4 GHz.

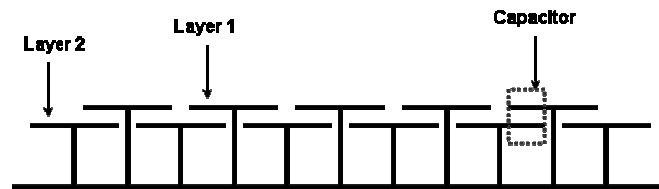


Figure 4.3 Three-Layer High-Impedance Surface [17]

The high-impedance surface is particularly applicable to the field of portable hand-held communications, in which the interaction between the antenna and the user can have a significant impact on antenna performance. Moreover, using this ground plane structure as a shield between the antenna and the user in portable communications equipment can lead to higher antenna efficiency, longer battery life, and lower weight [17].

As shown in [8], by placing a spiral antenna over a FSS structure rather than a PEC ground plane, a reduction of more than 69% in antenna height can be obtained. Furthermore, in order to maintain the inherent frequency-independent characteristics of a spiral antenna, varactor diodes or reversed-biased diodes can be connected between each unit cell in the periodic surface texture and its four neighbors to tune the resonance frequency by changing the voltage of the diodes which adjusts the capacitance between neighboring cells as shown in [19].

#### 4.3 Summary and Conclusions

Antennas can be potentially miniaturized in the z-direction by replacing the PEC ground plane separated from the antenna by a  $\lambda/4$  thick substrate with a FSS structure that allows the ground plane conductor to be in close proximity to the antenna without affecting its radiation performance. This type of high impedance structure not only makes it possible to reduce the antenna height by at least 69%, but also provides the opportunity of maintaining broad-band antenna responses by means of including tunable varactor diodes to the structure that adjusts the resonance frequency of the FSS. Lastly, a two-layer FSS structure operating at 2.4 GHz was presented that could serve as the substrate for the spiral antenna designs introduced in chapters 2 and 3 to make them miniature in the z-direction.

## Chapter 5

### Miniature Coil Antennas

#### 5.1 Introduction

Advances in technology have placed a great emphasis not only on broadband antennas to cover an entire design application range but also on antenna miniaturization to cope with the demands of making electronic devices smaller. There are fundamental limits to how small an antenna can be at a particular wavelength and still behave as an efficient radiating device. In this chapter, the fundamental limits of electrically small antennas are studied to distinguish and examine the restrictions of miniature coil antennas.

Research and measurement characterization were oriented to investigate the feasibility of using chip inductors mounted in a 1-port configuration as electrically and physically small helical antennas operating at the frequency range of 1 to 3 GHz. The research focuses on reflection coefficient and radiation efficiency measurements in order to characterize coil performance as electrically small antennas.

#### 5.2 Background Theory

Antenna size with respect to the wavelength is the parameter that will have the major influence on the radiation characteristics such as gain, efficiency, and polarization purity [16]. An antenna is considered to be electrically small when its maximum physical dimension is small compared to the operating wavelength [14]. Therefore, the coil

inductors used for this investigation are considered to be electrically small based on the physical dimensions and operating wavelengths shown on tables 5.1 and 5.2.

A coil inductor can be analyzed as a helical antenna, which is a conductor that is wound into a helical shape and properly fed at the input of the helix [4]. Figure 5.1 shows the typical geometry for a helix with N turns, where D is the diameter of helix calculated between centers of coil material, d is the diameter of helix conductor, S is the spacing between centers of coil material, and L is the length of one turn. The length of one turn is given by equation 5.1, where C is the circumference of helix equal to  $\pi D$  [4]. Another important parameter of the helical antenna is the pitch angle  $\alpha$  defined by equation 5.2, which is the angle formed by a line tangent to the helix wire and a plane perpendicular to the helix axis [5].

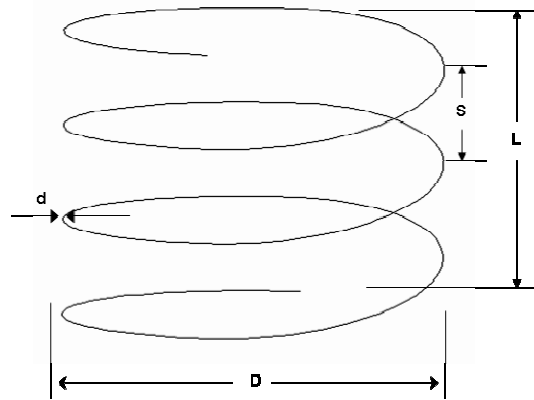


Figure 5.1 Typical Geometry for a Helix

$$L = \sqrt{C^2 + S^2} \quad (5.1)$$

$$\tan(\alpha) = \frac{S}{C} \quad (5.2)$$

A helix of fixed diameter collapses to a loop as the spacing between turns approaches zero ( $\alpha=0^\circ$ ) [15]. On the other hand, a helix of fixed spacing between turns straightens out into a linear conductor as the diameter approaches zero ( $\alpha=90^\circ$ ) [15].

Therefore, a true helix is formed when the pitch angle is between 0 and 90 degrees ( $0^\circ < \alpha < 90^\circ$ ) with a circumference greater than zero but less than the circumference when the helix is reduced to a loop [5]. The radiation characteristics of the antenna can be varied by controlling the size of its geometrical properties compared to the wavelength [5]. Moreover, the input impedance is critically dependent upon the pitch angle and the size of the conducting wire [5].

The coil inductors used for this investigation can be compared to helical antennas operating in the normal mode of radiation that occurs when the dimensions of the helix are small compared to the operating wavelength, and hence they have neither a wide-band nor a high efficiency [15]. This normal mode of operation is related to the lowest transmission mode of operation  $T_0$  used to describe how an electromagnetic wave propagates along an infinitely long helix [15]. In this mode, a helix has adjacent regions of positive and negative charge separated by many turns. This is the mode that occurs on low frequency inductances [15].

A helical antenna operating in the normal radiation mode exhibits maximum radiation broadside to the plane of the antenna, and the current is assumed to be uniform in magnitude and in-phase over the entire length of the helix [15]. For a small helix ( $L \ll \lambda$ ), the far-field is independent of the number of turns. Therefore, the axial ratio of the polarization ellipse can be defined as the ratio of the far-field  $E_\theta$  component of the short dipole to the far-field  $E_\phi$  component of the small loop [15].  $E_\theta$  and  $E_\phi$  are 90 degrees out of phase. Helical antennas could have circular polarization instead of elliptical polarization if the magnitudes of the  $E_\theta$  and  $E_\phi$  components are equal.

### 5.3 Measurement Characterization

The inductors used for this investigation were 0402 and 0603 Coilcraft surface mount chip inductors with inductances of 47 and 270nH respectively. The radiation efficiency varies depending upon the direction the inductor is bonded [10]. Consequently, the responses of six 1-port configurations were analyzed to determine the most efficient design pattern. The 0402 inductors have a remarkable difference in the wire windings across them. The spacing between each wire turn changes across the inductor length, so the wire windings look more closely spaced towards one end of the coil wrap-up. Thus, this difference was taken as the reference point to bond the 0402 inductors in six different 1-port orientations. On the other hand, the 0603 inductors have a polarity dot marked on one side of the plastic cap covering the top of the surface mount chip, which was taken as the reference point to bond these inductors in the six different 1-port orientations, as shown by figure 5.2.

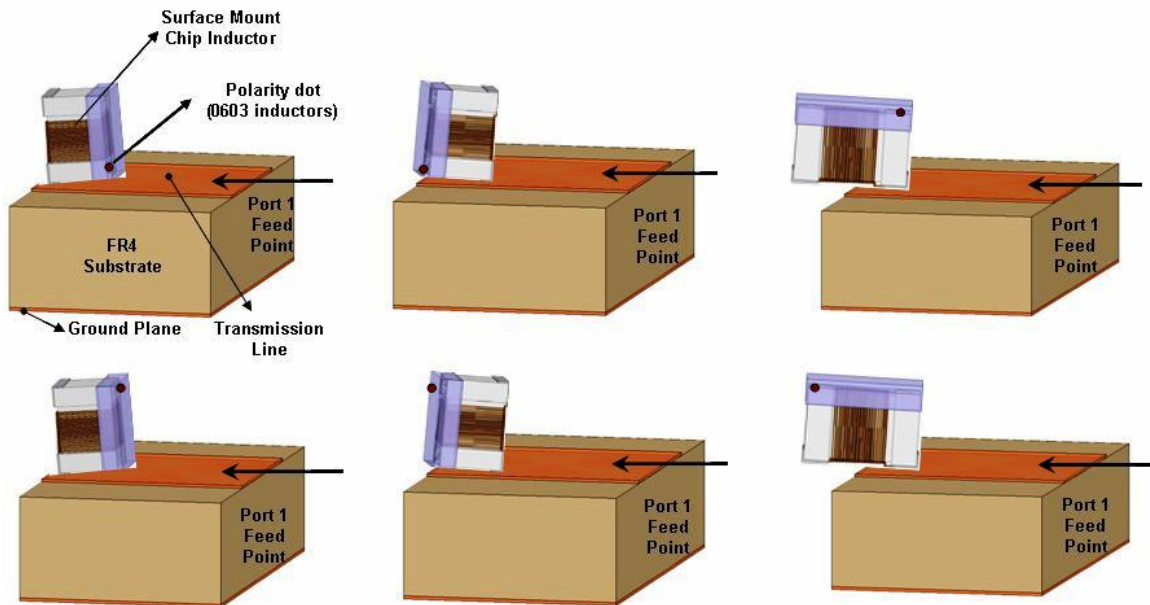


Figure 5.2 Six 1-Port Bonding Configurations Used to Characterize Surface Mount Chip Inductors as Miniature Antennas

Based on preliminary s-parameter measurements, the 0402 and 0603 inductors showed a lower reflection response when bonded vertically on the side of the reference point looking away from the feed line. Also, the inductors bonded horizontally on the reference point side showed a promising reflection response. The best vertical and horizontal orientations were chosen for the subsequent measurements and calculations (figure 5.3).

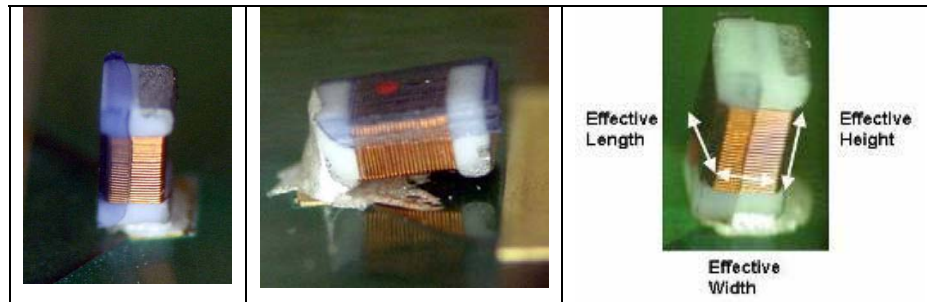


Figure 5.3 Surface Mount Chip Inductor. Left- Vertical Configuration. Middle- Horizontal Configuration. Right- Inductor Parameters

Total wire length and diameter of electrically small antennas are two of the physical properties that influence their electromagnetic behavior. Therefore, we estimated these resonant properties based on the number of turns, effective length, width, and height of the inductors provided on the Coilcraft datasheets (figure 5.3). Estimated values for total wire length and diameter were obtained using formulas 5.3 and 5.4 respectively, where “N” is the number of turns, “E” is the effective length, “C” is the effective width, and “G” is the effective height. The estimated values are summarized on table 5.1. Moreover, the pitch angle  $\alpha$  was estimated for the 47nH 0402 and 270nH 0603 chip inductors to be equal to 6.9 and 7.7 degrees respectively.

$$L = (E \cdot N \cdot 2) + (C \cdot N \cdot 2) \quad (5.3)$$

$$d = \frac{G}{N} \quad (5.4)$$

Table 5.1 Calculation of Inductor Parameters

Inductor / Parameters	E (mm)	C (mm)	G (mm)	N	d (mm)	L (mm)
47nH (0402)	0.51	0.66	0.56	13	0.043	30
270nH (0603)	0.76	1.07	0.86	23	0.037	84

Strong radiation is observed when the inductor's wire length is approximately  $0.45\lambda_0$  [10]. According to the calculations shown in table 5.2, the wavelengths were corrected to account for the inductor's geometry, which essentially consists of the wire being wrapped around a Teflon core. Thus, the wavelengths ( $\lambda_0$ ) were divided by the square root of the dielectric constant of Teflon that is equal to 2.1. The Teflon-corrected wavelength ( $\lambda_g$ ) and optimal wire length ( $0.45\lambda_g$ ) values are summarized in table 5.2.

By comparing the optimal  $0.45\lambda_g$  wire lengths calculated at the radiation frequencies to the actual stretched lengths, we concluded that they match well. For instance, in the case of the 47nH 0402 inductor, the total estimated wire length is 30 mm (table 5.1), and the  $0.45\lambda_g$  values for the vertical and horizontal 1-port configurations are 33 and 44 mm, respectively (table 5.2). Similarly, for the 270 nH 0603 inductor, the estimated wire length is 84 mm (table 5.1), and the  $0.45\lambda_g$  values for the vertical and horizontal 1-port configurations are 87 and 83 mm, respectively (table 5.2). Since we did not find an equation that relates bonding orientation to radiation efficiency, we used the best vertical and horizontal orientations found in the preliminary s-parameter measurements for subsequent measurements and radiation parameters calculations.

Table 5.2 Calculation of Wire Length for Optimal Radiation Performance

Inductor	Bonding Configuration	$f_0$ (GHz)	$\lambda_0$ (mm)	$\lambda_g$ Teflon (mm)	$0.45*\lambda_g$ (mm)
47nH (0402)	1-port Vertical	2.861	105	72	33
47nH (0402)	1-port Horizontal	2.14	140	97	44
270nH (0603)	1-port Vertical	1.07	280	193	87
270nH (0603)	1-port Horizontal	1.12	268	185	83

### 5.3.1 S-parameter Measurements

S-parameter measurements were performed using the best vertical and horizontal 1-port configurations with the samples radiating into free space (figure 5.4). Samples were mounted on 59 mil thick FR4 test fixtures, which were also used for efficiency measurements. These S-parameter measurements were also repeated with the samples inside a conducting sphere for efficiency calculation purposes. The loss factor or mismatch loss for these 1-port measurements was calculated using equation 5.5. Moreover, the loss factor of the miniature coil antennas (inductors bonded in a 1-port configuration), when radiating into free space as well as inside a conducting sphere (Wheeler cap), provides an insight into the radiation efficiency of the antennas.

$$LF = 1 - (|S_{11}|)^2 \quad (5.5)$$

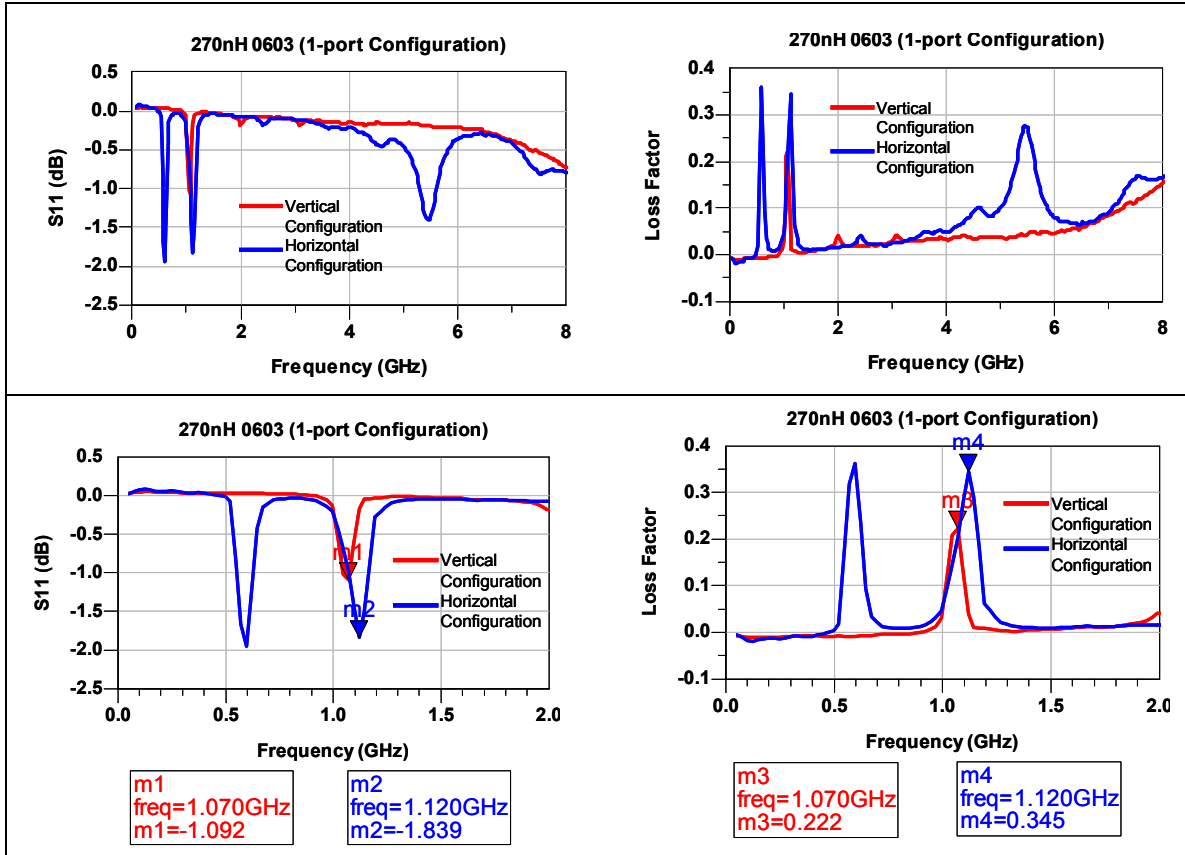


Figure 5.4 S-parameters of 270 nH 0603 Coil Inductor Bonded in a 1-Port Configuration Radiating into Free Space. Top Left- Broad-band S11 (dB) Response. Top Right- Broad-band Loss Factor. Bottom Left- Narrow-band S11 (dB) Response. Bottom Right- Narrow-band Loss Factor. Red Trace- Inductor Bonded in a Vertical Configuration. Blue Trace- Inductor Bonded in a Horizontal Configuration

### 5.3.2 Efficiency Measurements

An electrically small antenna can be represented by a lumped element circuit whose input impedance is given by equation 5.6, where  $R_A$  is the real part of the antenna's input impedance and  $X_A$  is the antenna's reactance [5]. The real part of the antenna's input impedance is defined by equation 5.7, where  $R_r$  is the radiation resistance and  $R_L$  is the loss resistance of the antenna [5].

$$Z_A = R_A + j \cdot X_A \quad (5.6)$$

$$R_A = R_r + R_L \quad (5.7)$$

The radiation resistance accounts for the radiated power and the loss resistance accounts for the dissipated power. The total antenna efficiency  $e_o$  is given by equation 5.8, where  $e_r$  is the reflection efficiency and  $e_{cd}$  is the conduction and dielectric efficiency. Reflection efficiency represents the mismatch between the transmission line and the antenna, and conduction and dielectric efficiency represent dissipative losses [5]. Reflection and conduction efficiency are defined by equations 5.9 and 5.10 respectively.

$$e_o = e_r \cdot e_{cd} \quad (5.8)$$

$$e_r = 1 - (|\Gamma|)^2 \quad (5.9)$$

$$e_{cd} = \frac{R_r}{R_L + R_r} \quad (5.10)$$

Efficiency measurements are performed to experimentally find the loss resistance of the antenna by using the principles of the Wheeler Cap method. This method consists of placing the antenna inside a conducting shell, which effectively eliminates  $R_r$  [11]. Therefore, the resistive term of the antenna's input impedance given by equation 5.7 will be only determined by loss resistance  $R_L$  when the antenna is measured inside the conducting shell environment. Then, the radiation resistance can be experimentally determined by subtracting the input impedance of the antenna measured with the antenna inside the shell from the input impedance of the antenna radiating into an anechoic environment [12].

The conducting shell or Wheeler cap used for efficiency measurements is shown in figure 5.5. This Wheeler cap consists of a rectangular cavity milled in the center of a piece of aluminum carrier. The chip inductor sample mounted on a FR4 test fixture is

placed inside this cavity with the RF coaxial connector sticking out of the cavity. The size of this cavity is 3.1 cm long, 1 cm wide, and 0.5 cm deep. An RF coaxial cable was used to connect the chip inductor sample to port 1 of the Vector Network Analyzer to perform S-parameter measurements.

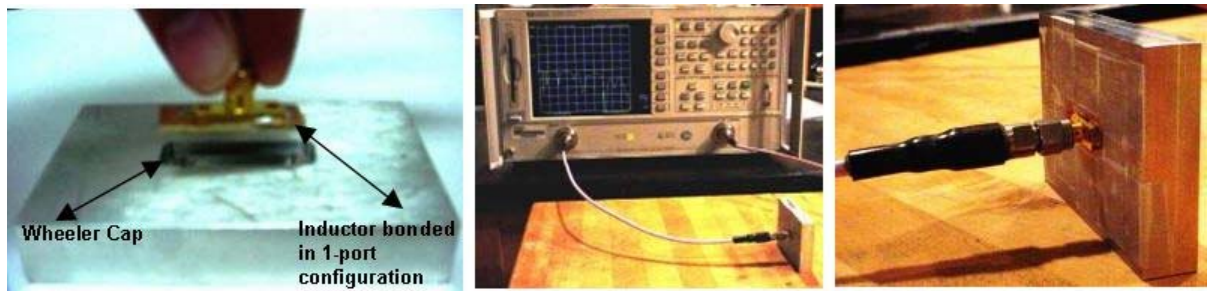


Figure 5.5 Efficiency Measurements

S-parameter measurements were performed with the samples inside the Wheeler cap (figure 5.5). Then, radiation efficiency was calculated using equation 5.11, where  $S_{11_{wc}}$  refers to the measurements when the antennas are inside the Wheeler cap, and  $S_{11_{fs}}$  refers to the measurements when the antennas are radiating into free space. Figure 5.6 shows the s-parameter measurements of the inductor antennas radiating inside the Wheeler Cap, and Figure 5.7 shows radiation efficiency calculations.

Equation 5.11 describes the constant power loss method to calculate radiation efficiency for small antennas (i.e.,  $< \lambda/10$ ). Equation 5.11 is proven to be mathematically equivalent to equation 5.10 [13]. This method assumes a constant power loss for a small antenna, with and without the Wheeler cap, whose radiation resistance is typically small in comparison to the 50-ohm measuring system source resistance [13]. The constant power loss method follows the same measurement principles as the Wheeler Cap method and defines radiation efficiency as the ratio of total power radiated by total power accepted by the antenna at its input terminals during radiation [5].

$$\eta = \frac{(|S_{11_{wc}}|)^2 - (|S_{11_{fs}}|)^2}{1 - (|S_{11_{fs}}|)^2} \quad (5.11)$$

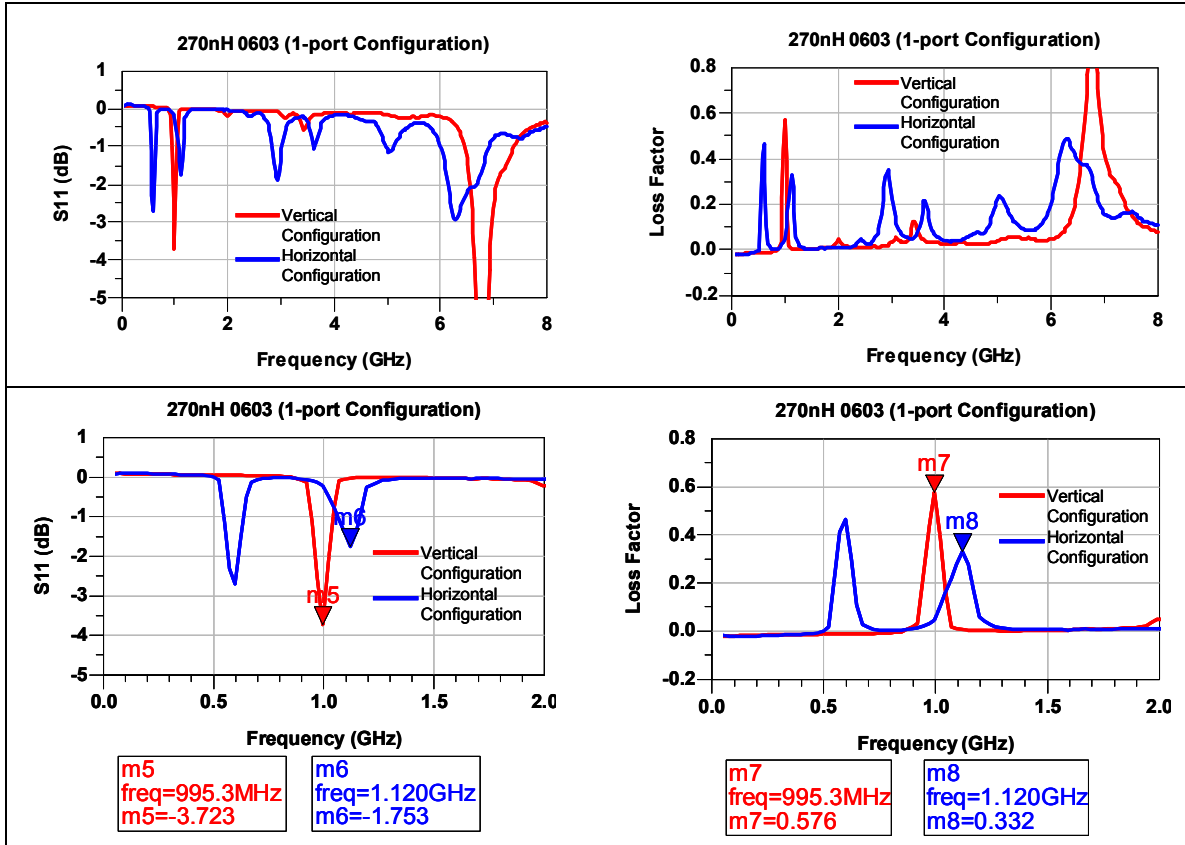


Figure 5.6 S-parameters of 270 nH 0603 Coil Inductor Bonded in a 1-Port Configuration Radiating Inside the Wheeler Cap. Top Left- Broad-band S11 (dB) Response. Top Right- Broad-band Loss Factor. Bottom Left- Narrow-band S11 (dB) Reponse. Bottom Right- Narrow-band Loss Factor. Red Trace- Inductor Bonded in a Vertical Configuration. Blue Trace- Inductor Bonded in a Horizontal Configuration

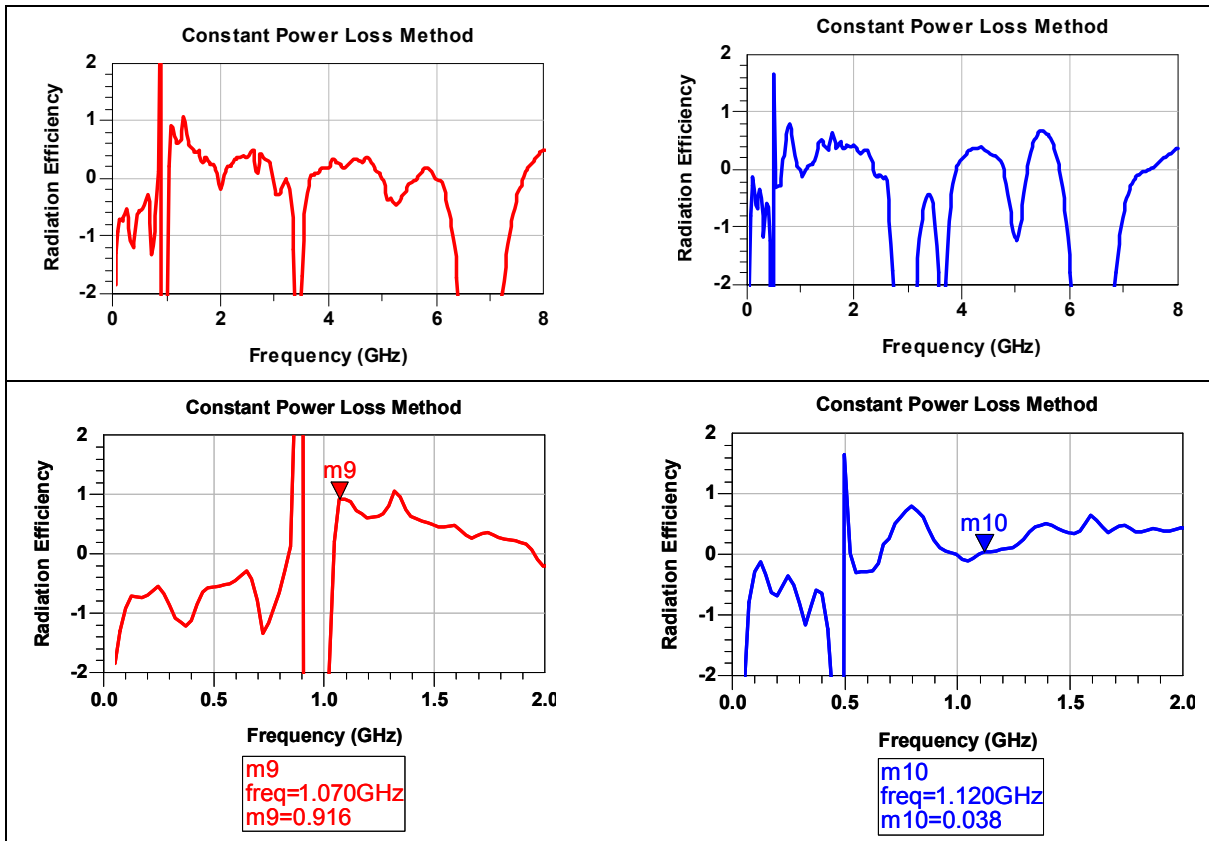


Figure 5.7 Radiation Efficiency of 270 nH 0603 Coil Inductor Bonded in a 1-Port Configuration. Top Left- Broad-band Response of Inductor in a Vertical Configuration. Top Right- Broad-band Response of Inductor in a Horizontal Configuration. Bottom Left- Narrow-band Response of Inductor in a Vertical Configuration. Bottom Right- Narrow-band Response of Inductor in a Horizontal Configuration

For the vertical 270nH 0603 sample, we obtained a very high efficiency of 91.6%, which is explained by a shift in resonance frequency from 1.070 GHz to 995.3 MHz rather than the existence of high radiation efficiency. In addition, the horizontal 270nH 0603 sample showed a very low radiation efficiency of 3.8% without a shift in resonance frequency. The loss factor does not significantly decrease when placed inside the Wheeler cap, generating this low efficiency; in fact, in some cases the loss factor increases when measured inside the Wheeler Cap. Based on our current efficiency results, we can conclude that these coil inductors have resonant frequencies with very low radiation efficiencies.

In order for the loss mechanisms and near fields of the antenna to behave the same way when inside the conducting sphere (Wheeler cap) as when it is radiating in free space, the Wheeler cap should have a radius of  $\lambda/2\pi$  [10]. This radius represents the transition between the antenna's energy-storing near-field and its radiating far-field [5]. The Wheeler cap used for the efficiency measurements did not have the specified radius, and this could have disturbed the coil antennas' near fields producing the frequency shift between shielded and unshielded measurements as well as the high loss for the shielded measurements. Moreover, electrically small antennas are difficult to measure properly because when they are connected to a measuring device a current will flow in the outer conductor of the cable connecting the antenna creating spurious radiation [16]. This spurious radiation will frequently completely mask the characteristics of the antenna under test yielding results that include the connecting cable [16].

Antennas are resonant at a frequency where they exhibit the greatest effective volume, and their resonant Q decreases with increasing effective volume [14]. Furthermore, antennas with dimensions which are small compared to a wavelength exhibit large radiation quality factors. Radiation quality factor Q equals the antenna reactance (stored energy) divided by the antenna resistance (radiated energy) [14]. Thus, there is more non-propagating energy stored than energy radiated leading to predominantly reactive input impedances. Also, because of the large radiation quality factors, the presence of even small resistive losses leads to very low efficiencies [12].

The basic limitations of electrically small antennas are imposed by the free-space wavelength that the antenna element must couple to [5]. These limitations are derived by assuming that the entire antenna structure with a largest linear dimension of  $2r$  is

enclosed within a sphere of radius  $r$  [5]. When the sphere enclosing the antenna element becomes very small, there exist no propagating modes so the  $Q$  of the system becomes very large. Thus, the fundamental limit on the electrical size of an antenna is related to the lowest achievable  $Q$  at its largest linear dimension, which is independent of the geometrical configuration of the antenna within the sphere of radius  $r$  [5]. The shape of the radiating element within the bounds of the sphere only determines what modes are excited [5]. The fundamental limit of electrically small antennas is given by equation 5.12, where  $k$  is the wave number equal to  $2\pi/\lambda$ , and  $r$  is the radius of the sphere enclosing the antenna [16].

$$Q = \frac{1}{(k \cdot r)^3} \tag{5.12}$$

Figure 5.8 shows how the input impedance for the 270nH 0603 coil inductor bonded vertically and horizontally is predominantly reactive at the resonant frequencies. For instance, the inductor in a vertical configuration has an input impedance equal to  $19.11-119.93j$ , and the inductor in a horizontal configuration has an input impedance equal to  $35.105-113.5j$ . Therefore, there is more non-propagating energy stored than energy radiated.

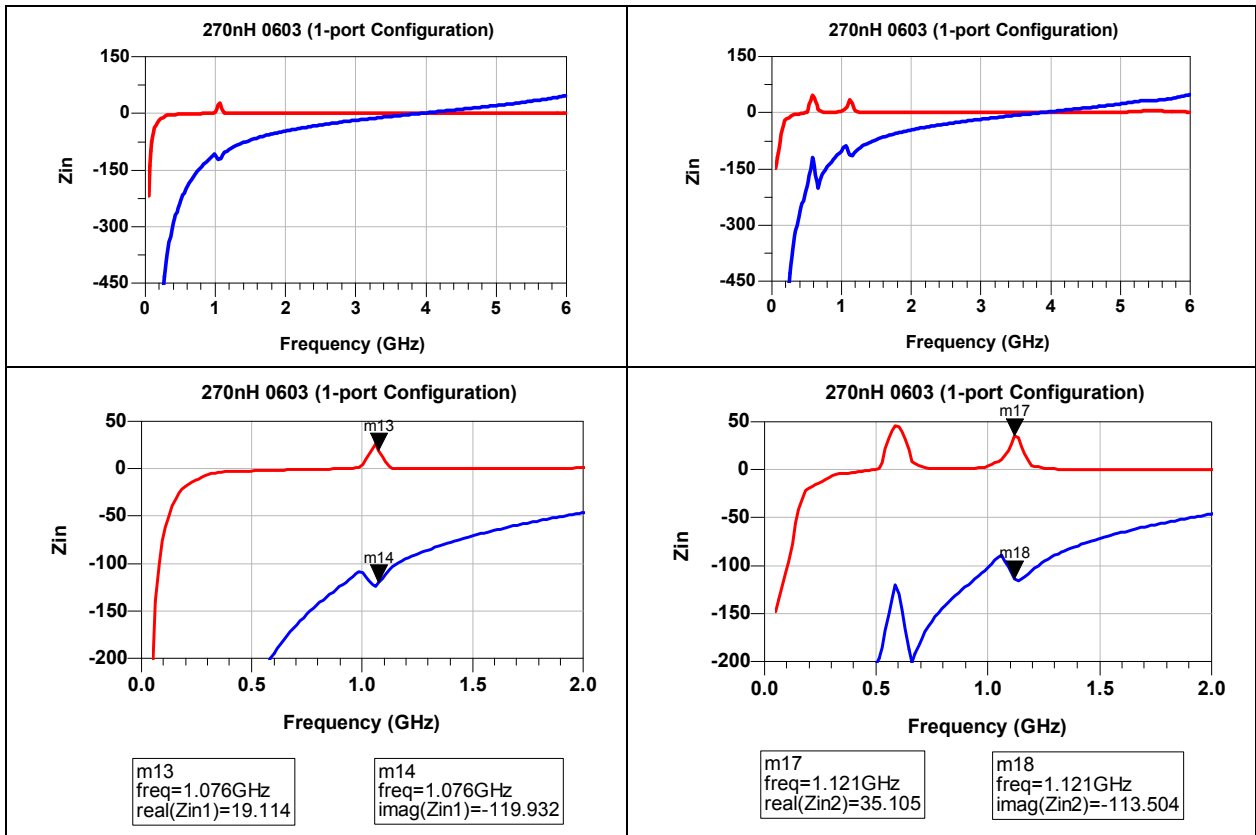


Figure 5.8 Input impedance of 270 nH 0603 Coil Inductor Bonded in a 1-Port Configuration Radiating in Free Space. Top Left- Broad-band Plot of Input Impedance for the Coil Inductor Bonded in a Vertical Configuration. Top Right- Broad-band Plot of Input Impedance for the Coil Inductor Bonded in a Horizontal Configuration. Bottom Left- Narrow-band Plot of Input Impedance for the Coil Inductor Bonded in a Vertical Configuration. Bottom Right- Narrow-band Plot of Input Impedance for the Coil Inductor Bonded in a Horizontal Configuration. Red Trace-  $Z_{in}$  (real). Blue Trace-  $Z_{in}$  (imag)

In [11], the efficiency measurement of a lossy monopole consisting of a copper strip with three 10-ohm resistors placed at interval of  $1/6$ ,  $1/2$ , and  $5/6$  along the antenna length is presented. At 950 MHz, the measured antenna efficiency is about 65%. The radiation efficiency of this monopole with different copper wire diameters ranging from 0.5 to 1.6 mm is also presented in this work. It is shown that monopoles with larger-diameter wires measured higher efficiency. For instance, a monopole with a wire diameter equal to 1.6 mm had a radiation efficiency of 98% at 950 MHz, and a monopole with wire diameter equal to 0.5 mm had a radiation efficiency of 87% at 950 MHz. All

the monopoles presented in [11] had a length of 85 mm, and were centrally mounted on a 220 mm by 220 mm ground plane. Similarly, the radiation efficiency measurement of a modified bow-tie antenna constructed as a monopole (also called a waveguide-to-coax transition) with a large surface area to minimize conductor losses is presented in [11]. The efficiency was found to be equal to 99.17%. These radiation efficiency values reported in the literature for small antennas confirm that the surface mount chip inductors used in this investigation have very low radiation efficiencies.

#### 5.4 Summary and Conclusions

The fundamental limits to how small an antenna can be at a particular wavelength and still behave as an efficient radiating device were studied. The restrictions of miniature coil antennas were examined by conducting S-parameters and efficiency measurements characterization. The measurement results show that the coil inductors have resonant frequencies with very low radiation efficiencies, which translates into the coil inductors not using effectively the available volume within the sphere of radius  $r$  enclosing them. Moreover, the coil inductors have predominantly reactive input impedances at the resonant frequencies, which indicate that there is more non-propagating energy stored than energy radiated.

Finally, even though the wheeler cap used for the efficiency measurements did not have the specified radius producing the frequency shift between shielded and unshielded measurements as well as the high loss for the shielded measurements, the coil inductors still have low efficiencies because of the predominantly reactive input impedances that make the presence of even small resistive losses decrease the efficiency.

## Chapter 6

### Conclusions and Recommendations

#### 6.1 Conclusions

In this research work, the design of frequency independent antennas, an Archimedean spiral antenna, and a narrow-band planar couple microstrip Balun were presented. Moreover, the designed Archimedean spiral antenna integrated with the narrow-band Balun was successfully fabricated and tested to validate the performance predicted by the electromagnetic simulations. An analysis of frequency selective surfaces was also conducted in order to demonstrate their capability to miniaturize an antenna overall thickness by serving as backing ground planes. Lastly, the radiation properties of surface mount chip inductors were studied to investigate the feasibility of using them as electrically small antennas.

An Equiangular and Archimedean spiral frequency independent antennas were designed and simulated as two-arm spirals for a frequency range of operation between 2 to 6 GHz. Simulations were performed with a ground plane located approximately a quarter-wavelength from the antenna, and without a ground plane, to corroborate the expected performance. It was demonstrated that the presence of a ground plane backing the antenna redirects one-half of the radiation into the opposite direction, which improves the antenna peak gain by about 3 dB. Furthermore, it was shown that when spiral antennas are backed by a quarter-wavelength substrate without a ground conducting

plane present, the radiated waves tend to get stored in the dielectric so the peak gain shifts 180 degrees in the theta direction. The simulation results showed that even though the Archimedean and the equiangular spiral antennas have different equations defining them, their performance characteristics are similar. For instance, the return loss, VSWR, total gain, and radiation characteristics follow similar and expected trends. However, the Archimedean spiral had a more flat input impedance response, as well as circular polarization over a greater bandwidth than the equiangular spiral. Despite the fact that the simulations were performed using a substrate with a fixed electrical length of  $\lambda/4$  calculated at 2.4 GHz, both spirals showed a broadband response at the designed frequency range.

With the aim of electromagnetic and circuit-level simulations, the Archimedean spiral antenna performance was successfully analyzed to the point where it was connected to the balanced feed network. It was shown that the twin-strip line feeding configuration does not affect the radiation characteristics of the antenna. It was also demonstrated that there is a trade-off in the antenna performance when the substrate backing up the antenna is reduced in thickness from an ideal  $\lambda/4$  thickness.

A narrow-band feed network that consists of a planar Balun was designed and simulated using the Agilent Advanced Design System (ADS) software in order to connect the antenna balanced input to an unbalanced line for fabrication and measurement purposes. Furthermore, the Balun was measured with the antenna as well as separate from the antenna in a back-to-back configuration. Both the Archimedean spiral antenna and Balun measurements agreed with the simulations.

A two-layer Frequency selective surface structure operating at 2.4 GHz was presented that could serve as the substrate for the Archimedean spiral antenna design to miniaturize its overall thickness. The FSS layer is static (not tuned) and thus the overall bandwidth reduces relative to the non-ground plane approach presented in Chapter 2. This type of high impedance structure not only makes it possible to reduce the antenna height by at least 69%, but also provides the opportunity of maintaining broad-band antenna responses by means of including tunable varactor diodes to the structure that adjusts the resonance frequency of the FSS.

Lastly, the fundamental limits to how small an antenna can be at a particular wavelength and still behave as an efficient radiating device were studied. The restrictions of surface mount chip inductors operating as miniature coil antennas were examined by conducting S-parameters and efficiency measurements characterization. The measurement results showed that the coil inductors have resonant frequencies with very low radiation efficiencies, which translates into the coil inductors not using effectively the available volume within the sphere of radius  $r$  enclosing them. Moreover, the measurement results also indicated that the coil inductors have predominantly reactive input impedances at the resonant frequencies due to the fact that there is more non-propagating energy stored than energy radiated.

## 6.2 Recommendations for Future Work

The simulations, analysis, and experimental data presented on the previous designs have provided interesting conclusions and ideas for future research work.

Even though it was proved that the coil inductors have low efficiencies because of the predominantly reactive input impedances that make the presence of even small

resistive losses decrease the efficiency, there is an important recommendation to validate expected results. It is advised to modify the Wheeler cap used for the efficiency measurements to have the required quarter wavelength radius so that the frequency shift between shielded and unshielded measurements as well as the high loss for the shielded measurements can be resolved.

Finally, a significant recommendation for future work regarding the frequency selective surfaces emphasizes the electromagnetic simulation of the low-frequency design operating at 2.4 GHz to validate the background theory and analysis presented in this research work. Integrating the 2.4 GHz frequency selective surface design with tunable varactor diodes is another important recommendation in order to exploit the inherently broad-band characteristics of the Archimedean spiral antenna.

## References

- [1] John D. Kraus, "Antennas for All Applications," Mc Graw Hill, 3<sup>rd</sup> Edition, New York, 2003.
- [2] Robert E. Collin, "Antenna Theory," Mc. Graw Hill, 2<sup>nd</sup> Edition, New York, 1969.
- [3] Thomas A. Milligan, "Modern Antenna Design," John Wiley & Sons, 2<sup>nd</sup> Edition, New Jersey, 2005.
- [4] Warren L. Stutzman and G. A. Thiele, "Antenna Theory and Design," John Wiley & Sons, 1<sup>st</sup> Edition, New York, 1981.
- [5] C.A Balanis, "Antenna Theory Analysis and Design," John Wiley & Sons, 2<sup>nd</sup> Edition, New York, 1982.
- [6] "Chapter 2: Analysis of Archimedean Spiral Antenna.", M.S.E.E. thesis, [scholar.lib.vt.edu/theses/available/unrestricted/Caswell\\_etd\\_Ch2.pdf](http://scholar.lib.vt.edu/theses/available/unrestricted/Caswell_etd_Ch2.pdf).
- [7] Ansoft Electronic Design Automation Software, "High Frequency Structure Simulator v9 User's Guide."
- [8] Jodie M. Bell and Magdy F. Iskander, "A Low-Profile Archimedean Spiral Antenna Using an EBG Ground Plane," IEEE Antennas and Wireless Propagation Letters, vol. 3, pp. 223-226, 2004.
- [9] David M. Pozar, "Microwave Engineering," John Wiley & Sons, 2<sup>nd</sup> Edition, New York, 1998.
- [10] E. Benabe, "Microwave Characterization and Modeling of Air Coil Inductors and Ceramic Multilayer Capacitors," M.S.E.E. thesis, University of South Florida, Tampa, Florida, 2000.
- [11] R. H. Johnston, J. G. McRory, "An improved Small Antenna Radiation-Efficiency Measurement Method," IEEE Antennas and Propagation Magazine, vol. 40, No. 5, October 1998.
- [12] J. S. McLean, "The Radiative Properties of Electrically-Small Antennas." IEEE Trans. Ant. Prop., University of Wisconsin-Madison, Madison, Wisconsin, 1994.

- [13] “Cellular Handset Antenna Efficiency Measurement Using the Wheeler Cap,” Skyworks Solutions, January 2005.
- [14] S. R. Best, “A Discussion on the Properties of Electrically Small Self-Resonant Wire Antennas,” *IEEE Antennas and Propagation Magazine*, vol. 46, No. 6, December 2004.
- [15] Rajeswari Chatterjee, “Antenna Theory and Practice,” John Wiley & Sons, 1<sup>st</sup> Edition, New York, 1988.
- [16] A. K. Skrivervik, J. F. Zurcher, O. Staub, and J. R. Mosig, “PCS Antenna Design; The Challenge of Miniaturization,” *IEEE Antennas and Propagation magazine*, vol. 43, No. 4, pp12-27, August 2001.
- [17] D. Sievenpiper, L. Zhang, R. Broas, N. Alexopolous, and E. Yablonovitch, “High-Impedance Electromagnetic Surfaces with a Forbidden Frequency Band,” *IEEE Transactions Microw. Theory Tech.*, vol. 47, no. 11, pp. 2059–2074, Nov. 1999.
- [18] D. Sievenpiper, “Forward and Backward Leaky Wave Radiation with Large Effective Aperture from a Electronically Tunable Textured Surface,” *IEEE Trans. Antennas Propag.*, vol. 53, no. 1, pp. 236–247, Jan. 2005.
- [19] D. Sievenpiper, J. Schaffner, H. J. Song, R. Loo, and G. Tansonan, “Two Dimensional Beam Steering Reflector Using an Electrically Tunable Impedance Surface,” *IEEE Trans. Antennas Propag.*, vol. 51, no. 10, pp. 2713–2722, Oct. 2003.